First Step of the Oxygen Reduction Reaction: A Computational Study of O_2 Adsorption at Electrified Metal/Water Interfaces

Dissertation

zur Erlangung des akademischen Grades
einer Doktorin der Naturwissenschaften (Dr. rer. nat.)
am Fachbereich Physik der Freien Universität Berlin

vorgelegt von
M. Sc. Alexandra M. Dudzinski
Berlin 2024

Fritz-Haber Institut der Max-Planck Gesellschaft

Erstgutachter: Prof. Dr. Karsten Reuter

Zweitgutachter: Prof Dr. Martin Weinelt

Tag der Disputation: 24.01.2025

Dla mojego brata, Fryderyk R. Dudzinski.

Acknowledgment

First and foremost, I extend my heartfelt thanks to Prof. Karsten Reuter for allowing me to pursue my PhD at the Fritz Haber Institute of the Max Planck Society. His belief in my abilities and his support gave me an invaluable opportunity to grow academically and professionally, his approach to science has been a major inspiration to me. I would like to express my gratitude to my supervisor, Dr. Vanessa J. Bukas, and my co-worker, Dr. Elias Diesen. Their support, guidance, and collaboration were invaluable throughout my PhD research. I want to thank Prof. A. C. Luntz and Dr. Frank Abild-Pedersen for enabling my research stay at the SLAC National Accelerator Laboratory by Stanford University. I am also grateful to Dr. Hendrik H. Heenen for sharing many insights and existing AIMD data.

To my dear family - my mother Joanna Dudzinski, brother Fryderyk Dudzinski, father Robert Dudzinski, and my cat Puma - your unconditional love and unwavering support have been my cornerstone. Your encouragement and belief in me have been a source of love, strength, stability, and joy throughout this challenging journey.

I am deeply thankful to my dear colleagues Sina Ziegler, Patricia König, Tabea Huss, Olga Vinogradova, Maryke Kouyate, Robert Strothmann, Simeon Beinlich, and Jakob Timmermann. Your companionship and support during both the dark and joyous times have made this journey memorable. Thanks to Thorben Eggert and again to Patricia for organizing the annual workshop with me; tackling it was very rewarding. To Katinka Freis, Anna Schröder, Deniz Meyer, Jaline Richter, my climbing partners, my friends from dancing, and all other amazing friends, thank you for always being there for me, for your constant support, and for listening to me. Your friendships have been a beacon of light during my PhD journey. I extend my heartfelt thanks to everyone I met along this journey, all co-workers at the Fritz-Haber Institute and Stanford University, and all other inspiring people I have met. Each one of you has contributed in your unique way to making my PhD experience special and unforgettable. I am beyond joyous and proud to have you all in my life.

Lastly, I want to express my gratitude toward this world, life, and myself. I am grateful for every wall to climb, all the music to dance to, and all the living beings to connect with. I am beyond thankful for the privilege of contributing to the fundamental understanding of nature, our beautiful, God-given source of all.

Declaration of Authorship

Name: Dudzinski

First name: Alexandra Maxi

I declare to the Freie Universität Berlin that I have completed the submitted dissertation independently and without the use of sources and aids other than those indicated. The present thesis is free of plagiarism. I have marked as such all statements that are taken literally or in content from other writings. This dissertation has not been submitted in the same or similar form in any previous doctoral procedure.

I agree to have my thesis examined by a plagiarism examination software.

Date: _____ Signature: _____

Contents

Abstract

The oxygen reduction reaction (ORR) is a key limiting factor in fuel cell technology, driving extensive research efforts over the past few decades. Studies based on experiments and theoretical calculations on model single-crystal electrodes have helped establish fundamental trends across transition metal catalysts. In heterogeneous electrocatalysis, local electric field effects at the electrical double layer significantly influence the energies of reaction intermediates and impact catalyst performance in acidic or alkaline environments. However, these local field effects are challenging to model computationally and are frequently omitted. First, this work focuses on O_2 adsorption as the initial step of the ORR to understand the role of the electric field. The first part of the study focuses on the weak binding Au(111) metal catalyst surface, which favors the formation of hydrogen peroxide over water, with its activity strongly dependent on the (absolute) electrode potential. The underlying microscopic mechanisms remain unclear, likely involving key elementary reaction steps. We systematically enhance the double-layer model to clarify and compare the physical effects of the local field on O_2 adsorption. This progression includes an applied saw-tooth potential in vacuum, an implicit solvent model, and explicit water modeling via *ab initio* molecular dynamics (AIMD). Two main contributions are identified to the potential dependence of O_2 adsorption. Firstly, a dominant dipole-field interaction favors O_2 binding going to reducing conditions across all models. Additionally, we observe stabilization from explicit H-bonding that can only be observed in AIMD, leading to a peroxo-O_2* and a significant field response near the ORR onset. Since the O_2* adsorption becomes favorable close to experimental ORR onsets and can explain experimental SHE-driven ORR activity, we predict that O_2 adsorption is a potential-dependent, potentially rate-determining step of the ORR on the weak binding Au(111). These findings highlight the necessity of incorporating local electric field effects and explicit water in electrochemical interface models. Secondly, we draw a comparison to the more reactive Pt(111) surface. We conduct AIMD simulations to analyze and compare the properties of the metal/water interface Au(111) vs. Pt(111). Unlike Au(111), Pt(111) exhibits negligible potential dependence under realistic ORR conditions due to the inherently different reactivity of the two metals. We find a closely adsorbed peroxo O_2* state with a relatively constant number of H-bonds, irrespective of the potential or surface coverage on the Pt(111). In contrast, the interfacial water structure on Pt(111) undergoes significant changes due to the inclusion of more realistic surface coverages and potential variations. In our set-up, we observe O_2* dissociation determining the ORR selectivity towards H_2O. We find an indirect effect of the potential through surface coverage: The O_2* dissociation is promoted by desorption of H_2O* at reducing conditions. Our overall results emphasize the importance of accounting for local field effects, which i) can directly impact reaction steps but ii) can also indirectly impact the reaction mechanism through a more complex interplay between potential, surface coverage, and water structure.

Zusammenfassung

Die Sauerstoffreduktionsreaktion (ORR) ist ein entscheidender limitierender Faktor in der Brennstoffzellentechnologie, der in den letzten Jahrzehnten zu umfangreichen Forschungsbemühungen geführt hat. Bei der heterogenen Elektrokatalyse beeinflussen lokale Feldeffekte an der elektrischen Doppelschicht den Reaktionsmechanismus erheblich und wirken sich auf die Leistung des Katalysators aus. Diese lokalen Feldeffekte sind jedoch theoretisch schwer zu modellieren und werden oft vernachlässigt. Diese Arbeit konzentriert sich auf die O_2-Adsorption als ersten Schritt der ORR, um die Rolle des elektrischen Feldes zu verstehen. Zunächst wird die schwach bindende Au(111)-Katalysatoroberfläche untersucht, die die Bildung von H_2O_2 gegenüber H_2O bevorzugt, wobei ihre Aktivität stark vom (absoluten) Elektrodenpotential abhängt. Die zugrundeliegenden mikroskopischen Mechanismen sind noch unklar. Wir verbessern systematisch das Modell der elektrifizierten Metall/Wasser-Grenzfläche, um die physikalischen Effekte des lokalen Feldes auf die O_2-Adsorption zu verstehen und zu vergleichen. Die erste Approximation ist ein Sägezahnpotential im Vakuum, die Zweite ist ein implizites Lösungsmittelmodell und die Letzte ist die explizite Wassermodellierung mittels *ab initio* Molekulardynamik (AIMD). Zwei Hauptbeiträge zur Potentialabhängigkeit der O_2-Adsorption an Au(111) werden identifiziert. Erstens begünstigt eine starke Dipol-Feld Wechselwirkung die Bindung von O_2 unter reduzierenden Bedingungen in allen Modellen. Darüber hinaus beobachten wir eine zusätzliche Stabilisierung durch explizite Wasserstoffbrückenbindungen, die nur in AIMD Simulationen beobachtet werden kann, was zu einem peroxoartigen Sauerstoff an der Oberfläche und einer signifikant günstigeren O_2-Adsorption nahe realistischen ORR-Potentialen führt. Wir sagen vorraus dass die O_2-Adsorption ein kritischer, potentialabhängiger Schritt der ORR auf der schwach bindenden Au(111)-Oberfläche ist. Zweitens ziehen wir einen Vergleich zur reaktiveren Pt(111)-Oberfläche mit Hilfe von AIMD Simulationen. Im Gegensatz zu Au(111) zeigt Pt(111) unter realistischen ORR-Bedingungen aufgrund der inhärent unterschiedlichen Reaktivität der beiden Metalle eine vernachlässigbare Potentialabhängigkeit. Wir finden einen Peroxo-O_2* mit einer konstanten Anzahl von H-Bindungen, unabhängig vom Potential oder der Oberflächenbedeckung. Im Gegensatz dazu erfährt die Grenzflächenwasserstruktur auf Pt(111) signifikante Veränderungen, wenn realistische Oberflächenbedeckungen und Potenzialschwankungen berücksichtigt werden. In unserem Versuchsaufbau beobachten wir O_2* Dissoziation, was die ORR-Selektivität gegenüber H_2O bestimmt. Wir stellen einen indirekten Effekt des Potentials durch die Oberflächenbedeckung fest: Die O_2*-Dissoziation wird durch die Desorption von H_2O* unter reduzierenden Bedingungen gefördert. Unsere Gesamtergebnisse betonen die Bedeutung der Berücksichtigung von lokalen Feldeffekten, die i) direkt auf Reaktionsschritte einwirken können, aber ii) auch indirekt den Reaktionsmechanismus durch ein komplexes Zusammenspiel zwischen Potential, Oberflächenbedeckung und Wasserstruktur beeinflussen können.

Streszczenie

Reakcja redukcji tlenu (oxygen reduction reaction - ORR) jest kluczowym czynnikiem ograniczającym w technologii ogniw paliwowych, co doprowadziło do szeroko zakrojonych wysiłków badawczych w ostatnich dziesięcioleciach. W elektrokatalizie heterogenicznej efekty pola lokalnego w podwójnej warstwie elektrycznej znacząco wpływają na mechanizm reakcji i wydajność katalizatora. Jednak te efekty pola lokalnego są trudne do modelowania teoretycznego i często są zaniedbywane. Niniejsza praca koncentruje się na adsorpcji O_2 jako pierwszym etapie ORR, aby zrozumieć rolę pola elektrycznego. Po pierwsze, badana jest słabo wiążąca powierzchnia katalizatora Au(111), która sprzyja tworzeniu H_2O_2 zamiast H_2O, a jej aktywność silnie zależy od (bezwzględnego) potencjału elektrody. Podstawowe mechanizmy mikroskopowe są nadal niejasne. Systematycznie ulepszamy model naelektryzowanego interfejsu metal/woda, aby zrozumieć i porównać fizyczny wpływ lokalnego pola na adsorpcję O_2. Pierwsze przybliżenie to potencjał piłokształtny w próżni, drugie to niejawny model rozpuszczalnika, a ostatnie to jawne modelowanie wody przy użyciu *ab initio* dynamiki molekularnej (AIMD). Zidentyfikowano dwa główne czynniki wpływające na potencjalną zależność adsorpcji O_2 na Au(111). Po pierwsze, silne oddziaływanie dipol-pol sprzyja wiązaniu O_2 w warunkach redukcji we wszystkich modelach. Ponadto obserwujemy dodatkową stabilizację poprzez wyraźne wiązanie wodorowe, które można zaobserwować tylko w symulacjach AIMD, co prowadzi do nadtlenopodobnego tlenu na powierzchni i znacznie korzystniejszej adsorpcji O_2 w pobliżu realistycznych potencjałów ORR. Przewidujemy, że adsorpcja O_2 jest krytycznym, zależnym od potencjału etapem ORR na słabo wiążącej powierzchni Au(111). Po drugie, dokonujemy porównania z bardziej reaktywną powierzchnią Pt(111) przy użyciu symulacji AIMD. W przeciwieństwie do Au(111), Pt(111) wykazuje znikomą zależność od potencjału w realistycznych warunkach ORR ze względu na z natury różną reaktywność obu metali. Znajdujemy peroxo-O_2* ze stałą liczbą wiązań H, niezależną od potencjału lub pokrycia powierzchni. W przeciwieństwie do tego, międzyfazowa struktura wody na Pt(111) ulega znaczącym zmianom po uwzględnieniu realistycznego pokrycia powierzchni i fluktuacji potencjału. W naszym układzie eksperymentalnym obserwujemy dysocjację O_2*, która determinuje selektywność ORR w stosunku do H_2O. Stwierdziliśmy pośredni wpływ potencjału poprzez pokrycie powierzchni: dysocjacja O_2* jest promowana przez desorpcję H_2O* w warunkach redukujących. Nasze ogólne wyniki podkreślają znaczenie uwzględnienia lokalnych efektów pola, które mogą (i) bezpośrednio wpływać na etapy reakcji, ale (ii) również pośrednio wpływać na mechanizm reakcji poprzez złożoną interakcję między potencjałem, pokryciem powierzchni i strukturą wody.

List of Publications

This thesis is based on work from two publications:

[1] Dudzinski, A. M.; Diesen, E.; Heenen, H. H.; Bukas, V. J.; Reuter, K. First Step of the Oxygen Reduction Reaction on Au(111): A Computational Study of O_2 Adsorption at the Electrified Metal/Water Interface. *ACS Catalysis* **2023**, *13*, 12074–12081, DOI: 10.1021/acscatal.3c02129, this publication is licensed under CC-BY 4.0.

[2] Dudzinski, A. M.; Diesen, E.; Reuter, K.; Bukas, V. J. Oxygen Adsorption at the Electrochemical Metal/Water Interface: Au(111) vs. Pt(111). *Journal of Physical Chemistry C* **2024**, *128*, 49, 20886–20894, DOI: 10.1021/acs.jpcc.4c06384, this publication is licensed under CC-BY 4.0.

Furthermore, during the doctoral research, contributions were provided to the following work:

[3] Diesen, E.; Dudzinski, A. M.; Reuter, K.; Bukas, V. J. On the Origin of Electrocatalytic Selectivity during the Oxygen Reduction Reaction on Au(111). *ChemRxiv* **2024**, Working Paper, Version 1. Submitted for publication, DOI: 10.26434/chemrxiv-2024-7jj5n.

Li, Z.; Öztuna, E.; Skorupska, K.; Vinogradova, O.; Jamshaid, A.; Steigert, A.; Rohner, C.; Dimitrakopoulou, M.; Prieto, M.; Kunkel, C.; Stredansky, M.; Kube, P.; Götte, M.; Dudzinski, A. M.; Girgsdies, F.; Wrabetz, S.; Frandsen, W.; Blume, R.; Zeller, P.; Muske, M.; Delgado, D.; Köchler, T.; Arztmann, M.; Efimenko, A.; Frisch, J.; Kokumai, T.; Garcia-Diez, R.; Bär, M.; Hammud, A.; Kröhnert, J.; Trunschke, A.; Scheurer, C.; Schmidt, T.; Lunkenbein, T.; Amkreutz, D.; Kuhlenbeck, H.; Bukas, V.; Knop-Gericke, A.; Schlatmann, R.; Reuter, K.; Roldan Cuenya, B.; Schloegl, R. Rationally designed laterally-condensed-catalysts deliver robust activity and selectivity for ethylene production in acetylene hydrogenation. *Nature Communications* **2024**, *15*, 10660, DOI: 10.1038/s41467-024-54784-z.

List of Acronyms

- **PEMFC:** Proton exchange membrane fuel cells.
- **ORR:** Oxygen reduction reaction.
- **PCET:** Proton coupled electron transfer.
- **DFT:** Density functional theory.
- **PZC:** Point of zero charge.
- **CHE:** Computational hydrogen electrode.
- **RHE:** Reversible hydrogen electrode.
- **SHE:** Standard hydrogen electrode.
- **AIMD:** *Ab initio* molecular dynamics.
- **BOA:** Born-Oppenheimer approximation.
- **KS:** Kohn-Sham.
- **PAW:** Projector augmented waves.
- **VASP:** Vienna ab initio simulation package [4–6].
- **SCF:** Self-consistent field.
- **LDA:** Local density approximation.
- **GGA:** Generalized gradient approximation.
- **PW91:** Perdew-Wang 1991.
- **PBE:** Perdew-Burke-Ernzerhof.
- **RPBE:** Revised Perdew-Burke-Ernzerhof.
- **BEEF-vdW:** Bayesian error estimation functional with van der Waals correlation.
- **TPSS:** Tao-Perdew-Staroverov-Scuseria.
- **BOMD:** Born-Oppenheimer approximation.
- **ZPE:** Zero point energy.
- **AO:** Atomic orbital.
- **MO:** Molecular orbital.
- **$\mathbf{COM}_z$:** Center-of-mass height above metal surface .
- **ML:** Mono layer.
- **RDS:** Rate determining step.
- **RDE:** Rotating disk electrode.

Chapter 1

Introduction

1.1 Fuel Cells for Green Energy

One of the most pressing challenges facing modern society today is how to mitigate climate change. We can already observe and feel the changes in the environment, such as rising temperatures, changes in flora and fauna, melting glaciers, rising sea levels, and unpredictable weather changes in most regions of our planet. This is mainly due to the anthropogenic increase of carbon dioxide in the atmosphere, mostly as a result of the conversion of fossil resources into fuels and chemicals that are essential for modern life [7]. Therefore, the search for alternative carbon-neutral technologies is an ongoing quest to ensure the decrease of anthropogenic impact on nature.

At the heart of realizing a secure and sustainable future lies the exploitation of renewable energy sources such as solar, wind, and hydroelectric power. One of the pillars of a future sustainable energy landscape lies in the development of efficient electrocatalytic technologies that enable chemical-to-electrical conversion and *vice versa* [8, 9] and circumvent the burning/exhaustion energy into the atmosphere. Green hydrogen, among other liquid fuels, is one of the most promising and environmentally friendly energy carriers today. In the so-called Proton Exchange Membrane Fuel Cell (PEMFC), chemical energy carriers such as hydrogen are oxidized to produce electricity. Figure 1.1 shows a simplified scheme of a fuel cell, where hydrogen is oxidized at the anode and oxygen is reduced at the cathode to produce electricity. Another advantage is that there are no toxic byproducts of this reaction since the byproduct is mostly just water.

This technology is interesting for several domains, i. e. several automobile manufacturers have started to commercialize fuel cell electric vehicles [10]. Other domains where fuel cell application can potentially play a role include stationary and portable power generation, industrial application, aerospace, defense application, and grid support. This technology can also be used for decentralized, small-scale chemical synthesis, e.g. H_2O_2 synthesis. PEMFCs are mostly interesting candidates for small to medium scale operations. [8]

However, further technological breakthroughs are necessary to enable a sustainable

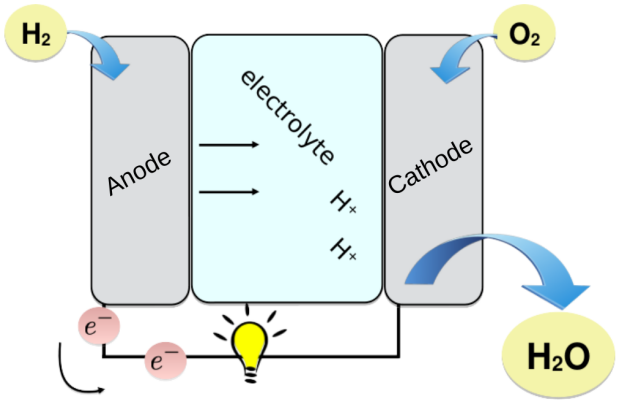

Figure 1.1: Schematic description of the fuel cell. Hydrogen molecules undergo oxidation at the anode, releasing electrons and protons, while at the cathode, oxygen molecules are reduced by electrons and combine with protons to form water. This process generates electricity, heat, and water as by-products.

and efficient hydrogen-based economy. Hydrogen fuel cells have several fundamental problems that limit the overall performance and application of PEMFCs: First, the high cost of the platinum-based catalysts that are commonly used. Although platinum is known to be the best elemental catalyst (see Section 1.2.2), it is estimated that about 40 % of the cost of the fuel cell comes from the Pt-based catalyst [11]. Furthermore, platinum production is limited to less than 200 tons per year [12], and even if all of it is dedicated to, e.g., PEMFC-powered automobiles, it will not be sufficient to cover today's needs by orders of magnitude [13]. However, the choice of catalyst material is severely limited by realistic ORR conditions: The catalyst must withstand highly acidic or alkaline and oxidizing environments. Besides platinum, the other elemental metals that can remain thermodynamically stable without corroding and have sufficient stability are gold and iridium. Therefore, research is still often focused on Pt-based alloys for fuel cell applications [13].

Another limitation of PEMFC is the low rate of the oxygen reduction reaction (ORR) at the cathode on a conventional Pt-based catalyst [13]. This can be explained by the overpotential, which is defined as the extra voltage required above the equilibrium potential to drive an electrochemical reaction. It usually results from sluggish kinetics, leading to energy losses and reduced efficiency in electrochemical systems. Nearly two-thirds of the overpotential required in fuel cells stem from the ORR [8, 11, 14–16]. Thus, the overall performance of fuel cell applications is directly affected by the efficiency of the ORR [17]. The reaction takes place at the cathode where molecular oxygen is reduced by four protons and electrons to water while generating electrical potential (as shown in Figure 1.1). Consequently, it is of great importance

to understand the mechanism of this reaction in great detail. Yet, experimentally it is very difficult to draw conclusions for the reaction mechanism since the intermediates are difficult to detect *in situ* [13, 18, 19].

Several theoretical frameworks have been used to understand the reaction mechanism in depth, but difficulties arise in modeling the electrified metal/water interface, including all possible effects of solvents, coverage effects, and the charged electric double layer. Nevertheless, computational simulations have proven to be an essential tool to unravel the atomistic structure and dynamics that play a key role in various applications in the chemistry and physics of condensed matter [20–22]. This work is dedicated to unveiling some of the intricacies of the ORR from a computational perspective.

1.2 Theory of the Oxygen Reduction Reaction

1.2.1 Reaction Mechanism

The ORR has frequently been described using a charge-neutral framework, wherein a proton-coupled electron transfer (PCET) occurs at each step. The most common pathways are either a two-electron partial reduction, which results in the formation of hydrogen peroxide H_2O_2 (Equation (1.1)) or a four-electron reduction leading to H_2O (Equation (1.3)). In the two-electron pathway, O_2 is adsorbed, and sequentially reduced to OOH* and finally H_2O_2 (Equation (1.2)). This reaction is associated with a standard equilibrium potential $E^\circ = 0.70$ V [8]:

$$\mathrm{O_2} + 2\,(\mathrm{H^+} + \mathrm{e^-}) \longrightarrow \mathrm{H_2O_2} \qquad E^\circ = 0.70\ \mathrm{V} \tag{1.1}$$

$$\begin{aligned} \mathrm{O_2} &\longrightarrow \mathrm{O_2^*} \\ \mathrm{O_2^*} + (\mathrm{H^+} + \mathrm{e^-}) &\longrightarrow \mathrm{OOH^*} \\ \mathrm{OOH^*} + (\mathrm{H^+} + \mathrm{e^-}) &\longrightarrow \mathrm{H_2O_2} \end{aligned} \tag{1.2}$$

On the contrary, for the four-electron pathway (Equation (1.3)), there are two widely accepted mechanisms: The associative mechanism (Equation (1.4)), where adsorbed O_2* firstly forms OOH*, then dissociates to form OH*+H_2O and lastly gives $2H_2O$ by adding $(H^+ + e^-)$ at each step. The second mechanism is the dissociative mechanism (Equation (1.5)) where the dissociation of O_2* precedes the protonation and reduction of the newly formed O* species. The standard equilibrium potential is known to be $E^\circ = 1.23$ V [8].

$$\mathrm{O_2} + 4\,(\mathrm{H^+} + \mathrm{e^-}) \longrightarrow 2\,\mathrm{H_2O} \qquad E^\circ = 1.23\ \mathrm{V} \tag{1.3}$$

$$\begin{aligned} \mathrm{O_2} &\longrightarrow \mathrm{O_2}^* \\ \mathrm{O_2}^* + (\mathrm{H^+} + \mathrm{e^-}) &\longrightarrow \mathrm{OOH}^* \\ \mathrm{OOH}^* + (\mathrm{H^+} + \mathrm{e^-}) &\longrightarrow \mathrm{OH}^* + \mathrm{H_2O} \\ \mathrm{OH}^* + (\mathrm{H^+} + \mathrm{e^-}) &\longrightarrow \mathrm{H_2O} \end{aligned} \tag{1.4}$$

$$\begin{aligned} \mathrm{O_2} &\longrightarrow \mathrm{O_2}^* \\ \mathrm{O_2}^* &\longrightarrow \mathrm{O}^* + \mathrm{O}^* \\ \mathrm{O}^* + \mathrm{O}^* + 2\,(\mathrm{H^+} + \mathrm{e^-}) &\longrightarrow \mathrm{OH}^* + \mathrm{OH}^* \\ 2\,\mathrm{OH}^* + 2\,(\mathrm{H^+} + \mathrm{e^-}) &\longrightarrow 2\,\mathrm{H_2O} \end{aligned} \tag{1.5}$$

The interplay between these pathways is governed by surface structure, catalyst composition, and operating conditions. In prior literature, the adsorption of the O_2 has frequently been dismissed as a chemical step that does not contribute to the potential dependence [8]. However, open questions still remain regarding the role of O_2 adsorption. The O_2 adsorption could become limiting due to either a weak binding metal catalyst surface like, e.g., on Au(111) [1] or due to competing adsorption with other possible surface coverage species (like e.g., OH*, H_2O* and O*) for strong binding metal catalyst like e.g. Pt(111) [11]. We will, therefore, focus on gaining more insight into the role of the O_2* adsorption at the interface and its effects on the reaction mechanism of the ORR.

1.2.2 Sabatier Principle and Volcano Plots

A fundamental concept that helps rationalize multiple catalyst materials is the Sabatier principle [23]. This principle states that the effectiveness of a catalyst in promoting a reaction depends critically on the strength of the reactant's adsorption onto the catalyst surface. According to Sabatier, optimal catalytic activity is achieved when the adsorption strength is neither too weak nor too strong. If the adsorption is too weak, the reactants will not bind sufficiently to the catalyst to react; conversely, if the adsorption is too strong, reactants remain bound to the catalyst, preventing the products from desorbing.

Following Norskov *et al.* [24], one can plot the theoretical activity vs. the formation energy of OH* to get a so-called volcano plot. The name volcano plot derives from the characteristic shape of the curve: it rises from low activity at both extremes of

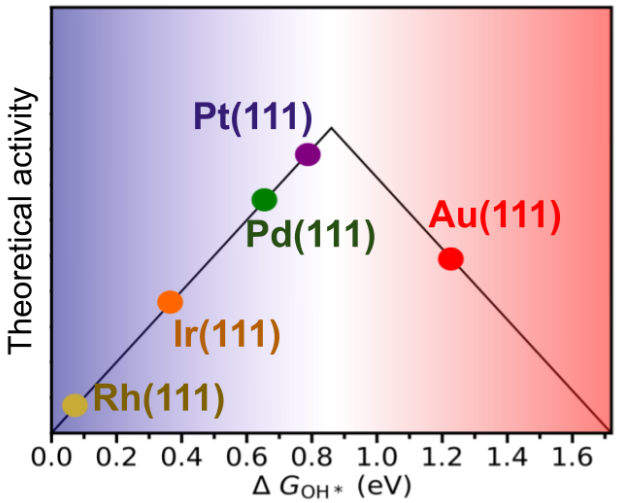

Figure 1.2: Schematic Figure to show the volcano plot for the ORR. The theoretical activity is plotted vs. the formation free energy of OH*. The values are adapted from Norskov *et al.* [24]. The strong-binding metal catalyst regime is marked in blue, while the weak-binding metal catalyst regime is denoted in red.

weak and strong adsorption to reach a peak at intermediate adsorption energy, which represents the optimal condition as predicted by the Sabatier principle. The formation energy of OH* can be chosen as an example to show the volcano relationship, but any other intermediate of the ORR would also do due to scaling relationships between the intermediates [24].

The volcano plot illustrates the connection between adsorption energies and catalytic activity [25]. In Figure 1.2 one can see the so-called volcano plot for the ORR. On the right-hand side are the weak binding metal surface catalysts like, e.g., Au(111). In this regime, the rate-limiting step is the adsorption of the reactant. However, on the strong binding side of the volcano plot, one can observe strong binding metal catalysts, such as Pt(111), where the product desorption is rate-limiting. The objective is to achieve an optimal trade-off between strong and weak binding. A catalyst that is closer to the top of the volcano will exhibit enhanced performance due to the maximized activity. To elucidate the O_2 adsorption under the influence of potential at the interface on both sides of the volcano, we will concentrate on the weak binding Au(111) and the strong binding Pt(111).

1.2.3 Modelling Electrochemical Systems

In recent years, the atomic-level understanding of heterogeneous electrocatalysis has significantly advanced. This progress is largely due to both numerous experimen-

tal innovations and simultaneous breakthroughs in first-principles simulations of the electrified solid/liquid interface. In theoretical electrocatalysis, density functional theory (DFT) calculations are often used to calculate charge-neutral reaction intermediates under conditions matching the potential at the point of zero charge (PZC). The computational hydrogen electrode (CHE) enables the inclusion of the potential *a posteriori* [24]. This referencing technique enables alignment of the chemical potential of a proton-electron pair to that of H_2 in the gas phase.

$$H^+ + e^- \rightleftharpoons \frac{1}{2}H_2(g) \qquad @U_{SHE} = 0 \tag{1.6}$$

$$\mu(H^+ + e^-) = \frac{1}{2}G(H_2(g)) - eU_{SHE} \tag{1.7}$$

It enables the construction of an energy reaction mechanism only using computationally efficient calculations of charge-neutral intermediates without explicitly treating electrons or ions in the solution. Potential effects for each reaction intermediate can now be included with the condition, that each step is composed of a so-called proton-coupled electron transfer (PCET). The intermediates can then be aligned to the potential vs. the reversible hydrogen electrode (RHE) or U_{RHE}. It consists of two terms: The first one describes electron activity in form of the absolute potential or potential vs. the standard hydrogen electrode (SHE) or U_{SHE}. The second term describes the proton activity:

$$U_{RHE} = U_{SHE} + k_B T ln(10) \times (pH) \times (N_e)^{-1} \tag{1.8}$$

where k_B is the Boltzmann constant, T the temperature and N_e the number of electrons. This elegant approximation often leads to the major simplification that each step of the ORR is a step-wise reduction by a PCET as seen in the mechanisms commonly used (Equation (1.1)-(1.5)).

While using first-principle calculations with charge-neutral intermediates offers substantial advantages, it also leads to limitations: Calculations at PZC inherently neglect the potential-dependent capacitive charging that is found at the electrified metal/water interfaces at realistic electrochemical conditions. Constructing a reaction mechanism only by using PCET can only explain mechanistic responses to the potential vs. RHE (U_{RHE}). The dependence of pH on the potential vs. RHE scale cannot be explained since U_{RHE} already includes the effects of protons and electrons simultaneously. Conversely, "chemical" steps of the reaction network are assumed to be independent of the electrochemical potential. Such steps refer to elementary reac-

tions that do not involve an explicit PCET, for instance, O_2 adsorption in the ORR [1, 2], CO_2 adsorption [26, 27], or CO dimerization [28–30] in the electrochemical reduction of CO_2. In cases where these "chemical" steps become rate-determining, the model cannot explain the experimental behavior anymore since it cannot capture purely potential-dependent steps that do not include a proton transfer, i.e., steps that can also be called proton-decoupled electron transfers or non-PCET. Generally, this simplistic charge-neutral representation is sufficient in many cases [31], but it breaks down when variations in electrocatalytic activity are experimentally observed without pH-adjustments vs. the absolute potential U_{SHE} or equivalently with pH adjustments vs. U_{SHE} for specific catalysts under certain conditions [32–35]. One example we will look into is the ORR on Au(111) in Chapter 4, where we find pH-dependent activity vs. U_{RHE} scale, which could be explained through a non-PCET step being rate-determining.

1.3 Outline of Thesis

This thesis aims to explore the role of the electric field at the electrochemical interface, specifically for the ORR from a computational perspective. We will focus on investigating the first step of the ORR, the O_2* adsorption on the weak binding Au(111) and the strong binding Pt(111).

In the following chapter, "Theory and Methods", we will dive deep into the theoretical framework. Modeling the electrochemical interface requires the inclusion of quantum effects, we therefore make use of density functional theory (DFT). To get a dynamic picture, we utilize *ab initio* molecular dynamics simulations (AIMD). We explain the methods that we use to model the electrified metal/water interface: Saw-tooth potential in vacuum, implicit solvation methods, and also the addition of a re-parametrized hydrogen potentials to our AIMD simulations to add explicit charge effects.

Since we will delve into the O_2 adsorption at the interface, the third chapter is dedicated to "O_2 Adsorption". Here, we will go into detail on the calculation of the O_2 adsorption energies, error analysis, and lastly, free energy contributions, and how we define and treat O_2 adsorption in AIMD.

The fourth chapter "O_2 Adsorption on the Weak Binding Au(111)" explains the first part of our work which is based on Ref. [1]: We investigate the O_2 adsorption on the weak binding Au(111). We compare multiple methods to model the metal/water interface and draw the main conclusion that potential effects and interfacial explicit water cannot be neglected since they lead to favorable O_2 adsorption close to experimental ORR onset.

The last chapter, before the conclusion, "O_2 Adsorption on the Strong Binding Pt(111)" uses the methodological insights gained from the previous chapter and compares the results from the weak binding Au(111) with the strong binding Pt(111) surface with the help of AIMD simulations. It is based on Ref. [2]. We investigate the O_2 adsorption and find that the O_2 adsorption is almost potential independent on the Pt(111) surface. We compare the water structures at the electrified interface and look at the role of realistic OH* coverage on Pt(111). Lastly, we also discuss the observed O-O* dissociation that becomes potential dependent through coverage effects on the OH*-covered Pt(111), showing how potential indirectly impacts the ORR.

Chapter 2

Theory and Methods

The main goal of this work is to gain insights into the electrified metal/water interface from a computational perspective. This chapter will explain the theoretical and technical groundwork to understand the utilized methods. Firstly, we explain density functional theory (DFT). DFT as the base allows for the inclusion of quantum effects, which is necessary when looking at effects that take place on the electronic level. Building on top of that, we also employ *ab initio* molecular dynamics (AIMD) simulations that enable us to get a dynamic picture and include explicit water. In AIMD simulations, finite-temperature dynamical trajectories are simulated where the forces stem from DFT calculations "on the fly" at each time step. Lastly, we compare three methods that enable charging the interface: Saw-tooth potential in vacuum, implicit solvation, and inclusion of re-parametrized H potentials to charge the interface in AIMD.

2.1 Density Functional Theory

DFT is an *ab initio* method to solve for the electronic structure of atomic systems, that give a tremendous electronic wave function. To get the ground state energy of a system, one has to solve the time-independent Schrödinger equation (see Equation (2.1)) for a system with N_e electrons at positions $\mathbf{r}$ and N_N nuclei at positions $\mathbf{R}$ [36, 37]:

$$\hat{H}\Psi(\mathbf{r},\mathbf{R}) = E\Psi(\mathbf{r},\mathbf{R}) \tag{2.1}$$

$$\mathbf{r} = (\mathbf{r}_1, \mathbf{r}_2, \mathbf{r}_3, ..., \mathbf{r}_{N_e}) \tag{2.2}$$

$$\mathbf{R} = (\mathbf{R}_1, \mathbf{R}_2, \mathbf{R}_3, ..., \mathbf{R}_{N_N}) \tag{2.3}$$

where $\hat{H}$ is the Hamiltonian, $\Psi(\mathbf{r},\mathbf{R})$ is the wave function of a system and E the energy of that system. Spin variables are usually also included as degrees of freedom, next to the electronic positions $\mathbf{r}$, but for simplicity, we will neglect those in the following explanations. The Hamiltonian $\hat{H}$ can also be written in terms of operators

describing each energy contribution [37]:

$$\begin{aligned}\hat{H} &= \hat{T}_e(\mathbf{r}) + \hat{U}_{ee}(\mathbf{r}) + \hat{V}_{eN}(\mathbf{r},\mathbf{R}) \\ &\quad + \hat{T}_N(\mathbf{R}) + \hat{V}_{NN}(\mathbf{R}) \qquad (2.4)\\ \hat{H} &= -\sum_{i=1}^{N_e} \frac{\hbar^2}{2m_e}\nabla_i^2 + \sum_{i,j=1,i<j}^{N_e} \frac{e^2}{|\mathbf{r}_i - \mathbf{r}_j|} - \sum_{I=1}^{N_N}\sum_{i=1}^{N_e} \frac{Z_I e^2}{|\mathbf{R}_I - \mathbf{r}_i|} \\ &\quad - \sum_{I=1}^{N_N} \frac{\hbar^2}{2M_I}\nabla_I^2 + \sum_{I,J=1;I<J}^{N_N} \frac{Z_I Z_J e^2}{|\mathbf{R}_i - \mathbf{R}_j|}\end{aligned}$$

where $\hat{T}_e$ and $\hat{T}_N$ are kinetic energy operators for electrons and nuclei, $\hat{U}_{ee}$, is the Coulomb operator for electrons, and lastly, electron-nuclei, nuclei-nuclei interactions are captured with the potential energy operators $\hat{V}_{eN}$ and $\hat{V}_{NN}$, respectively. m_e is the electron mass, $\hbar$ the reduced Plank constant, e the electron charge and M_i the mass of nucleus I [36, 37]. Commonly, the Born-Oppenheimer approximation (BOA) is applied to simplify Equation (2.4). Loosely, it argues that due to the considerable dissimilar masses of the nuclei and electrons, the motions of those particles act on different timescales. The BOA then is a quasi-separable ansatz separating the total wave function $\Psi(\mathbf{r},\mathbf{R})$ into an electronic $\Phi(\mathbf{r},\mathbf{R})$ and nuclear wave function $\chi(\mathbf{R})$ [20]:

$$\Psi(\mathbf{r},\mathbf{R}) = \Phi(\mathbf{r},\mathbf{R})\chi(\mathbf{R}) \qquad (2.5)$$

The BOA introduces a parametric dependence on given nuclear coordinates. In DFT, for a given set of such coordinates, the electronic Hamiltonian is then solved. This leads to a simplification of the Hamiltonian and $\mathbf{R}$ is considered constant. We can write the electronic Hamiltonian [36]:

$$\hat{H}_e(\mathbf{r},\mathbf{R}) = \hat{T}_e(\mathbf{r}) + \hat{U}_{ee}(\mathbf{r}) + \hat{V}_{eN}(\mathbf{r},\mathbf{R}) \qquad (2.6)$$

Nevertheless, this simplification is not sufficient for systems with more than a few electrons, since the Schrödinger equation still depends on $3 \times N_e$ variables. DFT gives a way to calculate the electronic energy for such systems: The underlying Kohn-Sham formalism is that a fully interacting system is mapped onto a fictitious non-interacting system of electrons while the density remains the same. The energy of the non-interacting system can be calculated and to account for the interactions, one simply adds a correction term, the exchange-correlation functional [38, 39]. This enables one to solve the Schrödinger equation, and one can then make predictions about systems with an immense number of electrons. The DFT is based on the Hohenberg-Kohn theorems explained in the following.

2.1.1 Hohenberg-Kohn Theorems

The Hohenberg-Kohn Existence Theorem:

The first Hohenberg-Kohn Existence theorem states that the ground state electronic density $\rho(\mathbf{r})$ determines the external potential energy $\hat{V}_{ext}$, apart from a trivial additive constant [40, 41]. This is grounded in the fact that the integration of the electronic density $\rho(\mathbf{r})$ yields the total electronic charge, which equals the number of electrons N_e in a system [41]:

$$N_e = \int \rho(\mathbf{r}) d\mathbf{r} \tag{2.7}$$

The external potential $\hat{V}_{ext}$, which mostly consists of the charges and positions of the nuclei, is also given by the ground state electronic density $\rho(\mathbf{r})$. This relationship becomes evident since the nucleus is located at the maxima of the electron densities [36]. The time-independent Hamiltonian becomes:

$$\hat{H}_e(\mathbf{r}) = \hat{T}_e(\mathbf{r}) + \hat{U}_{ee}(\mathbf{r}) + \hat{V}_{ext}(\mathbf{r}) \tag{2.8}$$

where the kinetic operator $\hat{T}_e$ and the potential operator $\hat{U}_{ee}$ are known. This leads to the fact, that the electronic ground state density $\rho(\mathbf{r})$ determines the Hamiltonian and thus the wave function via the Schrödinger equation (see Equation (2.1)). The wave function becomes a functional of the density $\Phi = \Phi[\rho(\mathbf{r})]$, which leads to the conclusion that the expectation value of any operator acting on the wave function becomes a unique functional of the electronic density. Hence, the ground state electronic density $\rho(\mathbf{r})$ is adequate to fully determine all properties of the quantum-mechanical system as well as the electronic energy $E_e[\rho(\mathbf{r})]$ [37, 40, 41]. The first theorem of DFT serves as an existence theorem stating these principles. Yet, it does not offer a method for calculating the electronic ground state energy for a given system.

The Hohenberg-Kohn Variational Theorem

Secondly, the Hohenberg-Kohn Variational Theorem states that the ground state density can be obtained from the ground state energy functional since it adheres to the variational principle by variation of the electronic density [40, 41]. Specifically, this principle suggests that if an approximate and well-behaved electronic density is assumed, it infers a corresponding approximated wave function Ψ_{app} and an associated approximated Hamiltonian $\hat{H}_{app}$. Consequently, the computed energy expectation value derived from this approximated state will always be greater than

or equal to the actual energy of the system [36]:

$$\langle \Psi_{app} | \hat{H}_{app} | \Psi_{app} \rangle = E_{app} \geq E_0 \tag{2.9}$$

So that the functional $E[\rho(\mathbf{r})]$ has its minimum relative to variations of the electronic density $\rho(\mathbf{r})$ of the ground state electronic density $\rho_0(\mathbf{r})$ [37, 42, 43]:

$$E_0 = E[\rho_0(\mathbf{r})] = \min\{E[\rho(\mathbf{r})]\} \tag{2.10}$$

$$\frac{\partial E[\rho(\mathbf{r})]}{\partial \rho(\mathbf{r})} = \rho_0(\mathbf{r}) = 0 \tag{2.11}$$

2.1.2 Kohn-Sham Formalism

The Schrödinger equation can now be solved with the help of the density functional theory. For many electron systems that we usually face in surface science describing all the electron-electron interactions in a term is an impossibly difficult task. That is why the description of the Hamiltonian operator can be simplified by writing it as a sum of non-interacting one electron operators, the so-called Kohn-Sham (KS) operators $\hat{h}_i^{KS}$ [36, 37]:

$$\hat{H}_{KS} = \sum_{i=1}^{N_e} \hat{h}_i^{KS} \tag{2.12}$$

$$\hat{h}_i^{KS}(\mathbf{r}_i)|\Phi_i(\mathbf{r}_i)\rangle = \left(-\frac{\hbar^2}{2m_e}\nabla_i^2 + V_{ext}(\mathbf{r}) + V_H[\rho(\mathbf{r}_i)] + V_{xc}[\rho(\mathbf{r}_i)] \right) |\Phi_i(\mathbf{r}_i)\rangle = \epsilon_i |\Phi_i(\mathbf{r}_i)\rangle \tag{2.13}$$

$$V_H[\rho(\mathbf{r}_i)] = \int_j d^3\mathbf{r}_j \frac{e^2 \rho(\mathbf{r}_j)}{|\mathbf{r}_j - \mathbf{r}_i|} \tag{2.14}$$

$$V_{xc}[\rho(\mathbf{r}_i)] = \frac{\partial E_{xc}[\rho(\mathbf{r}_i)]}{\partial \rho(\mathbf{r}_i)} \tag{2.15}$$

The one-electron Kohn-Sham operator $\hat{h}_i^{KS}$ consists of a kinetic energy term $-\frac{\hbar^2 \nabla_i^2}{2m}$, an external potential term V_{ext} as previously described felt by the ith electron (generated by nuclei or external electromagnetic field) and effective potential terms consisting of the Hartree potential $V_H[\rho(\mathbf{r})]$ and the exchange-correlation potential $V_{xc}[\rho(\mathbf{r})]$ [37, 44, 45]. These one-electron operators then act each on a one-electron wave function that is just dependent on three space coordinates instead of a wave function that is dependent on $3 \times N_e$ coordinates. Now the wave function can also be written in terms of one electron Kohn-Sham wave functions $\phi(\mathbf{r})$ [36].

$$E_{N_e}[\rho(\mathbf{r})] = \sum_{i=1}^{N_e} \hat{h}_i^{KS} |\phi_1, \phi_2, ..., \phi_{N_e}\rangle = E_{N_e} |\phi_1, \phi_2, ..., \phi_{N_e}\rangle \tag{2.16}$$

2.1.3 Projector-Augmented Waves

In DFT, the KS-eigenfunctions are expanded by a so-called basis set, that converts the above wave equations into matrix equations involving discrete expansion coefficients. For molecular systems, it is common to use localized functions, e.g., atomic orbitals or Gaussian orbitals. For systems utilizing periodic boundary conditions, that we are particularly interested in, the choice at hand is plane waves. Our work uses projector-augmented waves, or in short PAW's [46] as implemented in the Vienna Ab initio Simulation Package (VASP) [4–6]. There are multiple reasons why it is favorable to use plane waves: i) These make it easy to transform from reciprocal to real space representation, ii) the control of basis set convergence is trivial; one has to converge the total energies as a function of the cut-off energy (the highest energy of a plane wave within the basis set). iii) It allows for simple calculation of the Hellmann-Feynmann forces acting on the atoms and molecules from the expectation value of the Hamiltonian. Lastly, iv) basis-set superposition errors are avoided [42]. The PAW method tries to combine the computational efficiency of the Vanderbilt-type [47] ultrasoft-pseudopotential methodology [48] and the accuracy of the linearized augmented-plane wave method [49]. In PAW, the nodal feature of the valence orbitals is included as well as the orthogonality between valence and core wave functions. The all-electron wave function $|\Phi\rangle$, which consists of orbitals, is derived from the pseudo-potential wave function $|\tilde{\Phi}\rangle$ by linear transformation [46, 50]:

$$|\Phi\rangle = |\tilde{\Phi}\rangle \sum_i (|\phi_i\rangle - |\tilde{\phi}_i\rangle)\langle\tilde{p}_i|\tilde{\Phi}\rangle \tag{2.17}$$

where $|\phi_i\rangle$ are the all electron partial waves, $|\tilde{\phi}_i\rangle$ are pseudo potential partial waves, $|\tilde{p}_i\rangle$ are the projector functions [46].

One can imagine that between the PAW-spheres, the pseudo-orbitals $|\tilde{\Phi}\rangle$ are identical to the exact orbitals $|\Phi\rangle$, whereas inside the spheres the pseudo-orbitals $|\tilde{\Phi}\rangle$ are rather inaccurate approximations of the exact orbitals. The second part of the equation is needed to map the auxiliary quantities $|\tilde{\Phi}\rangle$ onto the corresponding exact orbitals [51]. In VASP [4–6], the frozen core approximation is also additionally implemented to reduce computational cost. The core orbitals are fixed since they are usually chemically inactive [52–54].

2.1.4 Exchange-Correlation Functionals

Only the exchange-correlation functional $E_{xc}[\rho(\mathbf{r}_i)]$ in Equation (2.15) is hard to evaluate. It accounts for the remaining electronic energy that is not included in the non-interacting electrostatic and kinetic terms [55]. It consists of two terms:

Firstly, the quantum-mechanical Pauli and Coulomb correlations, and secondly, the correlation-kinetic effects [41].

Most modern functionals do not attempt to solve this term. Instead, they approximate it through, e.g., trying to add the kinetic energy difference between the non-interacting and interacting system separately or adding empirical parameters [36, 55]. The Jacob's ladder describes the levels of approximations included in the functionals [56]. The lowest rung is the local density approximation (LDA). The exchange-correlation energy density at each point in space depends only on the electron density at that specific point, reflecting the behavior of a uniform electron gas. It is used for metals and in material sciences but is usually a bad approximation for chemical applications. The next rung includes generalized gradient approximations (GGAs). These formulae use the density and its gradient, which leads to a higher computational cost, but also to a more accurate solution [57, 58]. Because of the great trade-off between accuracy and efficiency, one can find these types of exchange-correlation functionals used in surface science. Especially Perdew-Wang 1991 (PW91) [57], Perdew-Burke-Ernzerhof (PBE) [58] and revised Perdew-Burke-Ernzerhof (RPBE) [59] functionals can be found in many theoretical works investigating surfaces and interfaces. Using these common functionals leads to similar errors for adsorption energies as compared to experimental adsorption energies [60]. It is well known that RPBE leads to slightly weaker adsorption energies while PBE and PW91 tend to display overbinding of adsorbates [39]. Another noteworthy functional is the Bayesian Error Estimation Functional with van der Waals correlation (BEEF-vdW) [61] functional that allows for error estimation through using an ensemble of GGA functionals. The next step is the meta-GGAs, which include the dependence of the exchange-correlation energy on the Kohn-Sham kinetic energy density. An example would be the Tao–Perdew–Staroverov–Scuseria (TPSS) [62] functional, but these are less common because their accuracy is not necessarily improved as compared to GGA functionals [39]. The fourth category of functionals is the hybrid-functionals, which incorporate a part of exact exchange as calculated in Hartree-Fock theory in combination with GGAs. Although the accuracy is enhanced, these functionals are often too expensive to use for surface science problems [39].

In the following work, we make use of the RPBE exchange-correlation functional [59] that is adapted to specifically address limitations in surface and interfacial calculations and how we are conducting them [39]. It is comparable to the PBE [58] functional, but the parameter κ differs to improve the description of atomic total energies and molecular atomization energies [59]. For PBE, κ equals 0.804, while in

RPBE, we have $\kappa = 1.245$. The exchange-correlation energy is written [59]:

$$E_{xc}[\rho(\mathbf{r}_i)] = \int \rho(\mathbf{r})\epsilon_{xc}(\mathbf{r})d(\mathbf{r}) = \int \rho(\mathbf{r})\epsilon_{xc}^{\mathrm{LDA}}(\rho(\mathbf{r})F_{xc}(s(\mathbf{r}))d(\mathbf{r}) \tag{2.18}$$

where $\epsilon_{xc}^{\mathrm{LDA}}$ is the local exchange energy density from the LDA, which consists of an exchange-correlation energy per particle in a uniform electron gas [63]. The reduced density gradient s is defined as [59] :

$$s(\mathbf{r}) = |\nabla\rho(\mathbf{r})|/[2(3\pi^2)^{1/3}\rho(\mathbf{r})^{3/4}] \tag{2.19}$$

$$F_{xc}(s) = 1 + \kappa - \frac{\kappa}{1 + \mu_{xc}s^2/\kappa} \tag{2.20}$$

Lastly, $F_{xc}(s)$ is the local exchange enhancement factor and μ_{xc} is a constant.

Another important point is that exchange-correlation functionals often do not include long-range dispersion (van-der-Waals) interactions. The following work includes a correction to account for these long-range dispersion effects: We utilize the DFT-D3 method by Grimme *et al.* [64, 65] that adds a van-der-Waals dispersion energy correction term.

2.1.5 K-Points

In plane-wave DFT, a **k**-point grid specifies the Bloch vectors to sample the Brillouin zone. In our work, we focus on a regular mesh, the number of **k**-points define the number of subdivisions the given lattice vector is divided. To be more specific we use a Γ-centered Monkhorst-Pack mesh as implemented in VASP [4–6, 66]: This method gives a set of special points in the Brillouin-zone which is efficient when integrating periodic functions of the wave vector [66, 67]:

$$\mathbf{k} = \sum_{i=1}^{3} \frac{n_i + s_i}{N_i}\mathbf{b}_i \tag{2.21}$$

where N_i is the ith subdivision, s_i defines the corresponding optional shift, and $\mathbf{b}_i$ is the corresponding lattice vector. A good number of **k** can be chosen by converging the total energy with increasing **k**-points.

2.1.6 Smearing Function

The electronic density can be calculated via the Kohn-Sham eigenvectors:

$$\rho(\mathbf{r}) = \sum_i f_i|\phi_i(\mathbf{r})| \tag{2.22}$$

where f_i is the occupation number that either equals 1 for an occupied state or 0 for an unoccupied state. For metallic systems, it is common to use a smearing function around the Fermi level to enable fractional occupation numbers [68].

$$\rho(\mathbf{r}) = \sum_i \int_{\mathbf{BZ}} f_{i\mathbf{k}} |\phi_{i\mathbf{k}}(\mathbf{r})(\mathbf{r})| d\mathbf{k} \tag{2.23}$$

where the the occupation number f_i is now exchanged by a smearing function $f_{i\mathbf{k}}$ [68]. There are various smearing functions $f_{i\mathbf{k}}$ commonly used: Fermi smearing, Gaussian smearing, cold smearing or tetrahedron method [69]. In our work, we utilize Gaussian smearing.

2.1.7 Self-Consistent Field Method

Now that the theoretical groundwork has been introduced, the ground state density can be calculated numerically. The Hohenberg-Kohn variational theorem (see Section 2.1.1) allows the use of an iterative approach to reach the ground state electronic energy: The KS-equations are solved iteratively towards so-called self-consistency with the help of the self-consistent field (SCF) method [70]. A SCF cycle starts with an initial guess of the density to obtain the starting wave functions. In the second step, the KS-Hamiltonian is calculated, and the KS-equations are solved. Afterwards, a new electron density is calculated. Now, the new values are compared with the previous guess, and if convergence isn't reached (usually defined by an electronic energy convergence parameter), the old and new parameters are mixed, and the second cycle starts at step two. This is continued until convergence is reached and the newest electronic ground state density is considered the solution [70].

2.2 *Ab Initio* Molecular Dynamics

Nowadays, molecular dynamics is extensively used to solve a wide range of problems in chemistry and material science. It encompasses both equilibrium thermodynamics and dynamic properties computed at finite temperatures. In molecular dynamics, the Newtonian equations of motion are solved for a system with a specified initial state and defined boundary conditions. At the core of any molecular dynamics simulation lies the question of how to define interatomic interactions. In classical molecular dynamics, these forces are described by force fields. However, these force fields become inadequate when dealing with more "chemically complex" systems where a variety of atoms or molecule types give rise to a multitude of different interatomic interactions or where the electronic structure and bonding pattern vary throughout the simulation, i.e., where bond making and breaking occurs [71]. In electrochemistry,

not only do we face a variety of atoms and molecule types, but charging effects also play a major role. This is where *ab initio* molecular dynamics comes into play. Here, we still have finite temperature dynamical trajectories, while the forces are generated "on the fly" by DFT single-point calculations. This approach allows for the incorporation of effects of chemical bond breaking and forming, as well as electronic polarization effects into the molecular dynamics picture. One can also view this as a shift from approximating on the level of selecting the model potential to the level of selecting a particular approximation for solving the Schrödinger equation [71, 72].

2.2.1 Quantum Molecular Dynamics

Since we now want to take a look at the dynamics of the system, we can write the Hamiltonian that includes both nuclear and electronic components following Equations (2.4) and (2.6) [20]:

$$\hat{H}(\mathbf{r},\mathbf{R}) = \hat{T}_N(\mathbf{R}) + \hat{H}_e(\mathbf{r},\mathbf{R}) \tag{2.24}$$

with the electronic Hamiltonian consisting of the electronic kinetic energy and all the Couloumbic interactions (electrons-electrons and electrons-nuclei, respectively): $\hat{H}_e = \hat{T}_e(\mathbf{r}) + \hat{U}_{ee}(\mathbf{r}) + \hat{V}_{eN}(\mathbf{r},\mathbf{R})$. The dynamics of the system can be defined by the time-dependent Schrödinger equation that includes a time-dependent wave function $\Psi(\mathbf{r},\mathbf{R};t)$ [20]:

$$i\hbar\frac{\partial}{\partial t}\Psi(\mathbf{r},\mathbf{R};t) = \hat{H}\Psi(\mathbf{r},\mathbf{R};t) \tag{2.25}$$

At a fixed time t and a fixed nuclei configuration $\mathbf{R}$, the eigenstates of the electrons can be obtained via the stationary or time-independent Schrödinger equation (as already described in Section 2.1):

$$\hat{H}_e\Phi_k(\mathbf{r},\mathbf{R}) = E_k\Phi_k(\mathbf{r},\mathbf{R}) \tag{2.26}$$

where a selected set of quantum numbers describes the electronic state k. The total wave function can be expanded via the Born-Huang ansatz [20, 73]:

$$\Psi(\mathbf{r},\mathbf{R};t) = \sum_{l=0}^{\infty}\Phi_l(\mathbf{r},\mathbf{R})\chi_l(\mathbf{R};t) \tag{2.27}$$

Note here, that χ_l consists of time-dependent coefficients in this expansion. Now, we can write the electronic contribution as a stationary Schrödinger equation, whilst the time-dependent part is included in χ_k, which is a set of nuclear wave functions for a selected electronic state k. After substitution of Equation (2.27) into the time-dependent Schrödinger Equation (2.25) and an integration over the electronic

coordinates $\mathbf{r}$, we arrive at [20, 74]:

$$i\hbar\frac{\partial\chi_k(\mathbf{R};t)}{\partial t} = \left[\hat{T}_N + E_k(\mathbf{R})\right]\chi_k + \sum_l \mathcal{C}_{kl}\chi_k(\mathbf{R};t) \tag{2.28}$$

where the nuclear wave functions are coupled to the electronic wave function through the coupling coefficient $\mathcal{C}_{kl}$, which includes the electronic wave function Φ_k [74]. To solve this system, two main approximations have to be made: the adiabatic and the BOA approximation.

2.2.2 Adiabatic and Born-Oppenheimer Approximation

The first approximation is the adiabatic approximation, which assumes that the electronic wave functions adapt quasi-instantaneously to changes in the nuclear configuration. This assumption relies on the fact that electrons, being much lighter, respond almost immediately to the movement of the heavier nuclei I. The gradient of the electronic wave function with respect to the nuclear coordinates is therefore zero [74]:

$$\nabla_I \Phi_I = 0 \tag{2.29}$$

This approximation lets us neglect the non-adiabatic coupling term $\mathcal{C}_{kl}$. The motion of the nuclei can be treated without considering the changes in the electronic state's gradient.

This leads us to the BOA (see Section 2.1). It states that the total wave function can be separated into a product of the electronic and nuclear wave function as seen in Equation (2.5), where the nuclear wave function here depends also on time t. Equation (2.28) can be simplified to the quantum-mechanical equation of motion of the nuclei in the BOA:

$$i\hbar\frac{\partial\chi_k(\mathbf{R};t)}{\partial t} = \left[\hat{T}_N + E_k(\mathbf{R})\right]\chi_k(\mathbf{R};t) \tag{2.30}$$

The analogous quantum-mechanical equation of motion for the electronic degrees of freedom can be written [20]:

$$i\hbar\frac{\partial\Phi(\mathbf{r},\mathbf{R};t)}{\partial t} = \hat{H}_e\Phi(\mathbf{r},\mathbf{R};t) \tag{2.31}$$

where the electronic wave function Φ can be shown in the basis of electronic states with coefficients $c_l(t)$ that depict the occupation numbers of the states:

$$\Phi(\mathbf{r},\mathbf{R};t) = \sum_{l=0}^{\infty} c_l(t)\Phi_l(\mathbf{r},\mathbf{R};t) \tag{2.32}$$

Solving Equations (2.30) and (2.31) gives the quantum dynamics of the nuclei and electrons, respectively. However, these need to be further simplified to make the problem tractable [20]. The methods arising are called *ab initio* molecular dynamics (AIMD).

2.2.3 Ehrenfest Dynamics

An important approximation in AIMD is that the average motion of the nuclei can be described by Newton's classical equations of motion, neglecting the quantum effects of the heavy nuclei. In Ehrenfest dynamics, the quantum mechanical motion of the electrons is solved at every step via Equation (2.31). The wave function is then used to compute the forces acting on the nuclei. The potential guiding the classical motion of the nuclei is given by the expectation value of the electronic Hamiltonian [20]:

$$M_I \ddot{\mathbf{R}}_I = -\nabla_I \int d\mathbf{r} \Phi^* \hat{H}_e \Phi = -\nabla_I \langle \hat{H}_e \rangle \tag{2.33}$$

2.2.4 Born-Oppenheimer Dynamics

In Born-Oppenheimer Dynamics, an additional assumption is made: The electronic wave function Φ is in its ground state, defined by the adiabatic wave function Φ_0. Equation (2.32) is simplified to just one term. Adding all approximations together, the equation of motions can be written as [20]:

$$M_I \ddot{\mathbf{R}}_I = -\nabla_I \min_{\Phi_0} \{ \langle \Phi_0 | \hat{H}_e | \Phi_0^* \rangle \} \tag{2.34}$$

$$E_0 \Phi_0 = \hat{H}_e \Phi_0 \tag{2.35}$$

The dynamics of the nuclei can be treated classically on the ground state electronic potential surface, and we get the electronic information from DFT calculations "on the fly" (see Section 2.1). The forces are also obtained via DFT calculations with the help of the Hellmann-Feynmann theorem [74]:

$$-\nabla_I \langle \Phi_0 | \hat{H}_e | \Phi_0 \rangle \approx -\langle \Phi_0 | \nabla_I \hat{H}_e | \Phi_0 \rangle \tag{2.36}$$

This simplification can be made because, in the ground state, the wave function has been optimized to minimize energy. Therefore, small changes in the positions of the nuclei do not significantly change the wave function. As a result, the derivative (or gradient) of the wave function with respect to nuclear positions is negligible, allowing the expression to simplify.

In this work, the AIMD simulations are performed using the Born-Oppenheimer

approach, incorporating all previously discussed approximations [74]. AIMD is a broader term, encompassing not only Ehrenfest dynamics and BOMD but also non-ground-state methods like e.g. Car-Parrinello Molecular Dynamics, which are not relevant to this work. Therefore, from now on, when the term AIMD is used, it will specifically refer to the BOMD methodology, as implemented in the code we are using: VASP [4–6].

2.2.5 Verlet Integration

The equation of motion needs to be further integrated to determine the new positions of the nuclei. There are several numerical integration methods available, but in our work, we focus on the Verlet Integrator [75] as implemented in VASP [4–6, 42]. To be more concise, VASP implements the leapfrog method, which is very similar to the velocity Verlet algorithm, as both give the same set of new positions. The main difference lies in the timesteps where the velocities are updated. In the velocity Verlet method, the positions and velocities are calculated for the same timestep, denoted as $t + \delta t$. When using the leapfrog method (as implemented in VASP), the positions and velocities can be given for different timesteps, for example, $t + \delta t$ and $t + \frac{1}{2}\delta t$, respectively. The corresponding equation for updating the positions is:

$$\mathbf{R}_I(t + \delta t) = \mathbf{R}_I(t) + V_I(t) + \frac{1}{2}A_I(t) \tag{2.37}$$

where V_I is the velocity and A_I is the acceleration.

2.2.6 Nosé-Hoover Thermostat

To go to realistic ensembles, one has to go beyond the view of an isolated system as previously. To achieve this, we work in the canonical ensemble, also called the NVT ensemble, where we control the number of particles N, the volume V, and lastly, the temperature T.

In the canonical ensemble, we simulate an isothermal system, where the temperature is controlled and maintained. This is done by introducing a thermostat, which allows the system to exchange energy with an external heat bath. One of the most widely used thermostats is the Nosé-Hoover thermostat [76–79]. It works by introducing an additional degree of freedom that represents the coupling between the system and the heat bath. This extra degree of freedom adjusts the particle velocities in the system, thereby controlling the temperature. A fictional dynamical variable, whose physical meaning is the friction $\mathcal{J}$, is included proportional to the velocity into the

equation of motion [80]:

$$M_I \ddot{\mathbf{R}}_I(t) = F_I - \mathcal{J} M_I \dot{\mathbf{R}}(t) \tag{2.38}$$

$$\dot{\mathcal{J}} = \frac{[(K/K_0) - 1]}{\mathcal{T}} \tag{2.39}$$

where F_I denotes the force on nuclei I, $\mathcal{T}$ is a phenomenological relaxation time. The friction coefficient $\mathcal{J}$ is defined by a feedback equation that controls the kinetic energy K to make its time average equal to K_0 [80]. This enables adjustment of the kinetic energy to maintain a constant temperature, or rather to keep it fluctuating around a defined target [81].

2.3 Practical implementation

2.3.1 Density Functional Theory

There are several DFT codes available to use, we choose the Vienna Ab initio Simulation Package (VASP) [4–6] that is based on the PAW method [46, 50] (see Section 2.1.3), a plane wave basis set in periodic boundary conditions. We follow the technical framework set by Heenen *et al.* [82]: We use a cut-off of 400 eV, a 4×3×1 Γ-point centered Monkhorst-Pack **k**-point grid to sample the Brillouin zone (see Section 2.1.5) and a Gaussian smearing of 0.1 eV (see Section 2.1.6). As mentioned, all our calculations use the revised RPBE [59] exchange-correlation functional and D3 dispersion correction scheme, to account for dispersion effects [64, 65] (see Section 2.1.4). We use a convergence threshold for the SCF cycle of less than 10^{-6} eV (see Section 2.1.7). It has been shown in previous work that this set-up performs well for similar systems as ours [83, 84]. Furthermore, to account for dipole effects, we include dipole corrections as common practice for theoretical surface science calculations [85].

Since O_2 is paramagnetic as explained in greater detail in Section 3.4, spin polarization is included in all calculations with O_2. To achieve self-consistency, the standard Pulay-mixing scheme with Kerker preconditioning [5] was used:

$$\mathbf{G}_k^1 = A \frac{k^2}{k^2 + k_0^2} \tag{2.40}$$

where k represents the reciprocal space vector. We conducted stability tests, looking at the stability of the magnetic moment, making sure it took on realistic values ($< 2\mu_B$). For Au(111), we found that choosing a linear mixing factor for the magnetization density $A = 0.1$ with a cut-off wavevector for the Kerker mixing scheme of $k_0^2 = 0.5$ led to enhanced stability and convergence of the electronic ground states.

For Pt(111), these values changed to $A = 2.0$ and $k_0^2 = 0.25$.

All calculations are conducted with three layers of metal (here Au(111) or Pt(111)) in a (non-symmetric) three-layered 3×4 supercell. In order to model a bulk-like behavior of the lower metal layer, we keep the bottom two layers fixed. We choose a 14 Å vacuum region to separate the periodic images in the z-direction perpendicular to the surface. For Au(111) a lattice constant of 4.167 Å [82] was used, while for Pt(111), a lattice constant of 3.934 Å was used, obtained from a bulk-Pt DFT-geometry optimization. Geometry optimizations give new lattice and atomic positions that optimize the energy of a system, whereas this is usually limited to finding the closest local minimum [86, 87]. As implemented in VASP [4–6], we utilize the conjugate gradient algorithm for that purpose. The structure is hereby optimized along a specific search direction. The initial search direction stems from the DFT-calculated forces and stresses. The following steps are conjugate (perpendicular) to the prior step. It starts with a trial step, whereas a DFT-single point calculation gives new entries, forces, and stresses. Based on the change in energy and forces, a polynomial is fitted to determine the expected minimum, whereas new energy forces and stresses are calculated. Depending on the outcome, if the new forces/stresses parallel to the previous ones vanish, a new trial step is performed. Otherwise, the line minimization is improved. This continues until energy convergence is reached (in our work within 0.01 eV), allowing us to obtain the closest energetically stable structure[86, 87].

2.3.2 *Ab Initio* Molecular Dynamics

We set up our *ab-initio* molecular dynamics (AIMD) simulation following the framework of Heenen *et al.* [82]. AIMD simulations were conducted using the VASP package [4–6] utilizing the same parameters and unit cells as for the DFT calculations (described in the previous section). The simulations were performed in the NVT ensemble at 300 K, using a Nosé-Hoover thermostat (see Section 2.2.6) with a damping coefficient of 40 fs and a timestep of 1 fs. An initial equilibration phase of 5 ps was implemented for all simulations, during which data were not collected for subsequent analysis.

In all AIMD simulations, approximately three layers of interfacial water—comprising 24 H_2O molecules—were placed atop the 3×4 metal surface, keeping the 14 Å vacuum region in the z-direction perpendicular to the surface. To incorporate interfacial water onto the OH*-covered Pt(111) surfaces, we utilized water configurations from equilibrated AIMD snapshots of the clean surface. These configurations were shifted upward by 0.2 Å along the z-axis to accommodate the protruding OH* species and then re-equilibrated.

The initial OH*-covered Pt(111) model was constructed by exploring various configurations corresponding to a 5/12 monolayer (ML) coverage of OH* within a vacuum DFT cell. This involved placing OH* species on different top sites of the Pt(111) surface and performing geometry optimizations to identify the most energetically favorable structures. The configuration with the lowest energy was selected as the starting point for the AIMD simulations.

During the subsequent AIMD runs, we observed proton exchange between the initial OH* species and co-adsorbed H_2O* molecules that spontaneously occupied some of the remaining vacant top sites. This observation led us to conclude that the specific initial configuration of the 5/12 ML OH* coverage was not critical. Therefore, no further stability tests were conducted. Consequently, most of the trajectories were initialized using equilibrated AIMD snapshots from previous simulations, with the five OH* species randomly distributed on the surface, and all co-adsorbed H_2O* molecules were removed.

2.4 Modelling the Electrified Metal/Water Interface

In our pursuit to describe the electrochemical interface, one has to take the effects of the electric fields and water molecules into account. In this work, we use three different methods to approximate the electrified metal/water interface as schematically shown in Figure 2.1:

- **Saw-tooth potential in vacuum** calculations, where an electric field is applied to static DFT calculations [88, 89].
- **Implicit solvation** calculations, where solvation is applied on the level of a continuous polarizable medium and charge is added through adding countercharges into the continuum [90].
- **Explicit solvation AIMD** simulations, where explicit water is added. Charge effects are simulated by adding re-parametrized hydrogen atoms into the simulation.

The saw-tooth potential in vacuum, as well as the implicit solvation model, represent computationally efficient, yet static modeling methods that will be explained in detail in Section 2.4.1 and Section 2.4.2, respectively. Here, the most energetically favored state is given by a DFT geometry optimization calculation, whereas finite-temperature corrections are added as a post-processing step (see Section 3.3). The third method we use is a finite-temperature AIMD, where we get the full dynamic picture with explicit water and a charged interface as explained in Section 2.4.3.

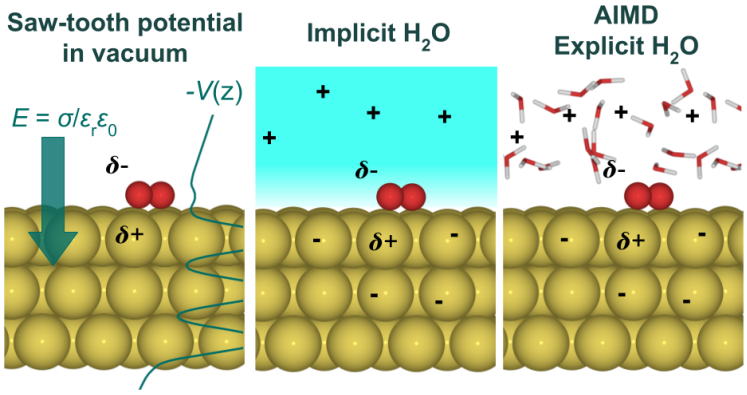

Figure 2.1: Schematic representation of the three main approximation methods used: Saw-tooth potential in vacuum, implicit solvation, and AIMD with explicit water.

To compare the three double-layer models that we introduce, it becomes valuable to be able to convert between the (constant) interfacial field $\vec{E}$ introduced via the applied saw tooth potential, and the (effective) surface charge density σ controlled directly through excess charge in the implicit solvation or AIMD models. Additionally, we want to be able to also convert to potential vs. SHE or potential vs. PZC to be able to show that we simulate close to realistic ORR conditions. For this conversion, we assume that the double layer at the flat single-crystal surface behaves like a simple parallel-plate capacitor that can be related to the (absolute) electrode potential U_{SHE} according to Ref. [91]:

$$\vec{E} = \frac{\sigma}{\epsilon_r \epsilon_0}\,\hat{\mathrm{z}} = \frac{C\,(U_{\mathrm{SHE}} - U_{\mathrm{PZC}})}{\epsilon_r \epsilon_0}\,\hat{\mathrm{z}} \tag{2.41}$$

$$U_{\mathrm{SHE}} = \frac{\sigma}{C} + U_{\mathrm{PZC}} \tag{2.42}$$

where ϵ_0 is the vacuum permittivity ($=8.85\mathrm{x}10^{-12}\,\mathrm{Fm}^{-1}$), and ϵ_r the dielectric constant of interfacial water which we set here to 1.5 as this is in line with values reported in the literature [92, 93]. We further use the experimental $U_{\mathrm{PZC}} = 0.5$ V vs. SHE for the PZC of Au(111) and $U_{\mathrm{PZC}} = 0.3$ V vs. SHE for the PZC of Pt(111) [94]. A constant $C = 25\,\mu\mathrm{F/cm}^2$ value for the Helmholtz capacitance is approximated for simplicity [91, 95–98]. Assuming the same capacitance for the clean and covered metal surfaces means that any possible adsorbate-induced changes to the work function are inherently ignored. We stress that the conversion between σ, $\vec{E}$, and potential should only be considered with caution and only tentatively. Additionally, it is important to consider that the present constant-charge approach should not be confused with so-called grand-canonical DFT simulations which give a more exact representation of reaction energies at a constant applied potential [99]. Another ap-

proximation we make is that we assume the same U_{PZC} for the clean Pt(111) as well as the OH*-covered Pt(111). But since we observe potential independence for most key target properties for the Pt-based systems, as will be discussed in Chapter 5, we expect that this assumption is unlikely to change the main qualitative conclusions of this work.

In the following, we further introduce the three different modeling approaches to approximate the electrified metal/water interface: Saw-tooth potential in vacuum, implicit solvation, and AIMD.

2.4.1 Saw-Tooth Potential in Vacuum

The first method we used to approximate electric field effects is the most simple one: A saw-tooth potential is applied to a static DFT calculation as shown in Figure 2.1. This method is implemented in VASP and gives a constant electric field $\vec{E}$ across the simulation cell in the z-direction. This method is as cheap as a normal non-electrified DFT calculation. Geometry optimization was performed for each applied field strength, where we scanned a range of $-1.0 < |\vec{E}| < 1.0$ V/Å. When going to stronger fields, the calculations become unstable due to the electronic density starting to "leak" from the slab to the edge of the simulation cell. The geometry was optimized until the forces were less than 0.01 eV/Å for each applied field. In order to find a stable minimum under all field conditions, we restricted the spin to 0 μ_{B}. Therefore, by construction, all our static calculations represent the fully chemisorbed O_2* state. To be more concise, we obtain the peroxo O_2* state that is described in detail in Section 3.4.

2.4.2 Implicit Solvation

Secondly, the implicit solvation method is employed. This accounts for a surrounding liquid electrolyte on the level of a continuous polarizable medium [90], as illustrated in Figure 2.1. Again, it is cheap to apply, comparable to a saw-tooth potential in a vacuum. The underlying concept is to employ a coarse-grained approach to model water solvation at the metal catalyst. Moreover, it is possible to charge the interface by explicitly modifying the number of electrons in the system, which is represented by the equation $n_e = n_e^{(\mathrm{neutral})}$. The counter-charge is placed in the continuum considering an electrolyte model, in the simplest case, e.g., by solving the linearized Poisson-Boltzmann equation, to keep the overall cell charge neutral. In our research, we utilize the polarizable continuum model, implemented in VASPsol [100–102], to ascertain the O_2 adsorption energies under varying charging conditions. Further information on how the O_2* adsorption energy is calculated can be found in Section

3. In order to model the solvation of water, VASPsol introduces an electrolyte filling of the vacuum region, with a relative permittivity of 78.4, which is consistent with the value observed in bulk water. To accurately represent the ionic environment, we selected a Debye screening length of $\lambda_{\mathrm{D}} = 3$ Å, which corresponds to a 1 M concentration of cations. This parameter is crucial for modeling the electrostatic interactions in the electrolyte, yet our findings indicated that variations in λ_{D} did not significantly affect the results. Similarly, like potential in vacuum calculations, geometry optimizations were performed for each applied charge. These optimizations were performed using the same settings as those employed with the saw-tooth potential method.

We expand the vacuum region for the implicit solvation calculations to 24 Å so that we can reduce the interactions between counter charges of two slabs. Considering the slab's asymmetric nature, it was determined that only half of the excess charge should be accounted for as surface charge density. The surface charge density was then calculated using the following formula:

$$\sigma = -e\delta n_e / 2A_{\mathrm{cell}} \tag{2.43}$$

where δn_e is the added or removed fraction of electrons, e is the electron charge and A_{cell} is the cell area ($A_{\mathrm{cell}} = 90.28$ Å^2 for Au(111) and $A_{\mathrm{cell}} = 80.42$ Å^2 for Pt(111)).

2.4.3 Explicit Solvation AIMD

Lastly, the most expensive yet accurate method to model the electrified metal/water interface is *ab initio* molecular dynamics simulations. This method is dynamic, we now have a time evolution of our system. Furthermore, we add explicit water molecules to our simulation cell: 24 H_2O molecules which corresponds to roughly three "layers" of interfacial water on top of the surface slab. Multiple independent simulation runs were initiated for each specified surface charge in the presence and absence of oxygen to explore different local minima of the H_2O solvent configurations. To charge the interface, randomly selected H atoms of the H_2O solvent are described with re-parametrized PAW potentials (included in the standard VASP distribution [103]) of 1.25 or 0.75 valency. The extra -0.25 or missing +0.25 electron charge (e) and multiples thereof are automatically added to or subtracted from the metal Fermi levels, depending on whether we want to model reducing or oxidative conditions, respectively. This happens automatically during the DFT SCF procedure to ensure the overall charge neutrality of the unit cell.

The additional valence electronic density (which balances the extra core charge) largely localizes in the metal slab. Some charge, however, remains on the positively

charged H atoms. This remaining electron density partly screens the introduced core charge and does not effectively contribute to the charging of the interface. Using Bader charge analysis [104–107] we found that the remaining charge is constant on every extra core charge, proportional to 0.34 e per added electron for the MD runs with only water and 0.31 e per added electron when O_2 is present for Au(111). We use the value from the trajectories including only water (without O_2) and estimate the effective counter-charge per modified H atom $0.25 \cdot (1 - 0.34) = 0.165$ e. We therefore consider our surface charge density to be $\sigma = -0.165n/A_{\text{cell}}$, where n is the number of modified H atoms and A_{cell} the area of the slab. We find similar behavior for the Pt(111) surface.

With this approach, it is important to ensure that the re-parametrized H atoms - which are effectively $H^{\pm\delta}$ ions - do not influence the surface chemistry that we are interested in. Figures 2.2 - 2.3 show that these atoms are mobile within the H_2O solvent and thus unlikely to be involved in specific interactions with the O_2 adsorbate on the Au(111) surface. Each species is normalized to its own total probability; otherwise, the contribution from re-parameterized hydrogen atoms would be too small to detect (i.e., if normalized against the total density of all species).

For Pt(111), as illustrated in Figures 2.4 - 2.7, mostly these atoms remain mobile within the H_2O solvent matrix, suggesting that they do not engage in specific interactions with the O_2* adsorbate on the metal surface. Yet, the re-parametrized H atoms can also be found at the interface, which might become especially problematic if the species that carries the re-parametrized H adsorbs at the surface. We have investigated this possibility and found that only a very small subset of the data is affected ($< 0.06\%$) that does not affect our results significantly (O_2* adsorption energy is changed by < 0.02 eV).

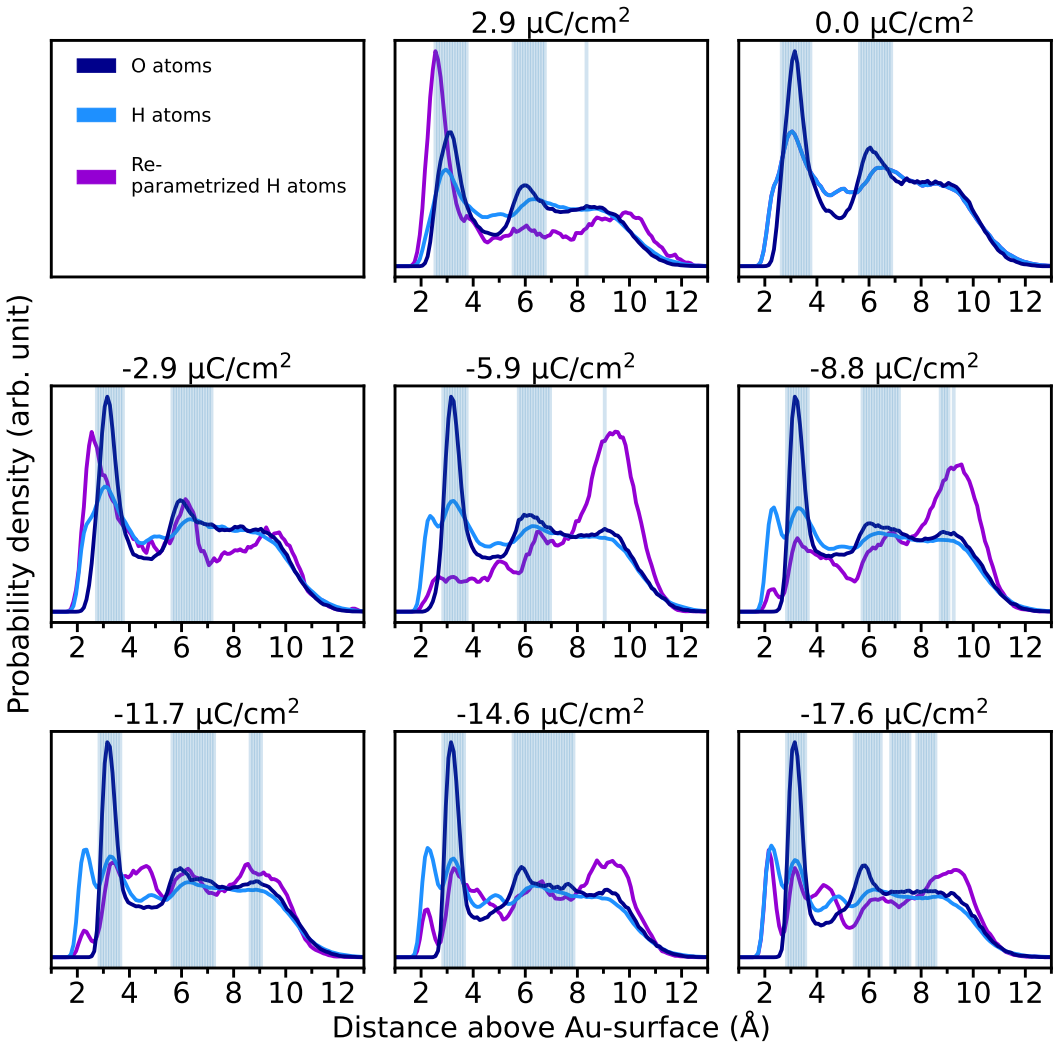

Figure 2.2: Average atomic densities along the surface normal as predicted from AIMD simulations of Au(111) + 24 H_2O. Different colored lines correspond to O atoms (dark blue), H atoms (blue), and re-parametrized H atoms (purple) in the H_2O solvent. The blue areas mark regions of interfacial (structured) water with density > 1 g/cm^3, i.e. larger than that of bulk H_2O. Each species is normalized to its own total probability. Different panels correspond to varying (effective) surface charge density, as noted on top.

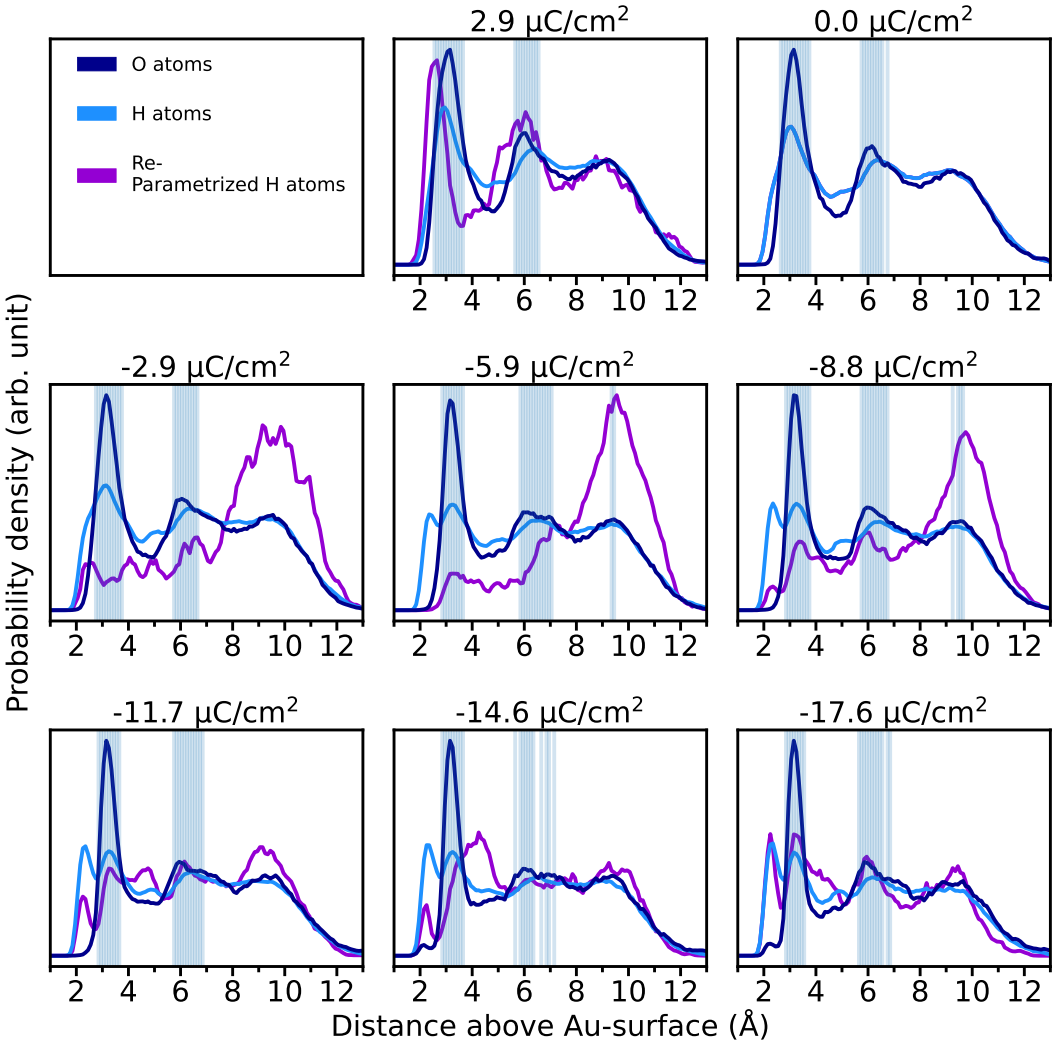

Figure 2.3: Same as Fig.2.2, but for Au(111) + 24 H_2O + O_2.

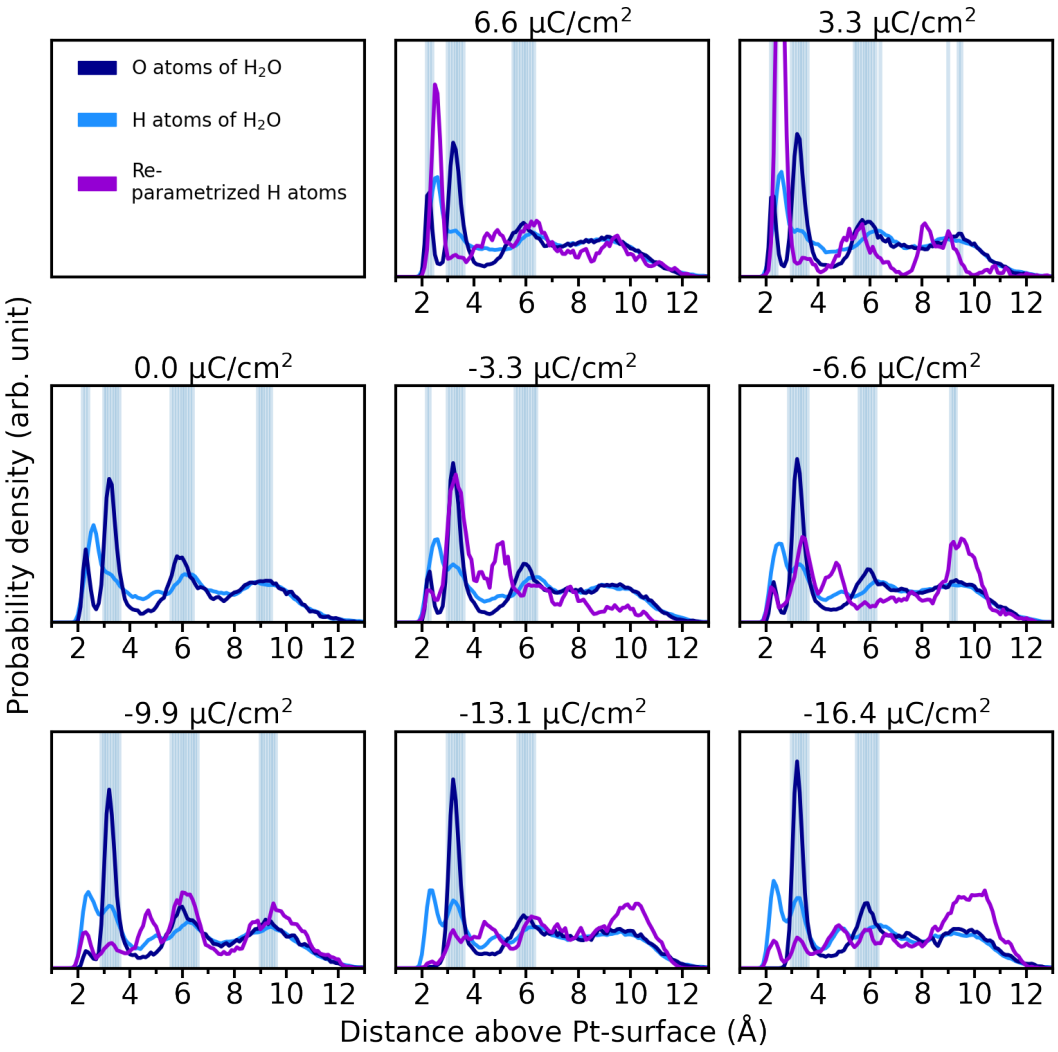

Figure 2.4: Same as Figure 2.2, but for Pt(111) + 24 H_2O.

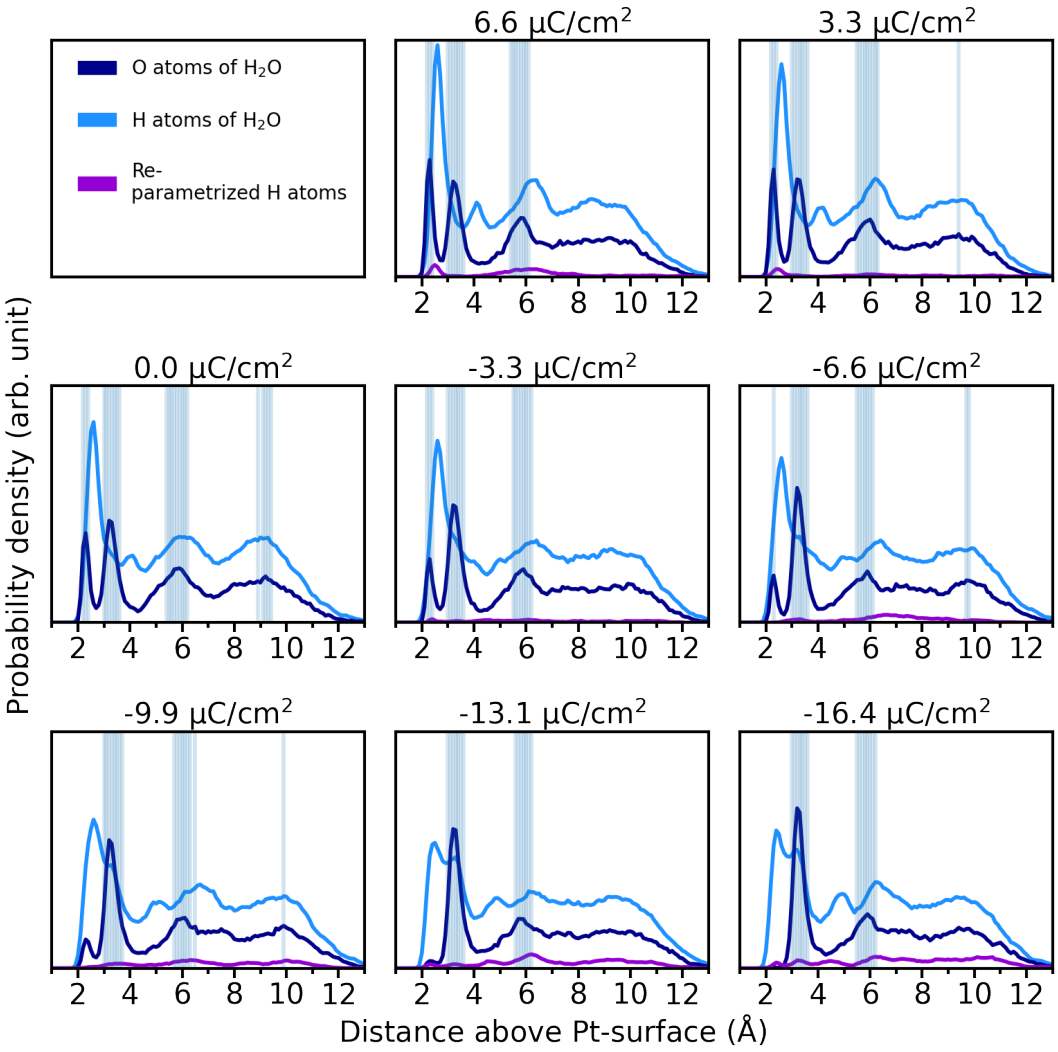

Figure 2.5: Same as Figure 2.2, but for Pt(111) + 24 H_2O + O_2*.

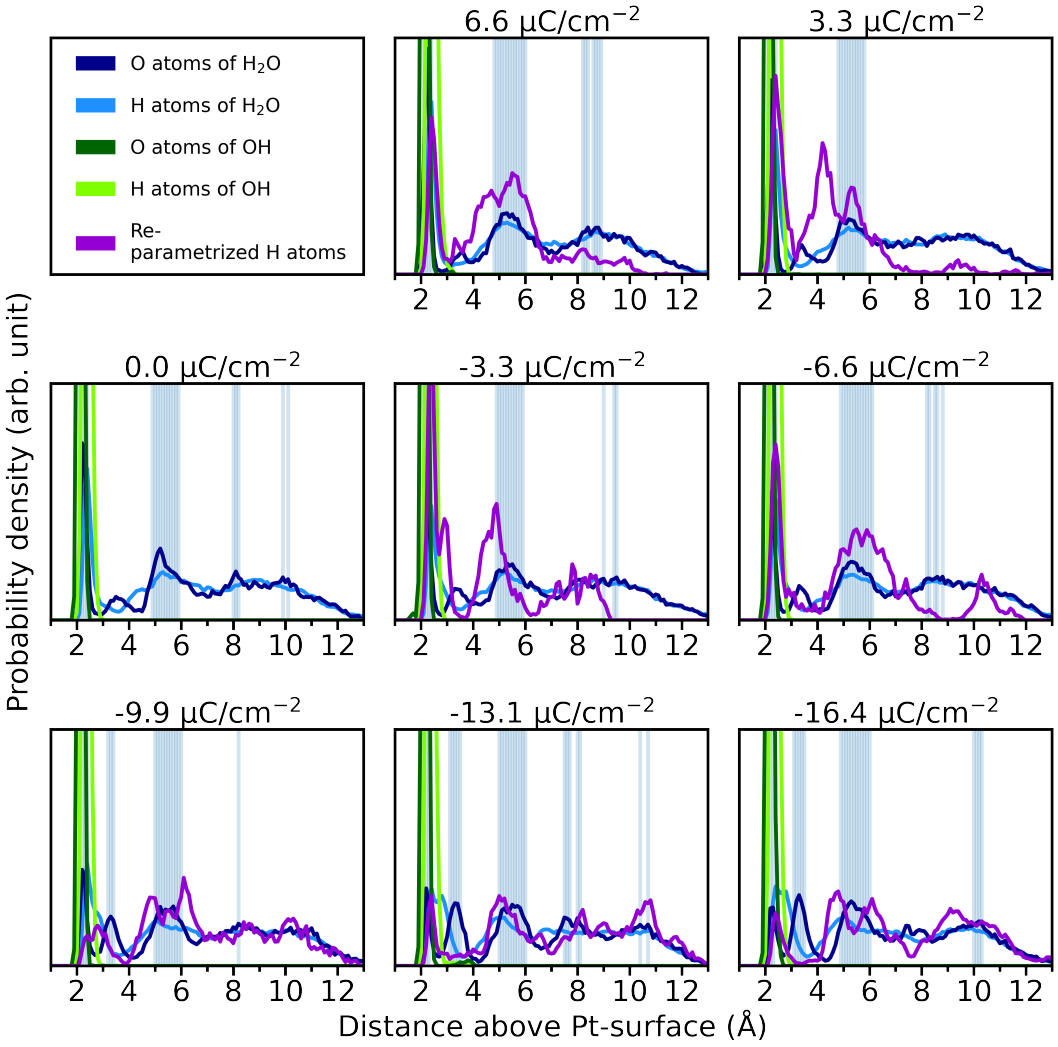

Figure 2.6: Same as Figure 2.2, but for Pt(111) + 24 H_2O + 5/12 ML OH*.

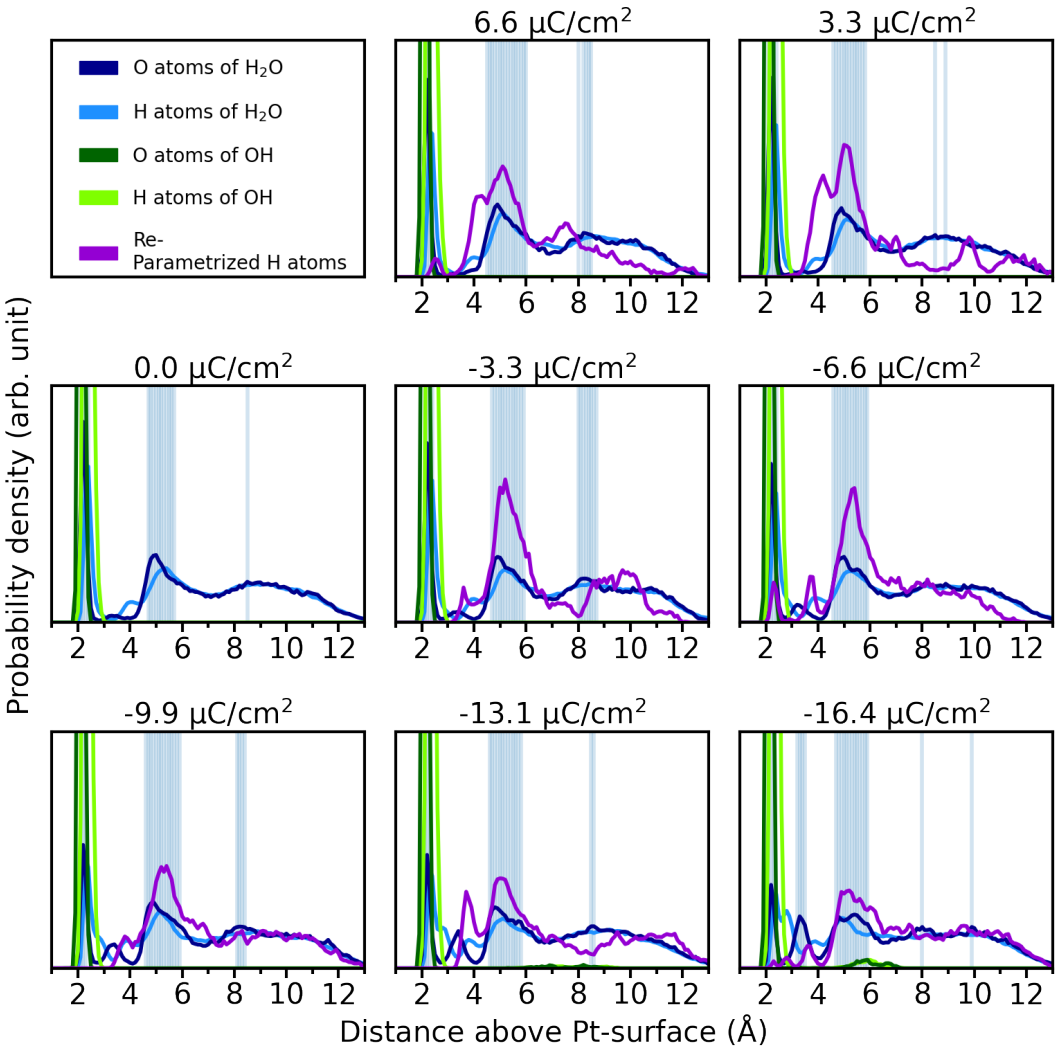

Figure 2.7: Same as Figure 2.2, but for Pt(111) + 24 H_2O + 5/12 ML OH* + O_2*.

Chapter 3

O_2 Adsorption

An integral part of this work is based upon understanding the O_2 adsorption on the two metal surfaces, Au(111) and Pt(111), from different computational methods. Therefore, this chapter is dedicated i) to explain how the O_2* adsorption energies are calculated, ii) to understand the O_2 adsorption and how we define it, and lastly iii) to cover the computational details required to obtain O_2 adsorption energies from AIMD.

3.1 Obtaining O_2* Adsorption Energies

To understand O_2 adsorption, it is essential to calculate the O_2* adsorption energy, which quantifies the energy released or required during the adsorption process and reflects the strength of the interaction between O_2 and the metal surfaces being studied. The general formula to calculate the electronic O_2* adsorption energy E_{ads} is shown in the following:

$$E_{\text{ads}} = E_{\text{O}_2^*} - E_* - E_{\text{O}_2(\text{g})} \tag{3.1}$$

where * is the energy of the clean slab, O_2* denotes the energy of the surface-bound O_2* configurations. Here, going to a more negative value of E_{ads} indicates a stronger binding to the metal surface in question. For all static calculations, Equation 3.1 was used, where the energies $E_{\text{O}_2^*}$ and E_* vary depending on the applied electric field $\vec{E}$ (saw-tooth potential model) or applied surface charge density σ (implicit solvation model). But looking at dynamic AIMD simulation results, this formula changes to:

$$E_{ads}^{(\text{AIMD})}(\sigma) = E_{\text{O}_2{}^*,\text{H}_2\text{O}}(\sigma) - E_{*,\text{H}_2\text{O}}(\sigma) - E_{\text{O}_2(\text{g})} \tag{3.2}$$

where explicit water is now included and the energies become dependent on surface charge density σ applied as described in Section 2.4.3. The only term that is still obtained from static DFT calculation is the energy of O_2 (g) in vacuum $E_{\text{O}_2(\text{g})}$. The other energies included are now AIMD averages. The reference energy $E_{*,\text{H}_2\text{O}}(\sigma)$ is defined as the AIMD average over all trajectories that include H_2O (+ OH^*) on a

metal surface, specifically in the absence of O_2. OH* is only present in simulations, where we specifically investigate the O_2 adsorption with surface coverage species on Pt(111).

$$E_{*,\mathrm{H_2O}}(\sigma) = \frac{1}{N}\sum_{k=1}^{N} E^{(k)} = \frac{1}{N}\sum_{k=1}^{N}\frac{1}{\tau_k}\sum_{i}^{\tau_k} E_i \tag{3.3}$$

The first sum runs over all N trajectories characterized by an (effective) surface charge density σ. The second summation includes all time steps τ_k of trajectory k, where E_i represents the total energy at a given timestep that AIMD gives as a DFT electronic energy.

The second AIMD average energy is calculated similarly, except that the trajectories now include adsorbed O_2* in addition to the metal slab and H_2O (+ OH*). Especially for the case of the weak binding Au(111), O_2 is not always adsorbed at the surface. We only include the subset of images where the O_2 is adsorbed at the surface into the average energy $E_{\mathrm{O_2{}^*,H_2O}}$. We will define the adsorbed O_2* in Section 3.5.

$$E_{\mathrm{O_2{}^*,H_2O}}(\sigma) = \frac{1}{N}\sum_{k=1}^{N} E^{(k)} = \frac{1}{N}\sum_{k=1}^{N}\frac{1}{\tau_k^{(ads)}}\sum_{i}^{\tau_k^{(ads)}} E_i \tag{3.4}$$

τ_k^{ads} only includes images, where adsorbed O_2* is present on the metal slab (see Section 3.5).

3.2 Error Analysis

3.2.1 Error Analysis of Trajectory

The error of each trajectory k is calculated to make sure that the average energy $E(k)$ is well sampled and converged. For simplicity, the superscript k will henceforth be dropped and the trajectory average energy will be denoted as $\bar{E}$. The error is shown in terms of standard deviation and variance as follows:

$$s^2(\bar{E}) = \frac{m}{\tau_k^{(\mathrm{ads})}} s^2(E) \qquad \text{where} \qquad s^2(E) = \frac{1}{\tau_k^{(\mathrm{ads})} - 1}\sum_{i=1}^{\tau_k^{(\mathrm{ads})}} (E_i - \bar{E})^2 \tag{3.5}$$

$$s(\bar{E}) = \sqrt{s^2(\bar{E})}\ . \tag{3.6}$$

One problem with molecular dynamics data is, that there might be statistical interdependencies that lead to a wrong average. In this work, the block averaging method was applied to calculate the scaling factor m as explained in detail in Reference [108]. Here, the trajectory is divided into n blocks b with lengths of L so that $\tau_k^{(\mathrm{ads})} = nL$.

For each block, the mean energy and the variance are calculated:

$$E_b = \frac{1}{L}\sum_{\tau \in b} E(\tau) \tag{3.7}$$

$$s^2(E_b) = \frac{1}{n-1}\sum_{b=1}^{n}(E_b - \bar{E})^2 \tag{3.8}$$

The relationship $(b-1)L + 1 \leq \tau \leq bL$ can be stated for each block b. In the next step, the sizes of the blocks are varied. For the Au(111) surface the sizes that were chosen are [2,4,6,8,12], where $L_i = \tau_k^{(\mathrm{ads})}/n_i$.

Now going to bigger block sizes, the block averages should become uncorrelated and the variance in the mean is defined as $s^2(\bar{E}) = s^2(E_b)/n = s^2(E_b) \cdot L/\tau_k^{(\mathrm{ads})}$. The scaling factor that can also be seen as the correlation time m describes the statistical inefficiencies due to correlated images. It can be calculated from:

$$m = \lim_{L\to\infty} m(L) \qquad \text{where} \qquad m(T) = L\frac{s^2(E_b)}{s^2(E)} \ . \tag{3.9}$$

The maximum $m(L_i)$ was taken as an estimate of m into Eqs. 3.5-3.6 since $m(L_i)$ is monotonously increasing with L_i. This way we made sure that each trajectory gives a well-converged average energy. We conduct the error analysis for each trajectory only for the Au(111) because of the poor statistics (as seen in Figure 3.4) stemming from the unfavorable binding of the O_2 to the metal surface. In contrast, on the strong binding Pt(111) we observe a very stable O_2* state leading to great convergence as seen in Figure 3.5 and 3.6.

3.2.2 Error Analysis of the Mean of Trajectories

The mean energy of the trajectory averages $E_{\mathrm{O_2{}^*,H_2O}}(\sigma)$ as shown in Equation 3.2 also gives an uncertainty, the standard deviation in the mean $s_{E_{\mathrm{O_2{}^*,H_2O}}}(\sigma)$:

$$s^2_{E_{\mathrm{O_2{}^*,H_2O}}}(\sigma) = \frac{1}{N}\frac{1}{N-1}\sum_{k=1}^{N}(E^{(k)}_{\mathrm{O_2{}^*,H_2O}}(\sigma) - E_{\mathrm{O_2{}^*,H_2O}}(\sigma))^2 \tag{3.10}$$

$$s_{E_{\mathrm{O_2{}^*,H_2O}}}(\sigma) = \sqrt{s^2_{E_{\mathrm{O_2{}^*,H_2O}}}(\sigma)} \tag{3.11}$$

N denotes the number of included trajectories. Analog to this, the standard deviation in the mean of the clean metal slabs $s_{E_{*,\mathrm{H_2O}}}(\sigma)$ can be calculated for $E_{*,\mathrm{H_2O}}(\sigma)$:

$$s^2_{E_{*,\mathrm{H_2O}}}(\sigma) = \frac{1}{N_*}\frac{1}{N_*-1}\sum_{k=1}^{N_*}(E^{(k)}_{*,\mathrm{H_2O}}(\sigma) - E_{*,\mathrm{H_2O}}(\sigma))^2 \tag{3.12}$$

$$s_{E_{*,\mathrm{H_2O}}}(\sigma) = \sqrt{s^2_{E_{*,\mathrm{H_2O}}}(\sigma)}\ . \tag{3.13}$$

With these two error definitions, we conduct error propagation to reach the final $s_{E^{(\mathrm{explicit})}_{\mathrm{ads}}}(\sigma)$ of $E^{(\mathrm{explicit})}_{\mathrm{ads}}(\sigma)$ as calculated in Equation 3.2. We will use these in Chapter 4 and 5 for Au(111) and Pt(111), respectively.

$$s_{E^{(\mathrm{explicit})}_{\mathrm{ads}}}(\sigma) = \sqrt{s^2_{E_{\mathrm{O_2{}^*,H_2O}}}(\sigma) + s^2_{E_{*,\mathrm{H_2O}}}(\sigma)} \tag{3.14}$$

3.3 O_2* Adsorption Energy: Corrections & Free Energy Contributions

Physical properties like electronic adsorption computed by DFT are always given at a temperature of 0 K. DFT does not include several energy contributions, such as the zero point energy (ZPE), entropic contributions, or enthalpy contributions, that need to be considered in realistic conditions. It is common practice in surface science applications to correct for these contributions as a post-processing step. For static calculations (vacuum DFT, saw-tooth, and implicit solvation calculations), we include the zero-point energy ($E_{\mathrm{ZPE,O_2{}^*}}$), the enthalpic energy ($C_{p,\mathrm{O_2{}^*}}T$) and lastly also entropy contributions ($-TS_{\mathrm{O_2{}^*}}$) to the electronic energy ($E_{\mathrm{O_2{}^*}}(\sigma)$). Furthermore, in addition to those contributions, an additional O_2 gas-phase correction ($E_{\mathrm{corr.}}$) is added to the DFT energy of gas-phase O_2 $E_{\mathrm{O2(g)}}$.

$$\begin{aligned} G^{(\mathrm{static})}_{\mathrm{ads}}(\sigma) = {} & E_{\mathrm{O_2{}^*}}(\sigma) + E_{\mathrm{ZPE,O_2{}^*}} + C_{p,\mathrm{O_2{}^*}}T - TS_{\mathrm{O_2{}^*}} \\ & - E_*(\sigma) - \left[(E_{\mathrm{O_2(g)}} + E_{\mathrm{corr.}}) + E_{\mathrm{ZPE,O_2(g)}} + C_{p,\mathrm{O_2(g)}}T - TS_{\mathrm{O_2(g)}}\right] \end{aligned} \tag{3.15}$$

The enthalpic contribution $C_{p,\mathrm{O_2{}^*}}T$ can be neglected when calculating the free energy from dynamic AIMD. The O_2* adsorption free energy from AIMD becomes:

$$\begin{aligned} G^{(\mathrm{AIMD})}_{\mathrm{ads}}(\sigma) = {} & E_{\mathrm{O_2{}^*,H_2O}}(\sigma) + E_{\mathrm{ZPE,O_2{}^*}} - TS_{\mathrm{O_2{}^*}} \\ & - E_{*,\mathrm{H_2O}}(\sigma) - [(E_{\mathrm{O_2(g)}} + E_{\mathrm{corr.}}) + E_{\mathrm{ZPE,O_2(g)}} + C_{p,\mathrm{O_2(g)}}T - TS_{\mathrm{O_2(g)}}] \end{aligned} \tag{3.16}$$

3.3.1 O_2 Gas-Phase Error Correction

It is known when using GGA-type functionals, that the ground state energy $E_{O_2(g)}$ of the triplet state of O_2 in gas-phase is particularly imprecise [58, 109]. We correct for the well-known oxygen over-binding predicted by semi-local DFT functionals [110] by assuming that all the error resides in the triplet O_2(g) ground state reference since it is unclear how much this error extends into the adsorbed O_2* state (after hybridization with the continuum of electronic states of the metal surface). We add a correction term $E_{\text{corr.}}$, derived from experimental and computational quantities. The free energy of the reaction shown in Equation (3.17) is known experimentally. Additionally, we estimate the free energy via vacuum DFT calculations:

$$O_2(g) + 2H_2(g) \longrightarrow 2H_2O(l) \tag{3.17}$$

In order to calculate the free energy of Equation (3.17) the ideal gas approximation as implemented in ASE is used [111, 112]. The free energy contributions of $E_{H_2O(l)}$ are calculated at room temperature at a pressure of 35 mbar, which is the H_2O vapor pressure [113]. The free energy of Equation (3.17) is given by:

$$\begin{aligned} \Delta G_{\text{DFT}} = E_{H_2O(l)} + E_{\text{ZPE},H_2O} - TS_{H_2O} \\ -(E_{O_2(g)} + E_{\text{ZPE},O_2} - TS_{O_2}) \\ -(E_{H_2(g)} + E_{\text{ZPE},H_2} - TS_{H_2}) \end{aligned} \tag{3.18}$$

From vacuum DFT, $\Delta G_{\text{DFT}} = -4.24$ eV is calculated. This value can be compared with the experimental value $\Delta G_{\text{exp.}}$=-4.916 eV [114]. The error is obtained by the difference of those two values leading to a post-processing correction of $E_{\text{corr.}} =$ 0.68 eV for the employed gas-phase O_2 reference correcting for the overbinding O_2(g).

3.3.2 Zero Point Energy, Entropy and Enthalpic Contributions

All following computations were facilitated by tools provided in the ASE [111, 112]. The starting point is DFT geometry optimized structures of either the O_2* adsorbed on a metal slab in vacuum or the gas-phase molecule in question in vacuum (see Section 2.3.1). The corrections were calculated at PZC and were maintained consistently during modifications of the surface charge.

For all cases, the vibrational modes were calculated from a finite difference approximation of the Hessian matrix as implemented in ASE [111, 112, 115].

In order to calculate the zero-point energy (E_{ZPE}), entropy (TS), and enthalpic contributions (C_pT) two approximations are further made dependent on if the structure in question includes an adsorbed or a gas-phase species.

For the adsorbed O_2* state, the harmonic oscillator is used; all degrees of freedom are treated harmonically. The metal slab was considered frozen so that the contributions were calculated only for the adsorbed O_2*. We also use the values computed on the clean Pt(111) slab for our simulations with the pre-covered Pt(111) + 5/12 monolayer (ML) OH* slab.

For the gas phase calculations (O_2 (g), H_2(g), H_2O(g)) the ideal gas approximation was applied.

The resulting free energy corrections are listed in Table 3.1.

	E_{ZPE} (eV)	TS (eV)	C_pT (eV)
O_2* on Au(111)	0.10	0.12	0.10
O_2* on Pt(111)	0.13	0.14	0.07
O_2(g)	0.10	0.65	0.09
H_2(g)	0.27	0.41	0.09
H_2O(g)	0.57	0.68	0.10

Table 3.1: Zero point energy, entropy, and enthalpic contributions at $T = 300$ K.

3.4 Definition of O_2 Adsorption

When calculating AIMD simulations, we obtain trajectories where the molecular oxygen can be either bound to the surface or solved in the water layers. It's important to differentiate between these different O_2 states, which requires understanding of the electronic structure of O_2. Using molecular orbital theory, we can construct a molecular orbital energy level diagram as seen in Figure 3.1. Each oxygen atom contributes 6 electrons from its atomic orbitals (AOs), which then fill the shared molecular orbitals (MOs). Following Hund's rule, the MOs are filled with the available electrons, resulting in two unpaired electrons in the two anti-bonding $\pi^*_{2\mathrm{p_x}}$ and $\pi^*_{2\mathrm{p_y}}$ orbitals. This causes the oxygen molecule to exhibit paramagnetic behavior, with the unbound oxygen molecule showing a spin state of 2 μ_B [116].

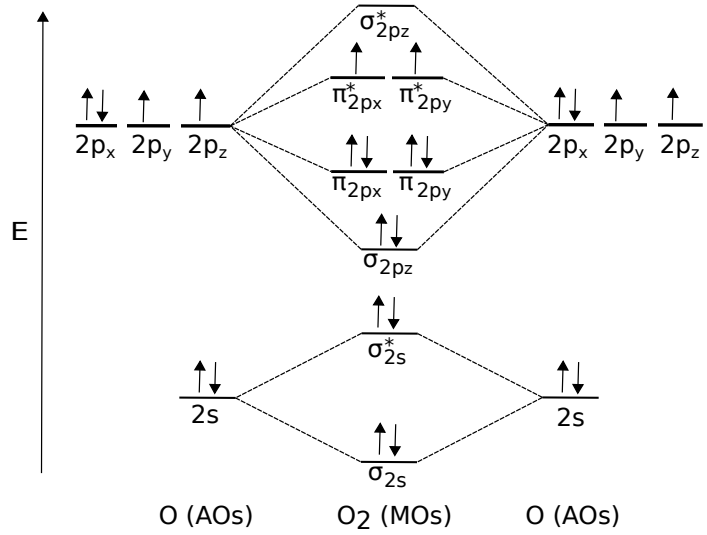

Figure 3.1: Molecular orbital energy level diagram for O_2. It shows how the 12 valence electrons (6 from each atom) are distributed in the molecular orbitals. The orbitals are filled following Hund's rule. Adapted from [116].

When the O_2 approaches the metal surface, there are several modes of the O_2 adsorption. The physisorbed O_2, where the oxygen is weakly bound to the surface via Van der Waals forces. The oxygen binds through the s- and p-orbitals leading to a possible vertical orientation [39]. The second mode is the chemisorbed O_2*, which is a more defined state where the O_2* binds much stronger to the surface. Here, one can mostly find the O_2* lying parallel to the surface. The main difference to the physisorbed O_2 is that charge from the metal surface transfers into the O_2*, filling up the anti-bonding states which leads to an activated O_2* for further reaction. Lastly, one can also observe dissociation in some cases which is often thermodynamically favored [39]. Figure 3.2 shows a schematic description of these possible O_2 states.

Looking more in-depth into the possible O_2 states, two distinct states can be further distinguished: the superoxo state O_2^- and the peroxo state O_2^{2-}, whereas the integer charges are presented for a gas-phase species. When looking at adsorbed species, it is difficult to quantify the charge transfer, but depending on the O_2* state, the O_2* displays different properties as listed in Table 3.2. These can furthermore be used as descriptors to distinguish the superoxo from the peroxo state. When the anti-bonding states of the O_2* get filled with charge from the metal surface during adsorption, the intramolecular O-O* distance gets lengthened. Additionally, spin quenching can be observed; the magnetic moment goes down towards 0 μ_B. The superoxo species is defined as a species with an intramolecular O-O* distance of around 1.35 Å [117] and a magnetic moment between 0-1 μ_B. Going to the peroxo state, by definition, the anti-bonding orbitals are filled which leads to an intramolecular O-O* distance

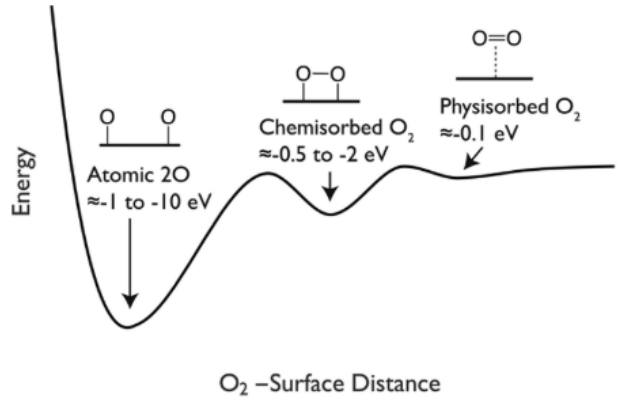

Figure 3.2: Schematic representation of the O_2* adsorption states. Reprinted with permission from Montemore *et al.* [39] Copyright 2024 American Chemical Society.

of 1.48 Å and a magnetic moment of 0 μ_B [39, 118]. Henceforth, "O_2*" will include both the superoxo O_2^- and peroxo O_2^{2-} species.

Species	Magnetic moment (μ_B)	O-O distance (Å)
O_2	2	1.207 [119]
Superoxo O_2*	0-2	1.35 [117]
Peroxo O_2*	0	1.48 [118]

Table 3.2: Possible O_2 states are shown with their respective magnetic moment and intramolecular O-O distance [39].

3.5 O_2 Adsorption Descriptors

In the previous section, we have set the groundwork that enables us to define a set of adsorption descriptors that can be used to filter AIMD trajectories so that we only include images with adsorbed O_2* into our O_2* adsorption energy calculations.

An AIMD image is regarded as adsorbed if the O_2 molecule (i) is sufficiently close to the surface with its center-of-mass height above metal surface (COM_z) < 3 Å, (ii) has a magnetic moment $\mu < 1$ μ_B, (iii) is not spontaneously protonated (the closest distance from the oxygen to any hydrogen > 1.3 Å) and iv) is not spontaneously dissociated (the intramolecular bond length < 1.6 Å).

For the Au(111), the choice of adsorption descriptor is sensitive to the magnetic moment and COM_z, since only a very small subset of the images include adsorbed O_2*, the O_2 mostly prefers to move dynamically at the interface. Lastly, protonation starts playing a role in the trajectories at reducing conditions [1]. Therefore, we

present sensitivity analyses for Au(111) in Fig. 3.3 focusing on the O_2* adsorption free energy in relation to the descriptor cut-off values that determine O_2* adsorption status: COM_z in Figure 3.3a), and magnetic moment cut-off in Figure 3.3b). Generally, the results show limited sensitivity to the chosen cut-off values, except for very low magnetic moment μ cut-offs (below 1 μ_B). This can be explained by the weak binding nature of Au(111), particularly near the PZC, which results in a preference to bind weakly, with little charge transfer and therefore, a relatively high magnetic moment μ value of the O_2*. Consequently, selecting a low cut-off, such as 0.5, leads to inadequate sampling. Under highly reducing conditions, numerous images exhibit almost entirely quenched spin (i.e., $\mu \approx 0$ μ_B), making the results less sensitive to the magnetic moment cut-off choice.

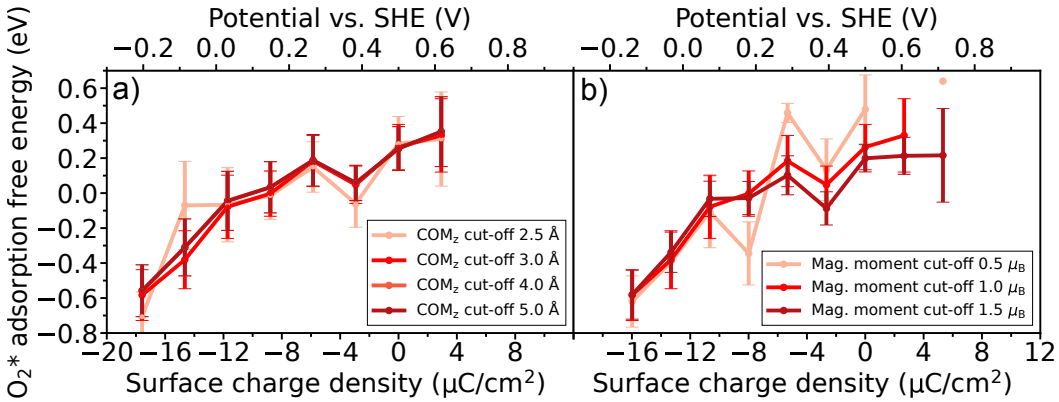

Figure 3.3: The O_2* adsorption free energy is plotted against the surface charge density. Panel a) shows the O_2* adsorption free energy variation when using different COM_z cut-off values with a fixed magnetic cut-off (μ = 1 μ_B). Panel b) focuses on the O_2* adsorption free energy variation with changing magnetic moment cut-off values while using a constant COM_z cut-off (COM_z = 3.0 Å).

When looking at the strong binding Pt(111), the O_2* adsorption is favorable and we find that O_2* is never desorbing, making it very insensitive to the choice of adsorption descriptor. Only the intramolecular bond length O-O* descriptor plays a major role since we observe many instances of dissociation. We choose all images where the O-O* bond length is smaller than 1.6 Å as a descriptor to make sure we do not include the O_2* dissociation process.

3.6 O_2* Adsorption Free Energies from AIMD

3.6.1 AIMD Sampling

Building upon the technical details described, we can now extract the O_2* adsorption energy from the AIMD simulations (for technical details, see Section 2.3.2 and 2.4.3).

The results from the AIMD simulations are listed in Tables 3.3–3.5: For each surface charge density σ, the O_2* adsorption free energy $G_{\text{ads}}^{(\text{AIMD})}$ is shown with the respective standard deviation in the mean (see Section 3.2.1). The number of included-to-original trajectories with O_2* is shown, indicating the number of trajectories that were utilized to calculate G_{ads} vs. the total number of trajectories that were calculated. The last column lists the number of reference trajectories without O_2*.

σ (µC/cm^2)	G_{ads} (eV)	included-to-original trajs. with O_2	included-to-original trajs. without O_2
2.9	0.42±0.21	5/11	10/11
0.0	0.35±0.13	7/11	11/11
-2.9	0.14±0.11	5/11	11/11
-5.9	0.27±0.15	4/11	8/11
-8.8	0.09±0.13	6/11	11/11
-11.7	0.01±0.18	6/11	11/11
-14.6	-0.29±0.17	3/11	7/11
-17.6	-0.49±0.15	3/11	8/11

Table 3.3: Summary of AIMD data for Au(111): Average values and errors for the O_2 adsorption free energies for each value of surface charge density σ. The last two columns show how many computed trajectories were included in the adsorption free energy with and without O_2, respectively.

The final O_2* adsorption free energy values along with the number of included trajectories for Au(111) are shown in Table 3.3. Many trajectories were discarded either due to the fact that they did not give any images including adsorbed O_2* or the desired energy accuracy was not met ($s_{E^{(k)}} < 0.1$ eV) (due to an insufficient number of images with adsorbed O_2*). This can be explained by the weak binding nature of Au(111). Going to reducing conditions, some trajectories displayed spontaneous O_2 protonation and had to be discarded.

The data used to obtain the O_2* adsorption free energy for Pt(111) and the OH*-covered Pt(111) is shown in Table 3.4 and 3.5, respectively. Some trajectories were excluded due to O_2* dissociation during the equilibration phase. Additionally, we observed a simulation artifact where the upper Pt(111) layer shifted non-physically in the xy-plane, consistent with observations reported by Heenen *et al.* [82].

This artifact was most prevalent in trajectories involving Pt(111) with 5/12 ML OH*

σ ($\mu C/cm^2$)	G_{ads} (eV)	included-to-original trajs.	included-to-original trajs. without O_2
6.6	-0.94±0.09	14/16	15/16
3.3	-0.71±0.08	14/16	16/16
0.0	-0.86±0.08	13/16	16/16
-3.3	-0.76±0.08	14/16	15/16
-6.6	-0.84±0.07	14/16	15/16
-9.9	-0.99±0.08	14/16	15/16
-13.1	-0.79±0.08	15/16	14/16
-16.4	-0.88±0.05	13/16	15/16

Table 3.4: Summary of AIMD data for Pt(111): Average values & errors for the O_2 adsorption free energies corresponding to each value of surface charge density σ. The last two columns note how many computed trajectories were included in the adsorption free energy with O_2 and without O_2, respectively.

without O_2*. All trajectories exhibiting this artifact were discarded, which accounts for the larger errors in the O_2* adsorption energy in Table 3.5 as compared to Table 3.4.

σ ($\mu C/cm^2$)	G_{ads} (eV)	included-to-original trajs. with O_2	included-to-original trajs. without O_2
6.6	-0.91±0.15	16/16	12/16
3.3	-0.85±0.12	15/16	11/16
0.0	-0.92±0.14	16/16	9/16
-3.3	-1.09±0.16	16/16	11/16
-6.6	-1.08±0.10	16/16	9/16
-9.9	-1.11±0.06	14/16	8/16
-13.1	-0.81±0.10	14/16	7/16
-16.4	-0.93±0.12	15/16	13/16

Table 3.5: Same as Table 3.4, but for Pt(111) + 5/12 ML OH*.

3.6.2 Trajectory Convergence

For each total surface charge considered, multiple trajectories were run both with and without O_2 to obtain a representative picture of the various local minimum water structures as summarized in the previous section. New trajectories were generally initialized by using images from already conducted AIMD simulations after equilibration time. The atomic momenta are then re-initialized according to the Maxwell-Boltzmann distribution, leading to differing behavior. Images representing chemisorbed O_2 were identified using several adsorption descriptors, as detailed in Section 3.5. Further explanation regarding calculating the O_2* adsorption energy

can be found in Section 3.1. Now that we obtained multiple trajectories, we also use uncertainty analysis to define the errors as explained in Section 3.2 or in literature (see Ref. [108]).

Achieving fully converged structures and proper thermodynamic averages requires sampling times that exceed the current capabilities of AIMD, especially when looking at the electrochemical double layer that contains slowly equilibrating components [120, 121]. For the weakly interacting Au(111) surface, simulations were extended to 40 ps (including equilibration) to ensure adequate statistical sampling of the chemisorbed O_2* state consistent with previous studies [82, 122, 123]. In contrast, for the strongly interacting Pt(111) surface, where O_2* predominantly remains adsorbed, a simulation duration of 12 ps per trajectory (including equilibration) was sufficient to achieve total energy convergence with a standard deviation below 0.01 eV (referred to running averages in Figures 3.5 and 3.6).

On Au(111), the AIMD simulations with O_2 showed unrealistic magnetic moments and extended convergence times at first. We found that the default values for the linear mixing factor for the magnetization density A and the cut-off wavevector for the Kerker mixing scheme k_0^2 (as explained in Section 2.3.1) lead to these instabilities. After conducting stability tests giving us stable parameters, a subset of images, including adsorbed O_2* from each AIMD trajectory, was re-calculated and re-filtered. To create a representative subset of the trajectory, a specific number of images distributed evenly across the entire trajectory was selected. This approach ensures that the subset captures the diversity and variability of the original trajectory. For each subset of re-calculated and re-filtered images, we calculate the average energy $E^{(k)}$ and the standard deviation in the mean $s_{E^{(k)}}$ (calculated as described in Section 3.1 and 3.2.1, respectively). Once $s_{E^{(k)}} < 0.1$ eV, the re-calculation was stopped and the mean trajectory energy $E^{(k)}$ was used to calculate the adsorption free energy as described in Section 3. Otherwise, more images were re-calculated and re-filtered until the required accuracy was reached. Once there were no more adsorbed O_2* images that could be taken from the AIMD simulation, which was the case for many trajectories due to the weak binding nature of Au(111), the trajectory was discarded. We plot the average energy $E^{(k)}$ and the standard deviation in the mean $s_{E^{(k)}}$ vs. the number of images considered in the average in Figure 3.4. Each line represents a different trajectory and we can see how most trajectories give a well-converged average energy $E^{(k)}$. The legends show the standard deviation in the mean (eV) for the rightmost point of each trajectory line. For surface charge density 5.9 µC/cm^2, we barely see any adsorbed O_2* images, and the trajectory is not converged, we therefore neglect this surface charge density and discard its trajectory. The average energies $E^{(k)}$ of the trajectories still vary up to 1.5 eV, demonstrating the importance

of sampling from multiple starting water structures.

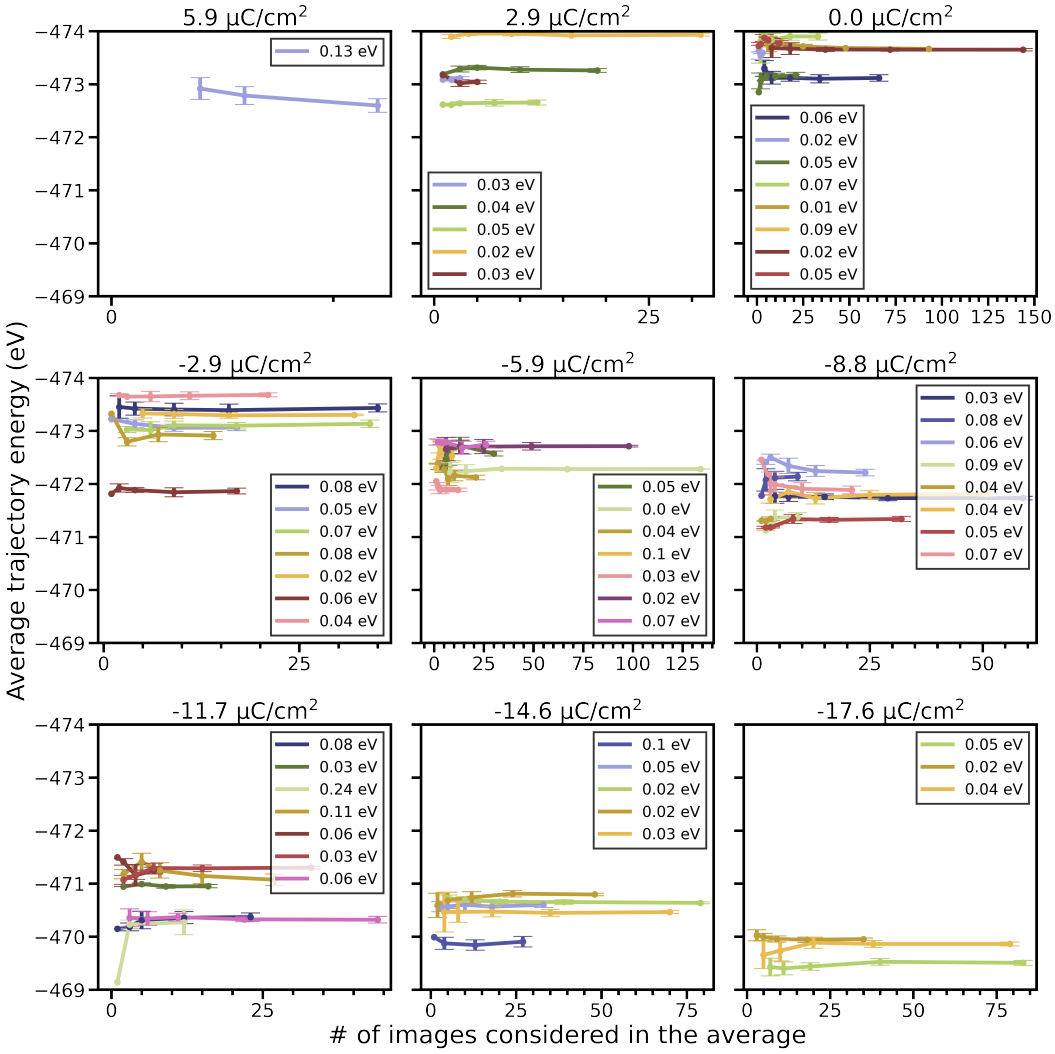

Figure 3.4: The average trajectory energy ($E^{(k)}$ in Equation (3.4)) is plotted against the count of images identified as adsorbed and included in the average for Au(111). The colored lines represent distinct trajectories, with legends indicating each trajectory's associated final standard deviation. Each panel illustrates a different (effective) surface charge density, as specified at the top.

Going to strong binding Pt(111), we change our approach: We conduct stability tests for linear mixing factor for the magnetization density A and the cut-off wavevector for the Kerker mixing scheme k_0^2 (as explained in Section 2.3.1) beforehand. Therefore, re-calculation of the images was not required. Additionally, we find O_2* adsorption favored independent of the potential. Every trajectory gives well-converged mean energies $E^{(k)}$, leading to a standard deviation less than 0.1 eV. We plot the running average trajectory energy $E^{(k)}$ vs. the timestep in Figure 3.5 for the clean Pt(111)

with O_2* and in Figure 3.6 for the OH*-covered Pt(111) with O_2*. Equilibration time is not included, which is why the count starts after 5000 fs and images without adsorbed O_2* (as defined in Section 3.5) are excluded. Every trajectory gives well-converged mean energies that can still vary up to 1.0 eV among different trajectories, thus, again, demonstrating the importance of sampling from multiple starting water structures.

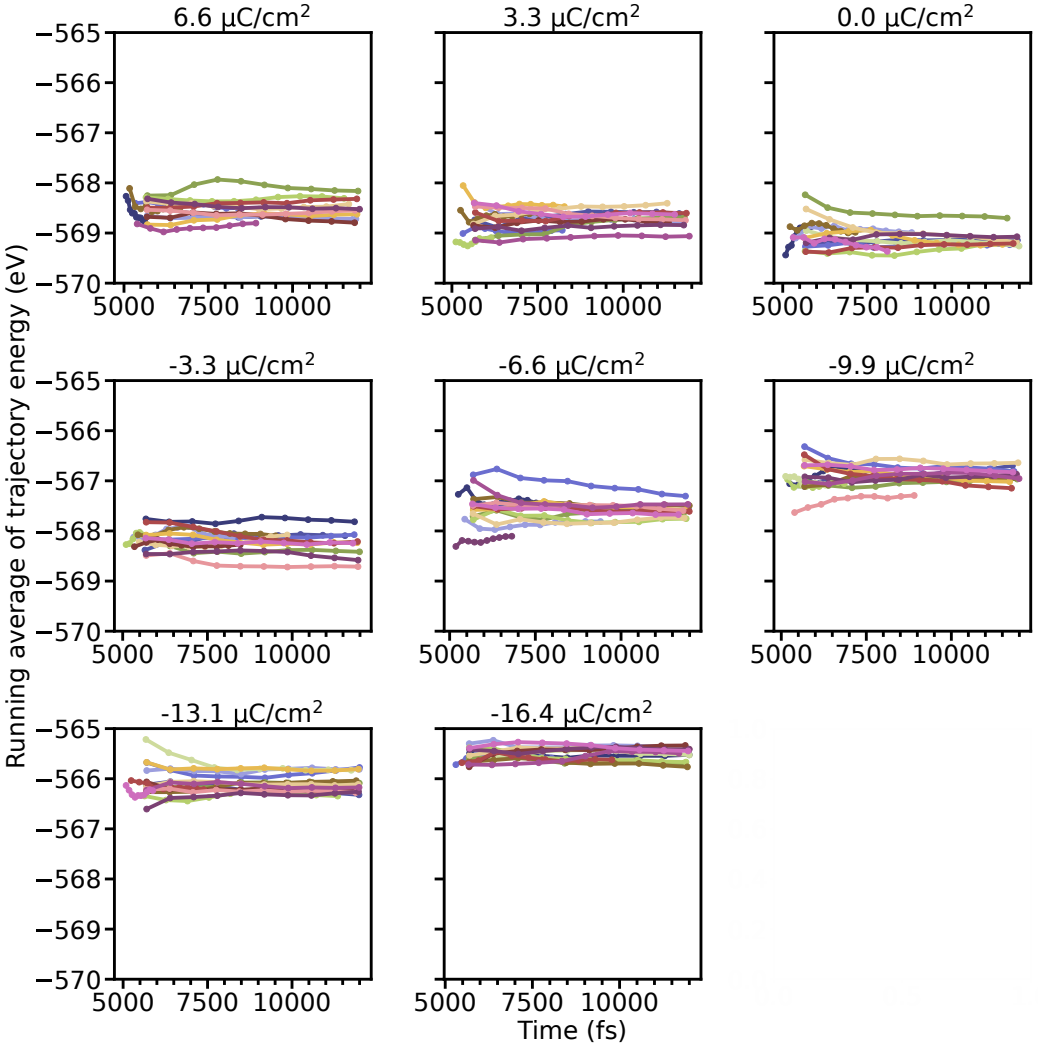

Figure 3.5: The average trajectory energy ($E^{(k)}$ in Equation (3.4)) is plotted against the timestep for Pt(111). The colored lines represent distinct trajectories. Each panel illustrates a different (effective) surface charge density, as specified at the top.

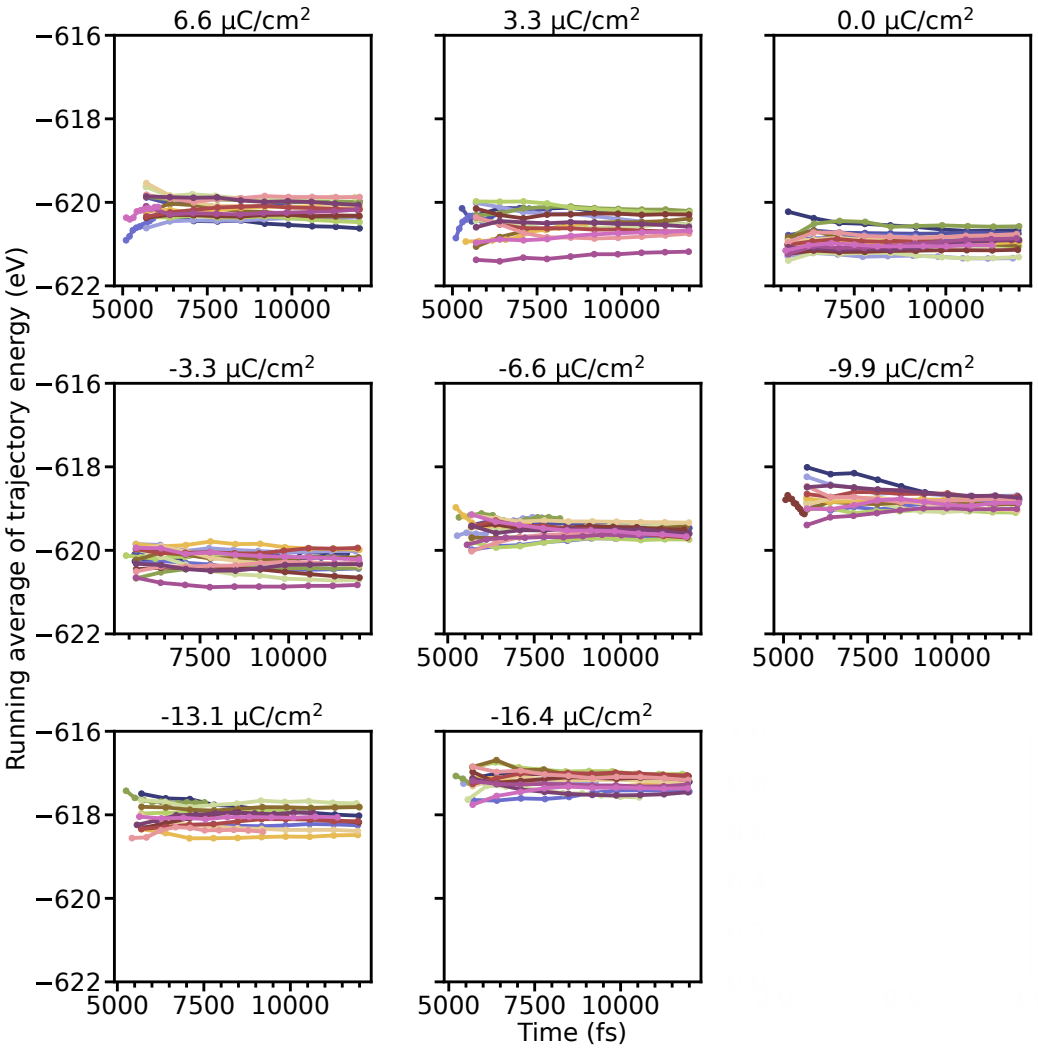

Figure 3.6: Same as Figure 3.5 but including 5/12 ML OH*.

Chapter 4

O_2 Adsorption on the Weak Binding Au(111)

4.1 Introduction

The Au(111) surface is a great benchmark system when investigating ORR on weak binding metal catalysts since it shows a rather high activity in comparison to other weak binding metal catalyst surfaces [124–129]. Furthermore, it is stable under acidic and alkaline conditions [13]. The ORR reaction mechanism is commonly shown in Figure 4.1 as a step-wise reduction through PCET steps: At each step, a proton and an electron are added. Two reaction mechanisms are often shown when looking at weak binding metal catalyst surfaces: the associative four-electron pathway leading to H_2O or the peroxyl two-electron pathway leading to H_2O_2 (as explained in Section 1.2.1). Dissociation of the O_2* is neglected because of the linear dependence of the oxygen binding energy and the barrier for oxygen dissociation [130], which would be rather high on the weak binding Au(111) surface. During the four-electron pathway, O_2 is getting step-wise reduced to OOH*, O*,OH* and finally to H_2O, while for the two-electron pathway, OOH* does not dissociate but gets further reduced to the final product H_2O_2. From experimental results, it is clear that the peroxyl reaction path dominates since H_2O_2 is the main product on Au(111) [126, 131].

Figure 4.1 depicts two such possible reaction mechanisms, where CHE (as described in Section 1.2.3) is used to include the effects of applied potential as a post-processing step [24]. The DFT-calculated free energies are calculated at point of zero charge (PZC). Each arrow depicts the contribution of the potential eU_{RHE} and an addition of a $(H^+ + e^-)$-pair. While being a rather elegant framework to account for the potential, it cannot capture potential effects on steps that are decoupled from proton transfers, i.e. non-PCET steps. This is the reason, why the O_2* adsorption was often neglected in previous work. Without O_2* adsorption, all reaction steps are downhill at $U_{\mathrm{RHE}} = 0$ V and remain so, up until a potential of 0.63 V. Going to higher potentials, the reaction starts to become thermodynamically unfavorable, starting with the formation of OOH*, which is, therefore, often considered the rate-

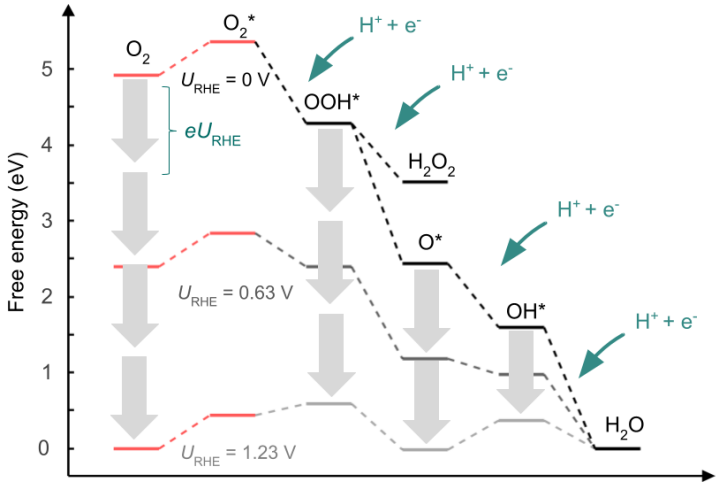

Figure 4.1: Energy pathway calculated from vacuum DFT including free energy contributions as explained in Section 3.3. CHE is applied to show the reaction mechanism under potential [24]. $U_{\mathrm{RHE}} = 0.63$ V is the highest potential where the reaction is thermodynamically favorable and $U_{\mathrm{RHE}} = 1.23$ V is the equilibrium potential.

determining step (RDS). However, despite extensive research, the identity of the RDS remains unclear.

In this charge-neutral framework consisting of the addition of PCET steps, how the ORR is often viewed, the adsorption of O_2* is often neglected as a purely "chemical" step independent from potential since it does not include a proton transfer. However, it remains unclear how the molecular oxygen even binds to such a weak binding metal catalyst surface. A simple vacuum DFT calculation on RPBE level gives an O_2* adsorption free energy of 0.31 eV showing that O_2 adsorption is not favored, as depicted in Figure 4.1. To our knowledge, O_2 has only been detected in a physisorbed state on Au under ultra-high-vacuum conditions (Montemore *et al.*, 2018 [39]), leaving its behavior in electrochemical environments under reaction conditions uncertain. These issues underscore the significance of investigating capacitive charging in realistic water environments.

Now let's take a look at the experimental results of the ORR on Au(111) as shown in Figure 4.2. Experimental rotating disk electrode (RDE) polarization curves depict the current density j_{tot} (indicating activity) when applying a potential to start an electrochemical reaction. For Au(111), the results show unusual behavior: The activity (described by the total current j_{tot}) shows pH-dependent behavior on U_{RHE} scale. The reaction shows much better activity in alkaline vs. acidic conditions. The pH dependency of the experimental onset on the U_{RHE} scale cannot be explained with a PCET step as the RDS. As explained in Section 1.2.3, U_{RHE} includes the

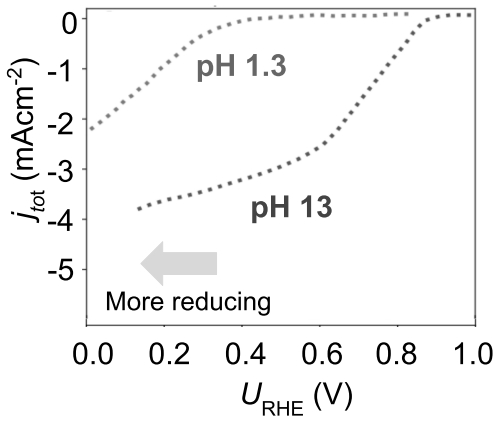

Figure 4.2: Experimental RDE polarization curves adapted with permission from Kelly *et al.* [91]. Copyright 2024 American Chemical Society. Recovered data from Ref. [131] (basic) and [126] (acidic).

activity stemming from electrons and protons, so seeing a pH dependence on the U_{RHE} scale means, that the reaction is determined by a step, where we likely find a proton decoupled electron transfer. To view the step $\mathsf{O_2} + (\mathsf{H^+} + \mathsf{e^-}) \longrightarrow \mathsf{OOH^*}$ as the RDS cannot explain the experimental behavior, calling for in-depth investigation of the O_2 adsorption.

Previous literature tries to elucidate the pH dependence of the activity: Ignaczak *et al.* proposed that the enhanced reaction rate in basic media is attributed to the formation of a stable superoxide ion following an initial outer-sphere electron transfer [132]. Similarly, Lu *et al.* suggested that surface-adsorbed H_2O functions as a proton donor, thereby facilitating the oxygen reduction reaction (ORR) in alkaline conditions [133]. Conversely, Vassilev *et al.* [134], Duan *et al.* [135], and Kelly *et al.* [91] emphasized the crucial role of adsorbed OOH* stabilization, attributed to local field effects at the electrified metal/water interface.

In this study, we investigate O_2 adsorption as the initial step of the ORR on Au(111). Moving beyond the PZC/CHE methodology, we present findings from three progressively sophisticated models of the electric double layer: a vacuum background with applied saw-tooth potential (see Section 2.4.1), implicit solvent model (see Section 2.4.2), and an explicitly modeled aqueous solvent using *ab initio* molecular dynamics (AIMD) (see Section 2.2 and 2.4.3). By systematically refining the electrochemical interface description, we elucidate field effects of varying physical origins. All models consistently describe dipole-field interactions and predict significantly enhanced O_2 binding at potentials relevant to ORR operation. However, only the atomically resolved solvent model provided by AIMD accurately captures the additional contribution from explicit hydrogen-bonding interactions, indicative of a peroxo surface

species formation at the ORR onset. Additionally, we find that the peroxo O_2* state is a precursor for the OOH* formation that we observe at reducing conditions close to ORR onset potential in our AIMD simulations. Overall, our results highlight the necessity of incorporating local electric field effects into electrochemical interface models and imply that the O_2 adsorption could be the rate-determining step.

4.2 O_2 Adsorption at the Electrified Interface from Static Calculations

In this work, we model the adsorption of O_2 at the electrochemical Au(111) interface trying to approximate the electrical double layer. In the first step, we use the crudest approximation, the aqueous solvent is completely neglected, and a saw-tooth potential is applied across the metal/vacuum interface to simulate the local potential drop driving the oxygen reduction reaction (ORR). Detailed descriptions of the methods and technical specifics are provided in Section 2.4.1. The O_2 adsorbate is relaxed at each applied electric field $\vec{E}$. The O_2* adsorption energy is then predicted at each electric field as explained in greater detail in Section 3.1:

$$E_{\text{ads}}(\vec{E}) = E_{\text{O}_2^*}(\vec{E}) - E_*(\vec{E}) - E_{\text{O}_2(\text{g})} \tag{4.1}$$

In this context, * and O_2* represent the clean surface and the surface-bound O_2* configurations, respectively. According to this definition, more negative E_{ads} values indicate stronger binding to the electrode. By correcting for the well-known overbinding of gaseous O_2(g) predicted by semi-local DFT and incorporating free energy contributions into Equation (4.1) (as detailed in Section 3.3), we obtain the free energy of O_2 adsorption, $G_{\text{ads}}(\vec{E})$, as a function of the local electric field [110].

Since we want to draw a comparison to higher level modeling methods, we can also show the O_2* adsorption free energy in terms of capacitive charging through an (effective) surface charge density σ or (absolute) electrode potential U_{SHE}. The assumption is made that the double layer behaves like a simple parallel-plate capacitor. This can be achieved with the help of Equation (2.42) which is described in detail in Section 2.4. While this approach incorporates several approximations that should be acknowledged, it enables us to establish a direct relationship with experimental potential conditions and allows for comparison with various theoretical models of the double layer. Consequently, the results of G_{ads} as a function of σ (bottom x-axis) and U_{SHE} (top x-axis) are presented in Figure 4.3 for a potential window that is realistic to the ORR, ranging from approximately -0.3 V to +1.0 V vs. SHE.

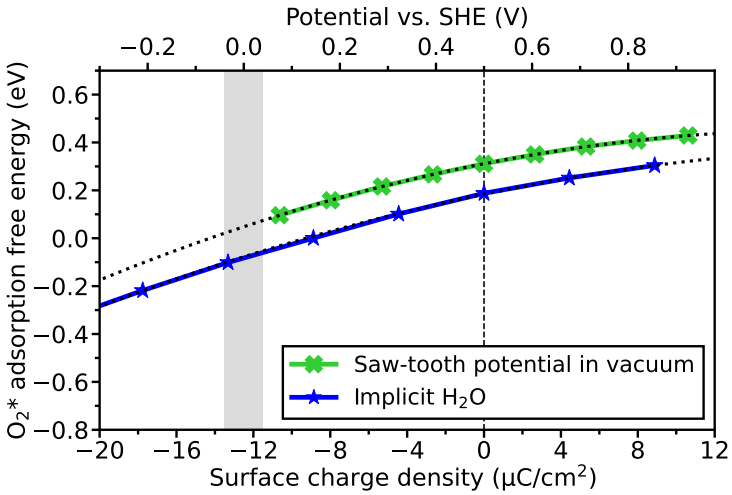

Figure 4.3: The free energy of O_2* adsorption at Au(111) is plotted as a function of surface charge density (bottom x-axis) and applied potential vs. SHE (top x-axis). The Figure compares different static models of the electrical double layer, as indicated in the legend: a vacuum background with applied saw-tooth potential (green crosses) and implicit solvation model (blue stars). The dotted black line shows a fitted second-order polynomial as seen in Equation (4.2). The vertical dashed line and the shaded gray area denote the PZC and the (approximate) experimental onset of the ORR, respectively.

Now, let's take a look at the saw-tooth potential in vacuum results, which can be seen as the green crossed curve in Figure 4.3: In the absence of an electric field, i.e., under conditions equivalent to the PZC ($\vec{E} = 0$, $\sigma = 0$, $U_{\mathrm{SHE}} = U_{\mathrm{PZC}}$), Figure 4.3 shows endothermic O_2 adsorption with $G_{\mathrm{ads}} = +0.30$ eV in vacuum. We focus exclusively on the lowest-energy chemisorbed state where the magnetic moment is fully quenched ($\mu = 0$), which leads to a peroxo O_2* (see Section 3.4). O_2* is significantly stabilized under electric fields corresponding to more reducing conditions. Within the present double-layer model, this stabilization is attributed to a purely electrostatic interaction. The strength of this interaction can be quantified using a dipole-field model, fitting to a (truncated) second-order polynomial [91]:

$$G_{\mathrm{ads}}(\vec{E}) = G_{\mathrm{ads}}^{\mathrm{PZC}} + \vec{p}\,\vec{E} - \frac{\alpha}{2}\,\vec{E}^2 \tag{4.2}$$

This relationship is shown as dotted black lines in Figure 4.3 where Equation (4.2) is fitted to the O_2* adsorption free energy of the saw-tooth potential in vacuum. Our analysis yields $p_z = 0.21\ e \cdot \text{Å}$ and $\alpha_{zz} = 0.15\ e \cdot \text{Å}^2/\text{V}$ for the z-components of the O_2* intrinsic dipole moment and polarizability, respectively. These values can be seen in Table 4.1 and they are in good agreement with literature [91].

	p_z ($e \cdot$ Å)	α_{zz} (e·Å^2/V)
Saw-tooth potential in vacuum	0.21	0.15
Implicit H_2O	0.22	0.12
Saw-tooth potential in vacuum from Ref. [91]	0.24	0.13

Table 4.1: Dipole moment p_z and polarizability α_{zz} components along the surface normal as extracted from the O_2* adsorption energy vs. the electric field on Au(111) (following Equation 4.2). The last row compares to the result from Kelly *et al.* [91].

Consequently, at the more negative potentials shown in Figure 4.3, O_2 chemisorption is favored by approximately 0.7 eV compared to the PZC, making it overall exothermic ($G_{ads} < 0$). This indicates that even this basic model of the electrical double layer captures a critical dependence on the absolute potential, suggesting that O_2 adsorption is an initial electrochemical step in the mechanism rather than a purely chemical one.

In the second step, the model is further refined to include solvation at the level of implicit H_2O electrolyte. Interestingly, this does not add much to the above picture, the fundamental conclusions still remain the same as drawn from the vacuum simulations. Here, the interface is explicitly charged while maintaining overall charge neutrality by distributing the corresponding counter-charge according to a Poisson-Boltzmann distribution within a polarizable continuum that represents the solvent [121, 136, 137]. Further information on the method can be found in Section 2.4.2. This method allows for the calculation of the O_2* adsorption energy, E_{ads}, and consequently the free energy of adsorption, G_{ads}, as direct functions of the excess surface charge density, σ. The free energy contributions are added following the same principles as for the saw-tooth calculations in vacuum (see Section 3.3). Figure 4.3 illustrates that, under these conditions, the implicit solvation model produces a G_{ads} curve qualitatively similar to that obtained from the vacuum simulations. Although implicit solvation includes a more physically accurate representation of the electrical double layer, it seems that it essentially captures the same physics of the adsorbate's response to the applied electric field as from vacuum calculations with applied saw-tooth potential.

As seen in Figure 4.3, Equation (4.2) can again be fitted to the O_2* adsorption free energy obtained from implicit solvation calculations. As seen in Table 4.1, it becomes clear that very similar values are obtained for the dipole $p_z = 0.22$ e $\cdot$ Å and polarizability $\alpha_{zz} = 0.12\ e \cdot$ Å^2/V as compared to saw-tooth potential in vacuum calculations. Both static methods capture the dipole-field effect, which, up

to now, seems to be the main driving force behind the potential dependence of the O_2 adsorption.

The primary quantitative difference observed with the inclusion of implicit solvation is an almost constant stabilization of approximately 0.1 eV in G_{ads}. This stabilization likely represents a small favorable interaction with the solvent, though it is somewhat dependent on the specific parameters of the model (detailed in Section 2.4.2). It is important to note that the implicit charging approach offers the technical advantage of achieving more stable electronic convergence under stronger electric fields. This improved stability is achieved with minimal additional computational cost compared to the vacuum simulations, making the implicit solvation model a more efficient and robust approach for simulating these systems under various field conditions.

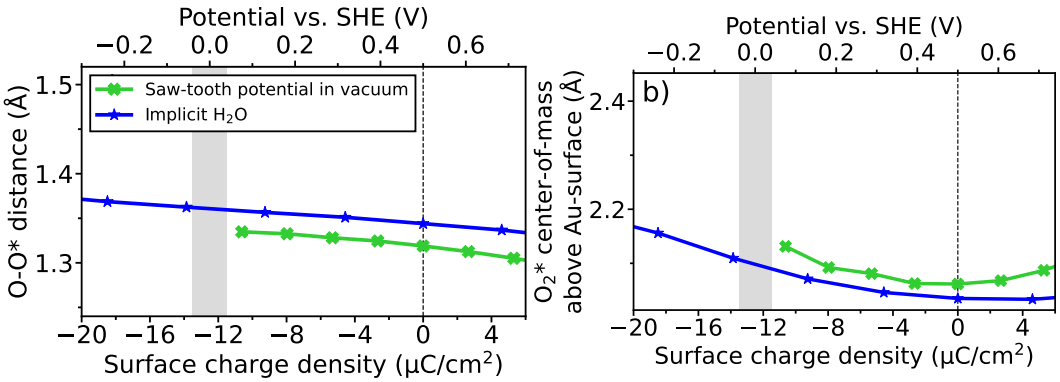

Figure 4.4: Average a) O-O* bond distance and b) O_2* center-of-mass distance from the Au surface (COM_z) as a function of surface charge density (bottom x-axis) and potential vs SHE (top x-axis). Compared are predictions regarding the O_2* bonding configuration from simulations using the saw-tooth-potential in vacuum (green crosses) and implicit H_2O (blue stars).

We characterize the O_2 adsorption state and compare saw-tooth potential in vacuum with implicit solvation calculations. The O_2* adsorption state lies parallel to the surface, with its center-of-mass position above a bridge position, consistent with previous studies [134]. Furthermore, it can be characterized by the intramolecular O-O* distance and the O_2* center-of-mass above Au-surface (COM_z) as shown in Figure 4.4. Figure. 4.4a) shows that the O-O* distance stays almost constant at around 1.32 Å for the saw-tooth-potential in vacuum calculations, and 1.36 Å for the implicit solvation results. These intramolecular O-O* bond lengths are common for the superoxo O_2* state. The larger intramolecular distance found from implicit solvation can be accounted for by solvation effects. Looking at the COM_z above the surface, the following trend can be found: The minimum of the COM_z lies at the PZC and going to more oxidative or reducing conditions, the O_2* slowly moves away from the surface. From implicit solvation calculations, the COM_z at PZC is 2.04 Å

and it goes up to 2.16 Å at 18.49 µC/cm^2. The saw-tooth potential in vacuum results shows a similar trend.

4.3 O_2 Adsorption at the Electrified Interface from Dynamic Simulations

4.3.1 O_2* Adsorption Energy: Dynamic vs. Static

To achieve more precise results and gain a deeper understanding of the complexity of the electrified metal/water interface, it is essential to at least include explicit water molecules in the simulation. We therefore choose AIMD simulations, as this enables us to add explicit water and observe the system's dynamics during a chosen time frame. The primary drawback of this method is its significant computational demand. AIMD simulations combine molecular dynamics simulations, which evolve the system over time, with density functional theory (DFT) single-point calculations performed at each time step to determine the forces, electronic energy, etc. Additional details are provided in Section 2.2. In this model, we conduct AIMD simulations within the NVT ensemble, sampling the O_2 and interfacial water structures at room temperature (for more technical details, see Section 2.3.2).

The interface is charged by supplying explicit counter-charge to the cores of randomly selected hydrogen atoms within the electrolyte. These charge-modified hydrogen atoms remain mobile within the H_2O network and are not expected to significantly influence the surface chemistry since we do not see water adsorption on the weak binding Au(111) surface. This can be seen in the water density plots including the positions of the re-parametrized H-atoms in Section 2.4.3. To sample multiple water structures, several 40 ps long trajectories were run with and without the O_2 for specified surface charge densities σ. In order to get the O_2* adsorption energy, the trajectories including O_2 are filtered to only include adsorbed O_2*. Since O_2 adsorption is not favored on the weak binding Au(111) surface, choosing the right adsorption descriptors becomes very crucial. We choose all images where the magnetic moment is lower than 1 μ_B and where the COM_z is lower than 3 Å. Furthermore, images where we have unwanted reactions happening, like e.g. the protonation of the O_2 to OOH* are also filtered out. Further information can be found in Section 3.5. The O_2* adsorption energy for each case is then determined from the difference in ensemble averages O_2* (see Section 3). By following a similar procedure used to calculate E_{ads}, we obtain G_{ads} as a function of σ. The free energy contributions are adjusted to the dynamical model as described in Section 3.3.

So let's have a look at the O_2* adsorption free energy G_{ads} vs. the surface charge

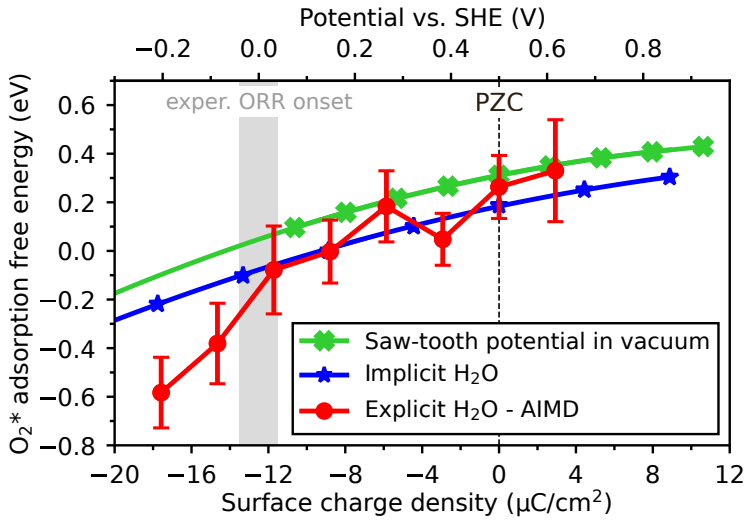

Figure 4.5: The free energy of O_2* adsorption at Au(111) is plotted as a function of surface charge density (bottom x-axis) and applied potential vs. SHE (top x-axis). The Figure compares different models of the electrical double layer are compared, as indicated in the legend: a vacuum background with applied sawtooth potential (green crosses), implicit solvation model (blue stars), and explicitly modeled H_2O via AIMD simulations (red circles). The vertical dashed line and the shaded gray area denote the PZC and the (approximate) experimental onset of the ORR, respectively.

density and compare it to the results from the static calculations as seen in the previous Section 4.2. In Figure 4.5, two distinct potential regimes can be identified. Near the PZC, G_{ads} demonstrates excellent quantitative agreement with the simpler vacuum and implicit H_2O models, exhibiting a similar trend of decreasing with potential. Therefore, we deduce that close to PZC, the O_2 adsorption is characterized and shaped by dipole-field effects as described by Equation 4.2. But going to very reducing conditions, around 0 V vs. SHE, a notable shift occurs as G_{ads} sharply decreases below zero and becomes more negative under increasingly reducing conditions. Interestingly, this transition corresponds with the approximate experimental onset of the oxygen reduction reaction (ORR), highlighted by the shaded gray area in Figure 4.5, as reported in previous studies [124, 126]. The shaded region accounts for the variability observed across different experimental investigations.

The inclusion of explicit H_2O solvent to the double layer model introduces a full atomistic representation of the dynamic interfacial H_2O network. Therefore, the second contribution becomes visible only for the results from AIMD as a change in slope of the O_2* adsorption energy when going to very reducing conditions. Stabilization effects on the O_2 due to hydrogen bonding are responsible for the deviation of the curve from the static calculation results. Such interactions contribute significantly

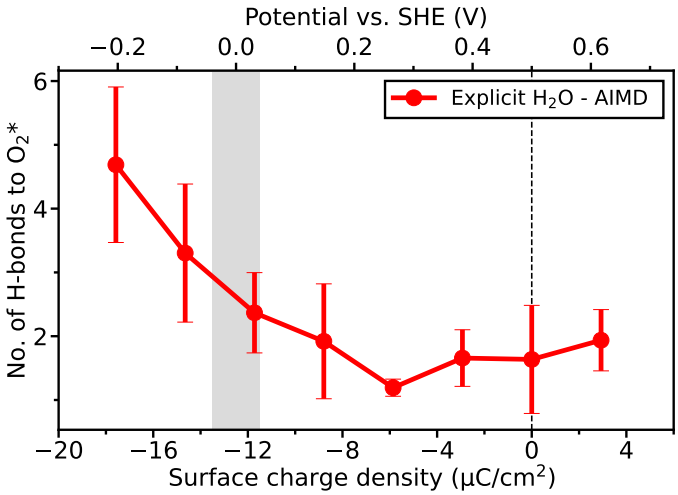

Figure 4.6: Average number of H-bonds to O_2* predicted from AIMD as a function of surface charge density (bottom x-axis) or applied potential vs SHE (top x-axis). The vertical dashed line and shaded gray area mark the PZC and (approximate) experimental onset of the ORR, respectively.

to the stronger O_2* binding observed under more reducing potentials on top of the dipole-field effects that still influence the shape of the curve, as can be seen in Figure 4.5. Detailed analysis of AIMD trajectories reveals an average of approximately two hydrogen bonds to O_2* in the high potential region near the PZC. Two criteria define H-bonds to the O_2*, following Heenen *et al.* [82]: the angle OO-H-OH $>$ 140 deg and the distance between the COM of O_2* and the oxygen of H_2O $<$ 3.5 Å . However, as indicated in Figure 4.6, this number increases linearly when the potential is reduced below 0 V vs. SHE or, equivalently, when the surface charge density σ falls below -12 µC/cm^{-2}. This stronger hydrogen bonding finally also leads to the spontaneous formation of OOH* during the AIMD simulations, a phenomenon that becomes more frequent at more negative potentials. This can be seen in Table 3.3, where only 3 trajectories are included for the results at very reducing conditions as compared to 7 trajectories at PZC. Interestingly, we find the experimental ORR onset close to the potential at which the O_2 adsorption becomes favorable and gains more H-bonds, enabling the formation of OOH*. This shows how the O_2* adsorption can very well be a rate-determining step.

4.3.2 O_2* Adsorption Configuration: Dynamic vs. Static

Now, one can take a closer look at the O_2* adsorption configuration to understand more in-depth what is exactly happening at the transition close to realistic ORR onset potentials. Again, we compare the two static models: The saw-tooth potential

in vacuum and the implicit solvation with the dynamic AIMD.

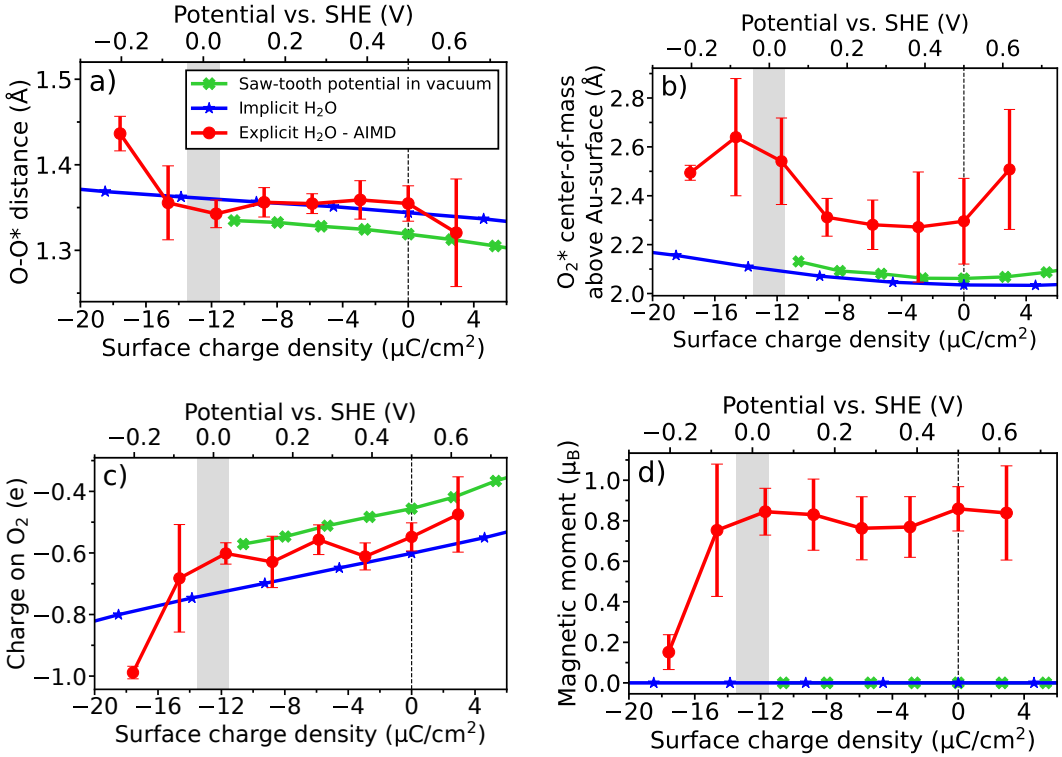

Figure 4.7: Average a) O-O* bond distance, b) O_2* center-of-mass distance above the Au surface (COM_z) c) the Bader charge [104–107] on the adsorbed O_2* and d) the magnetic moment as a function of surface charge density (bottom x-axis) and potential vs SHE (top x-axis). Compared are predictions regarding the O_2* bonding configuration from simulations using the saw-tooth-potential in vacuum (green crosses), implicit H_2O (blue stars), and explicit H_2O from AIMD (red circles).

In Figure 4.7a), the intramolecular O-O* distance is plotted vs. the surface charge density and potential vs. SHE. Again, we see good agreement with static calculations, except for the most negative surface charge density, where the mean O-O* distance goes towards 1.44 Å. The error bar of the O-O* distance at a surface density of -14.65 μC/cm^2 from AIMD is found to be large. We also find a substantial error for the value at very oxidative conditions. The latter we explain through the poor statistics and the highly unfavorable adsorbed O_2* state. The intramolecular O-O* distance from static calculations (saw-tooth potential in vacuum and implicit solvation) are very well in agreement, except when going to very reducing conditions. When looking at the COM_z from Figure 4.7b), generally we find the O_2* further from the weak binding Au(111) surface, but a trend is difficult to identify. We suspect that the O_2 adsorbs further from the surface due to some attraction between the O_2* and the explicit water. The error remains large, except at the most reducing potential

that we calculated from AIMD indicating a rather defined O_2 adsorption state. We conducted Bader charge analysis on the adsorbed O_2* [104–107]. Figure. 4.7c) and Figure 4.7d) show the evolution of the charge on O_2* and magnetic moment vs. the surface charge density, respectively. In both figures we see how close to PZC, an adsorbed O_2* state dominates with a Bader charge of around 0.6 e and magnetic moment of around 0.8 μ_B, but when going to very reducing conditions these values change to a higher charge on the O_2* of 1.0 e and a magnetic moment going to 0.1 μ_B. It seems that the nature of the O_2* changes when going to more reducing potentials. The transition of the O_2* state, as visible in Figure 4.7a), c) and d) at -14.65 µC/cm^2, is not visible in the static calculation results.

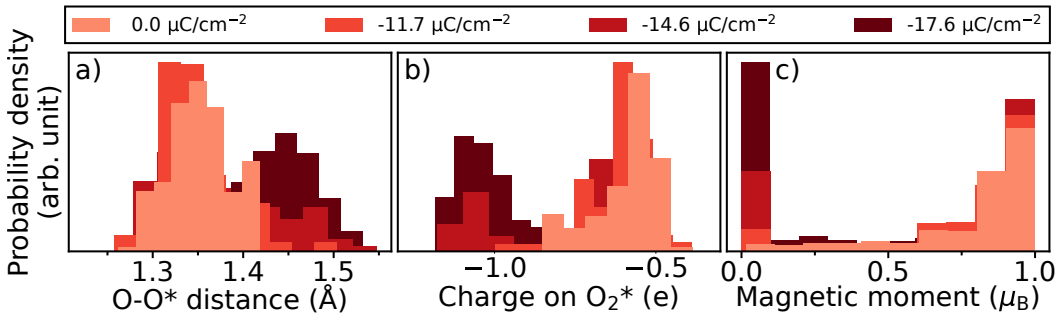

Figure 4.8: a) Probability density of the intramolecular O-O* distance for different values of surface charge density as listed in the figure's legend. The distribution distinguishes the superoxo from the peroxo O_2* dominating the surface at higher and lower potentials, respectively. b) and c) Same as a), but for the partial charge on O_2* as estimated from Bader charge analysis and magnetic moment predicted from AIMD.

To understand the transition in more detail, we plot the distributions of the O_2* adsorption properties at PZC and for surface charge densities where we detected the transition (close to experimental ORR onset potentials), as seen in Figure 4.8. It becomes clear that we have a bimodal behavior of the O_2* adsorption state. At a surface charge density of -14.6 µC/cm^2, we find both O_2* states co-existing leading to the rather large error in Figure 4.7. When comparing the O_2 adsorption state parameter at PZC vs. very reducing conditions as seen in Figure 4.8, it becomes clear that the observed transition is attributed to a potential dependent shift from a superoxo to a peroxo O_2* species at the surface. The peroxo species is characterized by an increased charge transfer from the metal surface to the molecule's anti-bonding 2π* orbitals, leading to i.a. a weakened O−O* bond and a magnetic moment of 0 μ_B. Further information on the definition of the O_2 adsorption state can also be found in Section 3.4. This transition cannot be seen for the static results since the magnetic moment is set to 0 μ_B by construction.

This transition leads to notable differences between the superoxo and peroxo O_2*

species in terms of their charge state, magnetic moment, intramolecular bond length, and O−O* stretching frequency, corroborating the findings of Panchenko et al. [138]. As illustrated in Figure 4.8, the O−O* bond length exhibits a bimodal distribution: a peak centered around 1.33 Å corresponds to the predominant superoxo state near the PZC, where the surface charge density σ is lower then -12 µC/cm^{-2}, while a second peak around 1.44 Å indicates the dominant peroxo state under more reducing conditions, where σ is below -12 µC/cm^{-2}. These bond lengths align with the definitions provided by Montemore *et al.* [39] that can be found in Section 3.4. A similar pattern is observed in the partial charge on the O_2* distribution, shown in Figure 4.8b), with peaks at 0.6 e and 1.1 e for the superoxo and peroxo species, respectively. The peroxo O_2* species could be regarded as a precursor state for proton-coupled electron transfer (PCET), given its tendency to protonate spontaneously to form OOH* or, less frequently, H_2O_2 during AIMD simulations. However, classifying this state as a definitive PCET precursor remains somewhat ambiguous based on our current simulations and warrants careful interpretation.

4.3.3 Free Energy Calculations

In the last part of our work, Umbrella sampling simulations were conducted for various σ values in a configuration that mirrors the one utilized for the AIMD. The resulting free energy landscapes helped us to understand in greater depth what states of the O_2 can be found at the electrochemical interface. These calculations were conducted by Elias Diesen, for technical information, see Ref. [1].

The free energy profile resulting from these simulations is depicted in Figure 4.9, illustrating the relationship between the COM_z and the increasingly reducing conditions (Figures 4.9 a)-c), from top to bottom). Firstly, when the system is at the PZC with σ=0 µC/cm^2, as shown in Figure 4.9a), a prominent physisorption well is observed approximately 3.2 Å above the surface, where O_2 is situated within the first water layer. The boundaries of this H_2O layer are estimated based on the H_2O density profile displayed in the bottom as Figure 4.9d). The shallow physisorption minimum has a weakly bound O_2 in its triplet spin state (μ=2 μ_B). The previous figures from AIMD, only take chemisorbed O_2* into account and do not include the physisorbed O_2. The data provided by Umbrella sampling can also be resolved by magnetic moment: A higher-energy (metastable) O_2* is revealed that can also be seen in the AIMD results as the endothermic chemisorption at PZC in Figure 4.5.

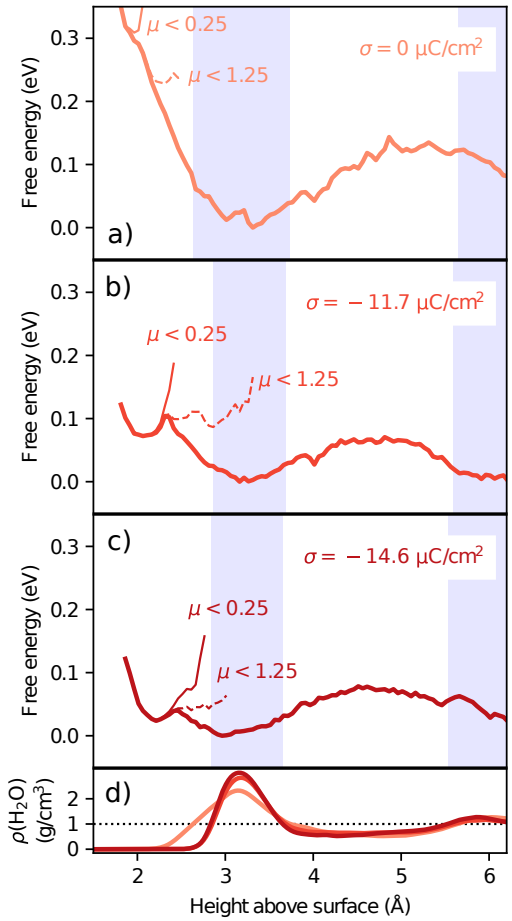

Figure 4.9: Free energy profiles a)–c) for progressively negative values of surface charge density, as a function of O_2 center-of-mass distance above the surface (COM_z), as predicted by umbrella sampling simulations. The chemisorption minima assigned to the peroxo (thin line, $\mu < 0.25$ μ_B) and superoxo (dashed line, $\mu < 1.25$ μ_B) states are revealed by resolving the full statistics of the free energy (thick solid line) concerning the magnetic moment. Based on the H_2O density profiles plotted in d), the shaded blue areas approximate the boundaries of the first and second interfacial solvent layers. The bulk H_2O density is shown by the dotted line in d).

We identify the peroxo O_2 state with a fully quenched spin and the superoxo O_2 state with a partially quenched spin between the surface and the first H_2O layer. The free energy minimum of the peroxo O_2 state is closer to the surface at around 2 Å, it has a negligible spin value (represented in Figure 4.9 as $\mu < 0.25$ μ_B) and an atomic configuration akin to that observed in a vacuum, where O_2* lies parallel to the surface with its center-of-mass positioned above the bridge site. The superoxo state, located further from the surface, is less distinct, represented by a broader region in

the free energy landscape and a wider range of possible spin values (in accordance with Ref. [39]). Although Figure 4.9 indicates $\mu < 1.25$ μ_B, varying the cut-off value for μ slightly shifts the relative population within the chemisorbed state, leading to minor differences in adsorption free energy without altering the qualitative results (refer to sensitivity analysis in 3.5). Between these two chemisorbed O_2* states, the superoxo state exhibits lower free energy, thereby rationalizing its preferential stability over the peroxo state around the PZC, as supported by AIMD observations.

When looking at Figure 4.9b) and Figure 4.9c) we can observe the evolution of the free energy landscape under increasingly reducing conditions. In Figure 4.9b) we can see two distinct changes: Firstly, both of the chemisorbed states shift energetically towards the physisorption minimum. This can be seen in the AIMD simulation results on Figure 4.5 where the O_2 adsorption becomes favorable, leading to more adsorbed O_2* images. The new minima of the chemisorbed O_2*, that can be observed now, moves away from the surface as the first interfacial H_2O layer becomes more compact. Secondly, the peroxo state becomes more stable compared to the superoxo O_2* state. This stabilization is increasingly significant at more negative σ, with Figure 4.9c) eventually showing a preference for the peroxo over the superoxo O_2*. It is crucial to note that only the inclusion of explicit adsorbate-solvent interactions can resolve the competition between these two states in our advanced model of the electrical double layer. This explains the sharper decline in G_{ads} at $\sigma < -12$ $\mu C/cm^2$ in Figure 4.5, attributed to the increasing peroxo population at the surface that leads to a stronger stabilization from H-bonding.

4.4 Summary

In conclusion, this chapter demonstrates that O_2 adsorption on Au(111) during the ORR is significantly influenced by the applied (absolute) potential due to local electric field effects and induced formation of the peroxo O_2* leading to enhanced stabilization from H-bonding. This finding indicates that O_2 adsorption constitutes an electrochemical step rather than a purely chemical one in the reaction mechanism. Specifically, we predict that while chemisorption is endothermic at the PZC, it becomes thermodynamically favorable around the experimental onset of the ORR at around 0 V vs. SHE. This observation supports the notion that O_2 adsorption could be the rate-determining step. Considering the O_2 as the rate-determining step can explain the experimental dependence of the overpotential on pH when measured on the RHE potential scale. For instance, converting the reaction onset from the SHE to the RHE scale yields approximately 0.06 V vs. RHE at pH 1 and 0.77 V vs. RHE at pH 13. These values, as discussed in previous studies [33, 91, 129, 132], should

be considered relative to the equilibrium reaction potential. Notably, the equilibrium potential of 0.70 V vs. RHE for the two-electron ORR, which dominates at the Au(111) electrode surface [125], translates to a significantly higher overpotential in acidic media compared to alkaline media. This effect is overlooked if potential dependence for O_2 adsorption within the PZC/CHE methodology is not considered, underscoring the importance of accounting for electric field effects in DFT models.

When predicting the system's response to applied potential, two effects of the local electric field are identified as contributing to the stabilization of O_2*. A dipole-field interaction predominates around the PZC, and this is captured even by simple and static double-layer models, such as applied saw-tooth potential in vacuum and implicit solvation calculations. This electrostatic effect alone is sufficient to recover a significant portion of O_2* stabilization with reducing potentials, owing to the adsorbate's substantial dipole moment. However, only an atomistic solvent model, as provided by AIMD, can account for the additional stabilization arising from directional hydrogen bonding within the H_2O network. Our findings show that this effect emerges around the experimental onset of the ORR, and we attribute its origin to the concurrent preference for a peroxo O_2* species at the surface. This state likely serves as a precursor to protonation, as evidenced by the spontaneous formation of OOH* in our AIMD simulations, thereby setting the stage for the subsequent step in the ORR mechanism. Finally, we show that neglecting non-PCET steps in the reaction mechanism, like here the O_2 adsorption on Au(111) for the ORR, and neglecting potential effects can lead to an incomplete representation and understanding of the electrochemical reactions.

Chapter 5

O_2 Adsorption on the Strong Binding Pt(111)

5.1 Introduction

In the previous chapter, our investigation revealed that the adsorption of O_2 on the Au(111) surface is highly dependent on the potential. Our work even implies that the O_2 adsorption might be the rate-determining step. This shows that neglecting potential effects on reaction steps that do not involve a proton-coupled electron transfer can lead to an incomplete representation and understanding of electrochemical reactions like here the ORR. Our analysis highlighted two primary factors causing the potential dependence of the O_2 adsorption: the dipole-field effects and the transition from superoxo to the peroxo O_2* leading to more stabilization from H-bonding. We have shown that to uncover the dynamics at the interface one has to include explicit water and charge the interface accordingly.

Nowadays, platinum-based catalysts are mostly used in fuel cell applications since platinum is known for showing high activity and stability [13]. Therefore, we will now move to investigate the more reactive Pt(111) surface: This chapter will draw a direct theoretical comparison of the O_2 adsorption on the weak binding Au(111) vs. the strong binding Pt(111) to estimate the role of the charged interface on O_2 adsorption and its implications for the ORR mechanism.

Let's have a look into the ORR mechanism: It is established that the two-electron pathway plays a major role on the weak binding Au(111) [124–126, 128, 129]. In contrast, on the strong binding Pt(111) surface, it is known that the four-electron pathway is dominating since the main product is water [139]. Figure 5.1 shows the two reaction mechanisms commonly assumed for the strong binding Pt(111).

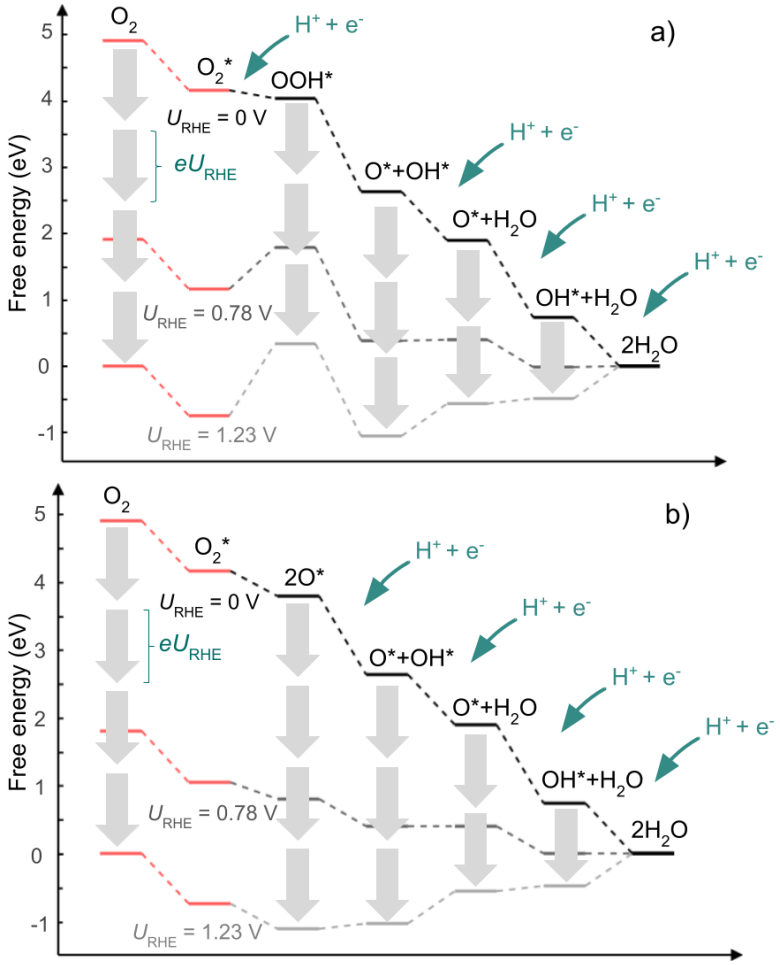

Figure 5.1: Common reaction mechanisms of the ORR on Pt(111): a) Associative mechanism and b) dissociative mechanism. The free energy for O_2* was calculated with vacuum DFT (see Section 2.3.1 and 3.3), the other free energies are from DFT vacuum calculations recovered from Hansen *et al.* [140]. The arrows show the influence of applied potential U_{SHE} with the help of CHE (see Section 1.2.3)

Figure 5.1a) shows the associative mechanism where the O_2* is stepwise reduced to OOH*, OH*+ H_2O and finally to 2H_2O. Secondly, Figure 5.1b) depicts the dissociative pathway, where the bond of the O_2* breaks to form 2O* species prior further reduction to 2OH* and 2H_2O. In literature, O_2 adsorption is often neglected as a chemical step, as it is likely not the RDS. Both reaction mechanisms calculated from DFT imply that the last reduction and hydrogenation step of the OH* to H_2O* is rate-determining as this is the first step to become unfavorable when going to higher potentials then 0.78 V. Unlike on the Au(111), we find no pH-dependence on the U_{RHE} scale, implying that the RDS should be a PCET step. It is still under vivid discussion if the ORR on Pt(111) follows the associative or dissociative pathway as

it is not easy to distinguish between the pathways from an experimental point of view [13, 18, 19]. However, platinum-based catalysts are still dominating fuel cell applications, so there is a large amount of information available from experiments: Electrochemical [16, 141], structure sensitivity [142], single-crystal [139, 143] and spectroscopic data [144] are available [8].

The significance of platinum-based catalysts has motivated a large amount of theoretical benchmark studies including Pt(111) [145], yet from a theoretical point of view, a myriad of open questions remains: Not only is the pathway still unknown [24, 145], but also the rate-determining step is still under debate [11, 146]. Among these challenges, one area currently receiving notable attention is the effect of the local interfacial field, which arises from the capacitive charging of the electrical double layer (cf. e.g., Refs [91, 147–149]). Open questions in this area include, for instance, how these effects manifest under realistic operating conditions, and to what extent they can influence reaction mechanisms and, consequently, catalytic performance. It is generally accepted that local field changes the binding energy not only of dipolar but also of polarizable intermediates, which can influence a reaction mechanism. Since the utilization of local field effects is being proposed as a strategy to enhance catalyst design [150, 151], it is becoming increasingly crucial to develop a fundamental understanding of these effects and their transferability across different catalytic systems.

The effect of the potential on the O_2* on Au(111) has been thoroughly described in Chapter 4. Building upon these previous insights, we go beyond static density functional theory (DFT) calculations representing static images of the interface in a charge-neutral environment corresponding to PZC conditions. Our main method at hand is AIMD (see Section 2.2). In order to understand and compare the potential effect, we focus on the O_2 adsorption and the subsequent ORR step at the interface. Although we do not anticipate these steps to be rate-determining [152], the response to the applied potential and even the mode of O_2 binding under ORR conditions have remained unclear up to date. When looking at the strong binding Pt(111), as shown by previous literature [153], one cannot neglect the role of surface-adsorbed species on the strong binding Pt(111). We, therefore, conduct AIMD simulations of an exemplary OH*-covered Pt(111) surface with 5/12 ML OH* [154] to get an idea of realistic ORR conditions. In the following chapter, we will not only discuss the results of the AIMD simulations on the clean Pt(111) and the OH*-covered Pt(111) slab, but we will also draw a direct comparison with the results from the weak binding Au(111) surface to understand the role of the reactivity of the metal catalyst surface on the O_2 adsorption under field effects.

In contrast to Au(111), we observe negligible potential dependence of the binding

of molecular O_2 on Pt(111). This result holds true for both the clean surface and a more realistic OH*-covered catalyst model. This can be explained by the inherently different reactivity of the two metal surfaces. On Pt(111), dipole-field effects do not play a major role for the rather tightly adsorbed O_2*. The O_2* state on Pt(111) is characterized by a peroxo species with a relatively constant number of H-bonds, irrespective of the potential. Additionally, we find that co-adsorption of OH* minimally impacts the O_2* adsorption energy. However, we see a strong potential dependence of H_2O* adsorption and the water structure at the interface. Nevertheless, the O_2* adsorption state does not seem to be strongly influenced by the change in water structure at the interface on Pt(111). Interestingly, we observe facile O_2* dissociation and consecutive hydrogenation in our simulations. We find an indirect effect of the potential on the more realistic OH*-covered Pt(111): When going to reducing conditions, we see H_2O* desorption promoting the O_2* dissociation. Although the ORR steps we investigate on the Pt(111) surface are most likely not rate-determining, we again find a potential effect, albeit indirect through the surface coverage species, of a non-PCET step. Again, this finding implies that one must go beyond the charge-neutral picture to understand electrochemical reactions like the ORR.

5.2 O_2 Adsorption: Au(111) vs. Pt(111)

In this work, we follow a similar framework as in the previous chapter but focus mainly on using AIMD simulations to sample the structures of O_2* and interfacial water at room temperature, as detailed in Section 2.2. To model the electrical double layer and the resulting potential drop that drives the catalytic ORR, we charge the interface by introducing an explicit counter-charge to randomly selected hydrogen atoms of the electrolyte (see Section 2.4.3). This approach enables us to observe the potential dependence of the O_2* adsorption free energy G_{ads} and to compare the behavior of the O_2 on Au(111) vs. Pt(111) within a potential range that is realistic for ORR operation. On Au(111), the experimental onset can be found around 0 V vs. SHE [155], or, equivalently -0.5 V vs. the experimental PZC [94], which can be estimated to be around σ=-12.5 µC/cm^2 according to Equation (2.42). This value is independent of pH [155]. This picture changes on Pt(111); it is well established that we find a Nernstian shift with pH on the SHE scale [152]. Therefore, U_{SHE} and pH cannot be decoupled: The onset is around 0.1 V vs. SHE [139], which equals -0.2 V vs. PZC [94] or ca. σ=-5.0 µC/cm^2 at pH 14. Here, it is important to note that we only approximate the potential from the surface charge density with the help of Equation (2.42). We use the potential vs. PZC to compare Au(111) vs. Pt(111). Yet, using a constant U_{PZC} for the strong binding Pt(111), where we find various

surface coverages, is a rather crude approximation.

Following the previous framework, multiple simulation trajectories, both with and without O_2*, are conducted for specific surface charge densities σ. The O_2* adsorption energy, $E_{\text{ads}}(\sigma)$, is calculated from the difference in ensemble averages, focusing exclusively on chemisorbed O_2*, as discussed in Section 3. A more negative E_{ads} value signifies stronger binding to the electrode. The trajectories were filtered to include only those images with chemisorbed O_2* for calculating $E_{O_2^*}(\sigma)$ (see Section 3). As described in Section 3.3, we adjust $E_{O_2^*}(\sigma)$ to account for the over-binding of gaseous O_2* from DFT [110] and free energy contributions. This adjustment ultimately provides the free energy of O_2* adsorption, $G_{\text{ads}}(\sigma)$, as a function of the applied surface charge density.

In addition, we also investigate the effect of OH*-covered Pt(111). Next to the inherent adsorption of water that is already captured on the clean Pt(111) slab when including explicit H_2O, it is well-documented that the reactive Pt(111) surfaces under operational ORR conditions exhibit partial coverage by hydroxyl species OH* [144]. We repeat our AIMD simulations with a more realistic 5/12 ML OH* coverage on Pt(111), which is predicted to be the most energetically stable configuration for the potential range -0.1 to 0.1 vs. SHE (at pH 14), just below the ORR onset [154]. In that work, Kristoffersen *et al.* [154] coupled AIMD simulations at the PZC with the CHE framework to simulate potential dependent coverage. To understand the composition of the surface coverage species in greater detail under realistic conditions, it would *inter alia* require a comprehensive exploration of the surface phase diagram (including capacitive charging) and going towards larger unit cells, which is beyond the scope of this work.

The resulting O_2* adsorption free energies are shown in Figure 5.2: In contrast to the Au(111) and as expected from the more reactive Pt(111) surface, we see a favorable O_2 adsorption at all surface charge densities that we simulated. At PZC, the O_2* binding is much stronger at Pt(111) with $>$ 1 eV difference; measuring specifically $G_{\text{ads}}^{\text{PZC}}$ = 0.26 eV at Au(111) vs. $G_{\text{ads}}^{\text{PZC}}$ = -0.92 eV at Pt(111). The results at PZC closely align with those obtained under vacuum conditions, where the predicted adsorption free energies at the PZC are $G_{\text{ads}}^{\text{PZC}}$ =0.31 eV for Au(111) and $G_{\text{ads}}^{\text{PZC}}$ = -1.15 eV for Pt(111). When adding 5/12 ML OH* to the clean Pt(111), the O_2* adsorption free energy is very comparable to the clean Pt(111) result. We observe a small stabilization on the OH*-covered Pt(111) slab. The mean O_2* adsorption free energy for the clean Pt(111) is -0.90 eV, for the OH*-covered Pt(111) we find -1.03 eV.

Secondly, the Pt(111) results show almost no potential dependence. In contrast, as described in the previous Chapter, the adsorption of O_2 on Au(111) exhibits a strong

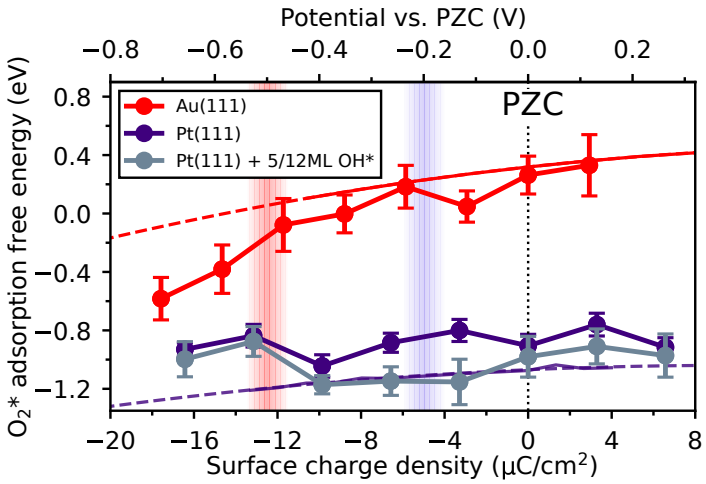

Figure 5.2: The free energy of O_2* adsorption is shown as a function of surface charge density (bottom x-axis) and approximate applied potential vs. PZC (top x-axis), comparing three metal surfaces as indicated in the legend: clean Au(111) (red), clean Pt(111) (purple), and Pt(111) with 5/12 ML pre-adsorbed OH* (grey). The dashed lines illustrate the electrostatic response of O_2* due to dipole-field interactions within the vacuum background models of Au(111) and Pt(111). The vertical dotted line and the shaded colored regions denote the point of zero charge (PZC) and the approximate experimental onset potentials for the oxygen reduction reaction (ORR): the red region corresponds to Au(111) at all pH levels [155], and the purple region represents Pt(111) at pH 14 [139], respectively.

dependence on the applied potential: The adsorption free energy G_{ads} decreases by approximately 0.9 eV across the investigated potential range. Specifically, O_2* adsorption is not favored near the PZC but becomes increasingly favorable under highly reducing conditions. We will start with comparing the two main effects leading to the slope as explained in the previous chapter: i) dipole-field effects dominating close to PZC and ii) stabilizing hydrogen bonding with the adsorbed O_2* at more reducing conditions.

With the goal of understanding the dipole-field effects, we conduct saw-tooth potential in vacuum calculation for the clean Pt(111) surface. The results, represented by the lines that are interpolated by dashed lines, are shown in Figure 5.2 for the Au(111) and Pt(111) surfaces in red and purple, respectively. We make use of the previously discussed conversion between surface charge density, electric field, and potential using Equation (2.42) in Section 2.4. On Pt(111), the data from this straightforward model is well in agreement with the AIMD results, while on Au(111), we find this agreement only close to PZC. The agreement shows how the dipole-field effects dominate the O_2* adsorption. Again, we find weak potential dependence for the Pt(111)

surface. Building on the framework established in Chapter 4 for Au(111), we fit the results from the saw-tooth potential in vacuum to the truncated second-order polynomial [91]:

$$G_{\text{ads}}(\vec{E}) = G_{\text{ads}}^{\text{PZC}} + \vec{p}\,\vec{E} - \frac{\alpha}{2}\,\vec{E}^2 \tag{5.1}$$

which lets us investigate the strength of the dipole-field effects. The intrinsic O_2* dipole moments are predicted to be p_z= 0.08 e·Å for Pt(111) vs. p_z= 0.21 e·Å for Au(111) i. e. a slope more than two times smaller at Pt(111) vs. Au(111). The corresponding polarizability values are also lower for Pt(111), with α_{zz} = 0.12 e·Å^2/V compared to α_{zz} = 0.15 e·Å^2/V, which aligns well with findings from other studies [91] as shown in Table 5.1.

	Au(111)		Pt (111)	
	p_z (e·Å)	α_{zz} (e·Å^2/V)	p_z (e·Å)	α_{zz} (e·Å^2/V)
Our work	0.21	0.15	0.08	0.12
Kelly *et al.* [91]	0.24	0.13	0.12	0.11

Table 5.1: Dipole moment p_z and polarizability α_{zz} components along the surface normal as extracted from fitting Equation (5.1) to the O_2* adsorption energy vs. the electric field at Au(111) and Pt(111) which are calculated via saw-tooth potential in vacuum calculations. The first row gives the results from our investigations while the second row shows results from Kelly *et al.* [91].

The dipole moment difference between the two metal catalysts is attributed to the inherently different reactivity between the two surfaces. The formation of a stronger chemical bond at the Pt surface results in a weaker adsorbate-induced dipole because the O_2* molecule is positioned closer to the surface. It is known that the metal-adsorbate bond length changes the dipole moment sensitively [156]. This is well in agreement with the observed change of COM_z: At PZC, from vacuum calculations, the difference of COM_z is 0.10 Å between the two surfaces, and from electrochemical AIMD simulations, we find a more pronounced difference of COM_z (0.33 Å).

Let's take a look at the second contribution that plays a major role on the Au(111) as explained in Chapter 4: The H-bonds to the adsorbed O_2*. This contribution leads to an additional stabilization of the O_2* adsorption around the ORR onset on Au(111) as depicted in Figure 5.2. This can be seen as a change in slope at around $\sigma < -12\,\mu\text{C/cm}^{-2}$, where G_{ads} drops abruptly below zero and becomes increasingly negative at more reducing conditions. As above, we define the H-bonds to the adsorbed O_2*: Two criteria define H-bonds to the O_2*, following Heenen *et al.* [82]: the angle OO-H-OH > 140 deg and the distance between the COM_z of O_2* and the oxygen of H_2O < 3.5 Å. It is important to mention that these criteria don't

give quantitative results, but it becomes possible to see trends in the H-bonds to the O_2*.

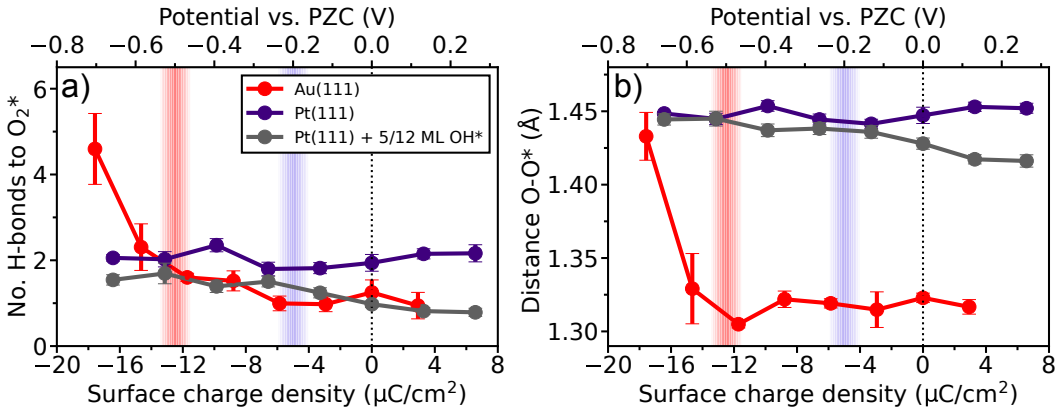

Figure 5.3: a) The average number of H-bonds to O_2* from AIMD simulations and b) the intramolecular O-O* distance, plotted against the surface charge density (bottom x-axis) or applied potential versus SHE (top x-axis). The transparent blocks indicate approximate experimental onsets for Au(111) (red) and Pt(111) (purple) [131].

Figure 5.3a) shows the number of H-bonds to the adsorbed O_2* throughout the potential span investigated. For Au(111), close to PZC, we count an almost constant average of about 1.5 H-bonds to O_2* in the high potential region around the PZC. However, this situation changes to a linearly increasing number of H-bonds when further reducing to $\sigma < -12\,\mu C/cm^{-2}$. As described in great detail in Chapter 4, this change is the potential dependent transition from a superoxo to a peroxo O_2* species adsorbed at the surface. Further details on the O_2 states can be found in Section 3.4. When going from superoxo to peroxo species, the charge from the metal surface is being transferred into the molecule's anti-bonding 2π* orbitals, leading to consistently changing observables like, e.g., prolongation of the intramolecular O-O* distance, lowering of the magnetic moment and a changing O−O* stretching frequency [138]. In assigning the O_2* oxidation state, we use the intramolecular O-O* distance here as a descriptor. We plot the intramolecular O-O* distance vs. the surface charge density in Figure 5.3b): on Au(111), the O-O* distance is around 1.32 Å close to PZC characterizing the superoxo state, but going to very reducing conditions the O-O* distance is being prolonged to 1.43 Å implying a peroxo O_2* species. Montemore *et al.* [39] reports an intramolecular bond length of 1.35 Å for the superoxo O_2* and 1.45 Å for the peroxo O_2* species, which supports our assignment of the two species.

On Pt(111), again, we see negligible potential dependence in Figure 5.3a): The H-bonds to the O_2* are constant for the investigated range of surface charge densities.

For the clean Pt(111) slab, the mean H-bonds to the O_2* are 2.04, while for the OH*-covered Pt(111) slab, we count 1.24 H-bonds to the O_2* in the mean. Figure 5.3b) shows the intramolecular O-O* length evolution vs. the surface charge density. On Pt(111), we see that the adsorbed O_2* has an almost constant intramolecular bond length throughout the whole potential range indicating a peroxo O_2*: For the clean Pt(111), we have a mean intramolecular bond length of 1.45 Å, while when looking at the OH*-covered Pt(111), the intramolecular bond length in the mean is 1.43 Å. To put it into a nutshell, on the Pt(111) surface, we only see peroxo O_2* independent of the potential, while on the Au(111), we have a transition from superoxo- to peroxo O_2* species at reducing conditions adding another contribution to the potential dependence of the O_2* adsorption.

5.3 O_2* Adsorption Configuration: Au(111) vs. Pt(111)

Now we will turn to inspect the O_2* adsorption configuration from AIMD: We investigated the COM_z above surface (Figure 5.4a)), the partial charge on the adsorbed O_2* from Bader charge analysis (Figure 5.4b)) and the magnetic moment (Figure 5.4c)) vs. the surface charge density. On Au(111), the O_2* sits rather far away from the surface, the COM_z is not very well defined with a mean value of 2.53 Å. Close to PZC, we find a partial charge of around -0.6 e and the magnetic moment is rather high at around 0.75 μ_B. When going to reducing conditions, more charge is transferred into the O_2* and the magnetic moment goes towards 0 μ_B which is in agreement with our predicted transition from superoxo to peroxo O_2*. We find the O_2* loosely adsorbed which leads to a rather undefined adsorption site with a small preference towards the bridge site, as seen in Figure 5.5a).

Contrary to the O_2* state transition predicted on Au(111), Figures 5.3 and 5.4 indicate that the scenario remains unchanged on Pt(111) across the entire range of potentials we investigated. Furthermore, adding 5/12 ML OH* does not lead to major changes in O_2* configuration. We observe a consistent average of about two hydrogen bonds (Figure 5.3a)), with no noticeable effect from surface charging. O_2* stays in what we classify as a peroxo-like state with an intramolecular O-O* distance of approximately 1.45 Å (Figure 5.3b)), a Bader charge of around -0.8 e (5.4b)) and an almost completely quenched spin of $\mu \approx 0.1$–0.2 (5.4c)).

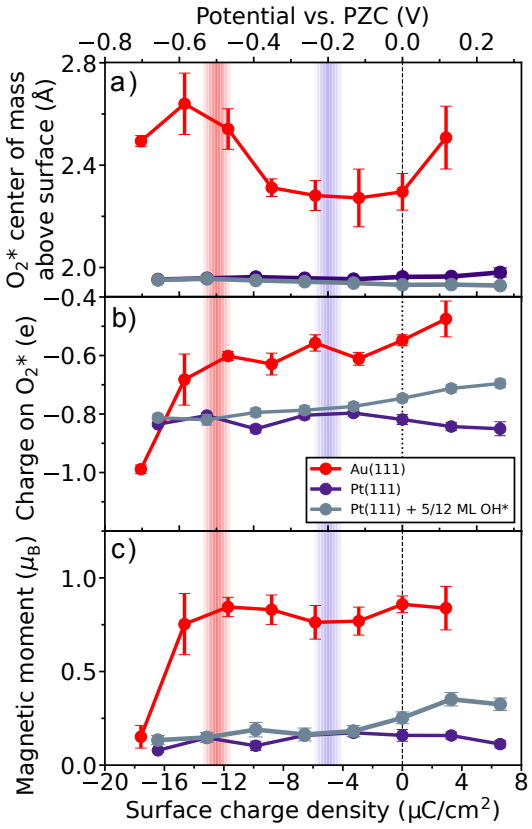

Figure 5.4: a) Mean center-of-mass above metal surface (COM_z), b) mean Bader charge and c) the mean magnetic moment of the adsorbed O_2* vs. surface charge density for Au(111) (red), Pt(111) (purple) and Pt(111) + 5/12 ML OH* (grey). The adsorbed O_2* state on Pt(111) is so clearly defined that the error bars are not visible. Dissociated and protonated O_2* are not included.

Another question is why there is a difference of charge on the peroxo species on the Au(111) vs. the peroxo species on the Pt(111) surface: We suspect this could be due to how the partial charge is denoted in Bader charge analysis. Defining charges is a difficult task at hand and Bader charge analysis only gives a way to approximate the electronic charge [104–107].

On Pt(111), the molecule lies flat on the surface with a COM_z of around 2.0 Å above a bridge site (see Figure 5.4b) and Figure 5.5)). This preference for the bridge site aligns with our vacuum-background calculations and previous work [157–159]. However, literature generally shows variation depending on the specific set-up and chemical environment [158, 160–162].

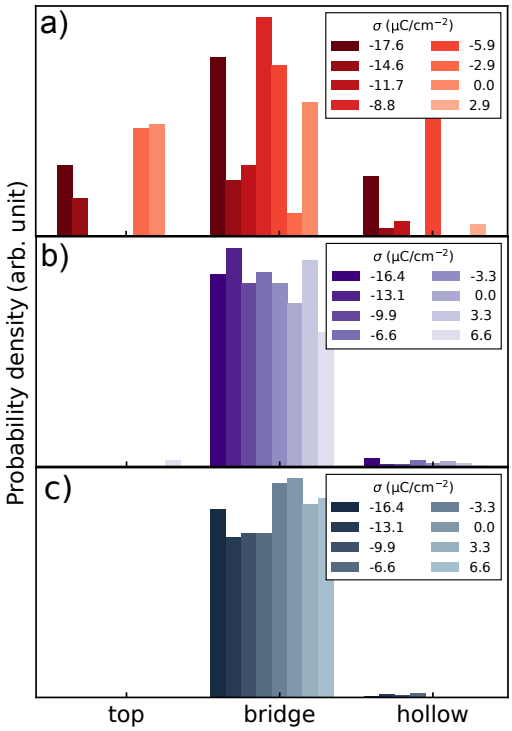

Figure 5.5: Distribution of adsorption site of the adsorbed O_2* for a) Au(111) (red), b) Pt(111) (purple) and c) Pt(111)+5/12 ML OH* (grey).

Furthermore, we compute the free energy profile of O_2 on Pt(111), including explicit H_2O, which supports our observation that the peroxo O_2* at the bridge site dominates (for our set-up). These calculations were conducted by Elias Diesen; for in-depth technical information, see Ref. [2]. Figure 5.6 displays the corresponding free energy landscape as a function of the molecule's COM_z distance from the surface, with a clearly defined molecular and chemisorbed O_2* state at a height of 2.0 Å and an adsorption free energy G_{ads} of -1.5 eV at the PZC (solid purple line). Spin-resolved analysis confirms this state's peroxo character with $\mu < 0.1$ μ_B. Additionally, our analysis uncovers a superoxo O_2* state ($\mu \approx 0.8$ μ_B), which prefers the top site and has a slightly tilted O-O* axis, but this state forms a less stable, shallow chemisorption well around a 2.7 Å COM_z height. This qualitative picture also holds under more reducing potential conditions of σ =-16.4 μC/cm^2 (dashed purple line in Figure 5.6). Therefore, we conclude that the dominant O_2* state on Pt(111) is peroxo, with no potential dependence in either the oxidation state of the molecule or its H-bond interactions with the solvent, at least within the relevant ORR potential range.

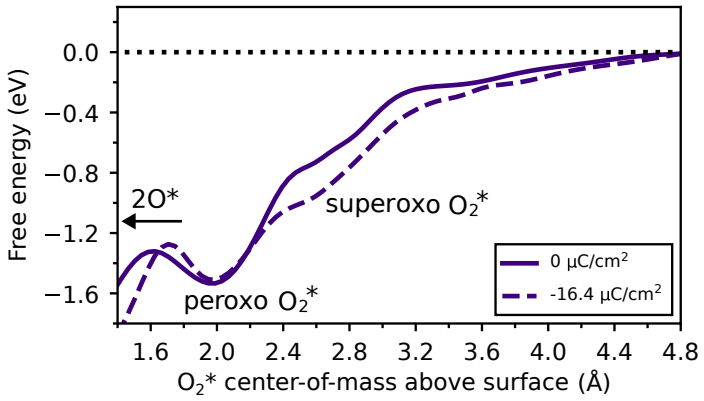

Figure 5.6: The free energy profile of O_2 is shown as a function of the COM_z. The energy values are obtained using umbrella sampling under PZC conditions (solid line) and more reducing conditions with a surface charge of σ = -16.4 μC/cm^2 (dashed line), using the O_2 state at a height of 4.75 Å as the zero-energy reference point [2].

When comparing the peroxo state on Pt(111) vs. the peroxo state on Au(111) in Figure 5.3a), one main difference is that the peroxo species on the Au(111) has much more H-bonds to the O_2* then the peroxo species on Pt(111). This can partly be explained via the COM_z as shown in Figure 5.4a). The close proximity of the adsorbed O_2* to the metal surface simply leads to a reduction in the exposed surface area of the molecule that is available for interactions like, e.g., the H-bonding. The key missing piece is understanding where the H-bonding donating water molecules sit with respect to the O_2*. Furthermore, when adding OH* to the surface, there are even fewer H-bonds to the O_2* as seen in Figure 5.3b). To fully understand this observation, a thorough investigation of the water structure will be shown in the next section.

5.4 Water Structure at the Interface: Au(111) vs. Pt(111)

To answer the remaining questions about the interplay between water structure and O_2* adsorption, we look at the water structure's potential dependence at the metal/water interface.

Figures 5.7-5.9 describe the water structure for each surface charge density (going to reducing conditions with increasingly darker colored lines and *vice versa*) for Au(111), Pt(111) and the OH*-covered Pt(111), respectively. We use the trajectories

without O_2*, but note here that the O_2* does not significantly change the water structure at the interface [2]. Additionally, we only include molecules that we define as H_2O and neglect OH* in the representation as they stay adsorbed at the interface at all times. We distinguish between them by searching for the closest oxygen from every hydrogen present. If the oxygen is then the closest to two hydrogen atoms, we define it as water; if the oxygen is closest to only one hydrogen, we denote it as OH*.

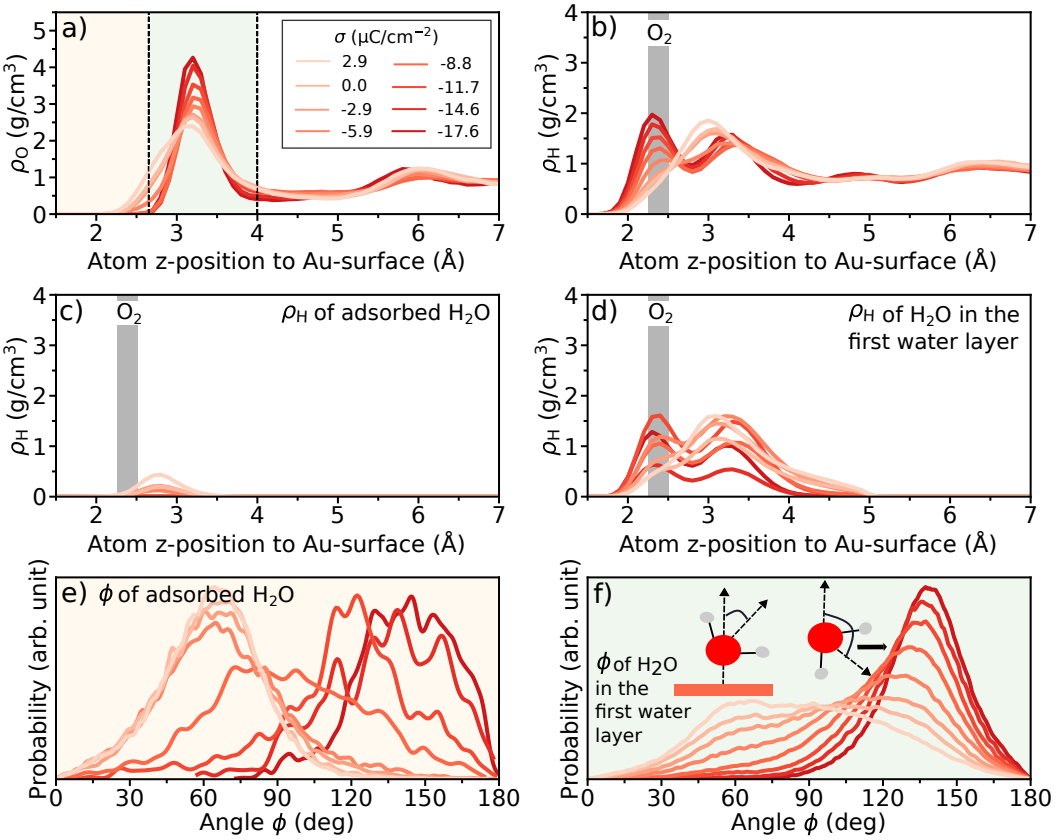

Figure 5.7: a) O(H_2O) densities and b) H(H_2O) densities of the water calculated for Au(111). The first black dashed line at 2.65 Å is used as a descriptor to define adsorbed water. The second black dashed line at 4.00 Å denotes the end of the first water layer. The H density of the adsorbed water and the H(H_2O) density of the first water layer are displayed in panels c) and d), respectively. The shaded grey region indicates the location of the adsorbed O_2*. The lower panels illustrate the probability distribution of the angle ϕ, representing the angle between the water bisector and the surface normal, for e) the adsorbed water layer and f) the first water layer.

Panels a) show the average water density resolved as oxygen density ρ_O. Building upon previous work [82] and the visible peaks in our water structure figures, we define the adsorbed water as water whose O(H_2O) is closer than 2.65 Å to the metal catalyst

surface. We estimate that the first water layer spans from 2.65 Å to 4.00 Å. While this representation is not new [154, 163, 164], this classification becomes useful to understand the interfacial water structure and for identifying the H-bonds donating H_2O.

Panels b) shows the average hydrogen density ρ_{H} vs. atom z-position to the metal surface, and the grey area denotes the position of O_2*. Panels c) and d) show the H density ρ_{H} of the adsorbed and first water layer, respectively.

Lastly, panels e) and f) show the angle ϕ between the water bisector (the vector that divides the angle between the two hydrogen atoms in a water molecule equally) vs. the surface normal for the case of adsorbed H_2O* and first water layer H_2O, respectively. Closer to 0 deg means the water is in an O-down configuration with the hydrogen atoms pointing up concerning the metal surface. Going to 90 deg, the water orientation shifts towards a flat-laying water molecule. Lastly, going to 180 deg, this picture changes again, and we see the two-H-down orientation with the oxygen pointing away from the surface.

Let's discuss the first figure investigating the interfacial water structure on Au(111): The first water layer dominates for all surface charge densities, which can be seen as a peak between $2.65-4.0$ Å in Figure 5.7a). Close to PZC, we observe a rather broad peak for both, the ρ_O and ρ_H, indicating that the water is agile and free within the first water layer. This agrees with the water orientation close to PZC; the water does not show much preference, and the angle spans from 45-135 deg. The water moves freely between a two-H-down, flat-lying, and O-down configuration, preferably in the first water layer. When looking at Figure 5.7a) we see a small amount of water counted as adsorbed close to PZC. It is not clear if this water should be counted as chemisorbed since it seems like the shoulder of the first water layer peak.

Now, going to reducing conditions, this picture changes: The O-density peak in the first water layer becomes more pronounced, and two peaks are visible in the H-density, implying a one-H-down configuration. The one-H-down configuration is further confirmed in Figure 5.7f), where at reducing conditions, we see a well-defined peak at ≈ 135 deg dominating. With the negative charge at the surface, the partially negatively charged oxygen of the water molecule is being repelled. Our Au(111) findings align well with literature [163], where the surface was investigated at even lower potentials, showing similar trends.

In the next step, we can compare the water structure on the more reactive Pt(111): In Figure 5.8, close to PZC, we can observe a peak emerging close to the surface ($<$ 2.65 Å) denoting adsorbed water. The hydrogen density peak associated with those adsorbed water molecules can be seen in Figures 5.8b)-c): The hydrogen density

peak can be found around 2.5 Å atom z-position to the surface, a bit further away from the adsorbed water/oxygen density peak in Fig 5.8a), indicating an O-down configuration. This can be further backed up by the observation in Figure 5.8e): The adsorbed waters prefer to adsorb at around $\phi = 60$ deg. Close to PZC, the first water layer is still prominent with little preference (30-160 deg) regarding the water orientation: The water slightly prefers to sit in a two-H-down configuration at higher angles (around 120 deg), but some water can also be found at lower angles down to 30 deg taking on an O-down configuration as seen in Figure 5.8f), which is further backed by a very broad peak of the water first layer H density as shown in Figure 5.8d).

When going to more reducing conditions, H_2O adsorption becomes negligible on the strong binding Pt(111) (see Figure 5.8a) and c)). The negatively charged interface becomes more hydrophobic and resembles the Au(111) water structure surprisingly well: The first water layer becomes even more prominent (see Figure 5.8a)) with a one-H-down configuration at around $\phi = 135$ deg (see Figure 5.8d) and f)). The water structure found agrees with previous work by Le *et al.* [164], where AIMD simulations were conducted with charge controlled by adding Na or F atoms.

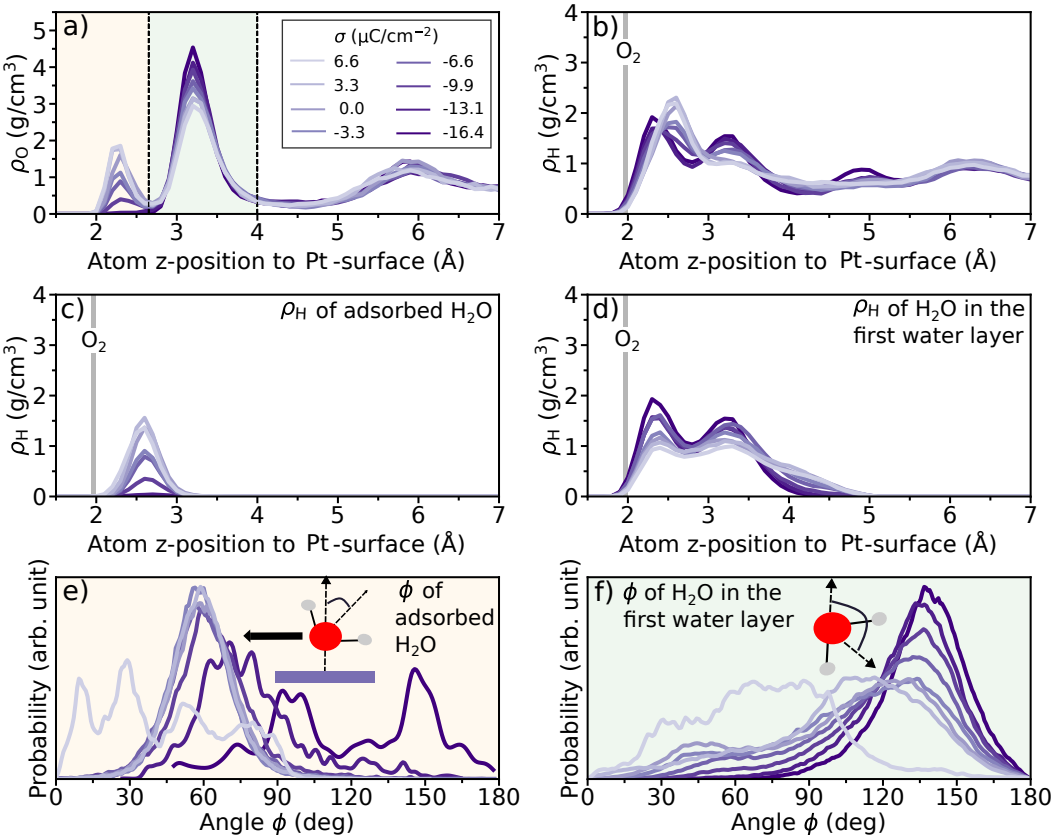

Figure 5.8: Same as Figure 5.7, but for Pt(111)

The water structure changes drastically once we start adding surface coverage species. As explained before, to represent the water structure with more realistic surface coverages, we choose 5/12 ML OH* as an exemplary approximation following Kristoffersen *et al.* [154]. They conducted AIMD simulations to find the most favorable coverage species at potential conditions that are of interest for ORR. They show that 5/12 ML OH* is the most favorable configuration in the potential region we are interested in while using a similar set-up. Again, it is essential to note that OH* species are not included in the Figure 5.9.

Close to PZC, as seen in Figure 5.9a), the first water layer is fully depleted, and significantly more water adsorption is induced. A very stiff surface cover ("hydrophobic layer" [165]) forms in the *xy*-plane on the surface, where the water molecules lay almost flat on the surface at around 60-90 deg (see Figure 5.9c)), showing a tendency to the O-down configuration. This also leads to the dominant peak in the adsorbed water layer of the H-density close to PZC as shown in Figure 5.9b) and c). We observe lively H-exchange between the adsorbed OH* and H_2O* in the *xy*-plane, leading to a dynamic hydrogen network. The OH* does not desorb [2]. Close to PZC, we find a "vacuum" region outside the "hydrophobic" H_2O*+OH* layer.

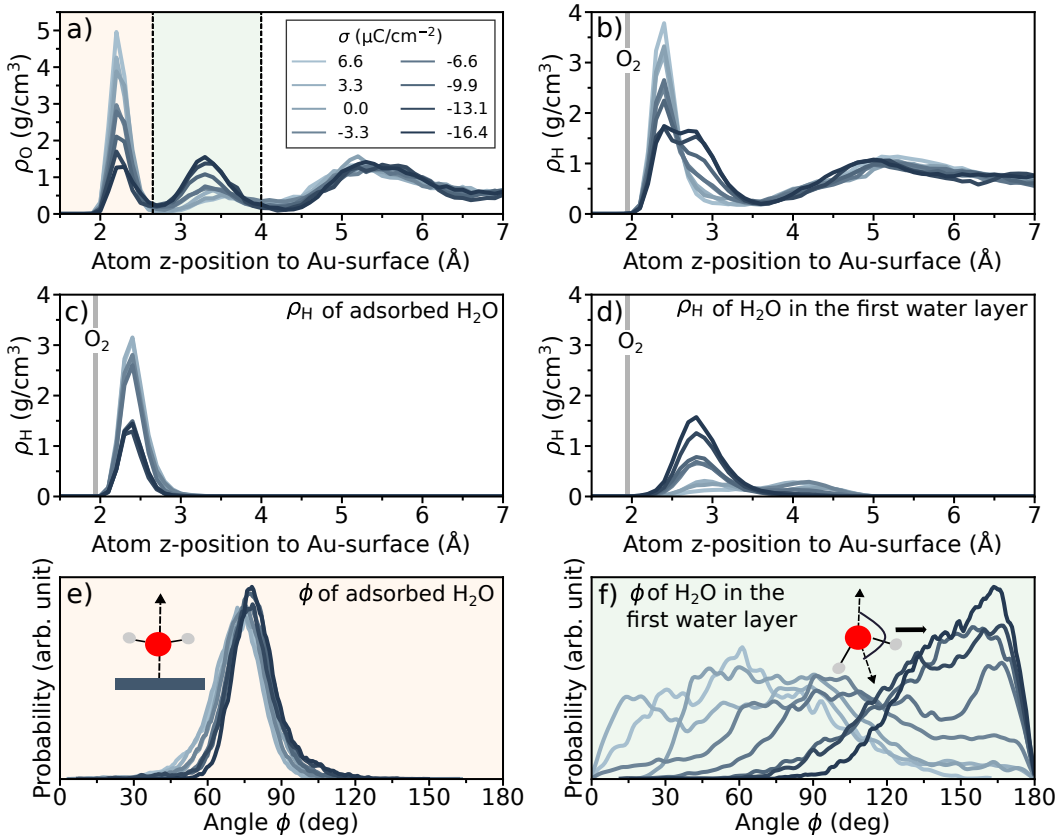

Figure 5.9: Same as Figure 5.7, but for OH*-covered Pt(111)

When going to reducing conditions, the surface coverage is getting destabilized, and some adsorbed H_2O* desorb and form a first water layer between 2.65-4.00 Å, which can be seen in Figure 5.9a). The adsorbed water remains in a somehow almost flat, O-terminated configuration, and the water in the first water layer prefers to be in the two-H-down configuration at around 175 deg (see Figure 5.9f)) with a single peak in the hydrogen density (see Figure 5.9d)). Again, this can be explained by the repulsion between the negatively charged surface and the partially charged oxygen of the water. Nevertheless, it is important to mention that further investigations are needed to look into the role of surface coverage on the water structure and the ORR, including potential effects. Another limitation is the size of the unit cell; we use a 3×4 cell, which limits the possibilities of surface coverage structures immensely.

In summary, for the clean Au(111) and clean Pt(111), we find the first water layer dominating the water structure for all surface charge densities. On the clean Pt(111) surface, we observe H_2O* adsorption close to PZC. Surprisingly, as we go to more reducing conditions, the Pt(111) water structure resembles the Au(111) water structure: H_2O* adsorption becomes negligible, and the first water layer dominates. Lastly, adding surface coverage species to the Pt(111) leads to a tremendous change in the water structure: A dominant adsorbed water layer forms in xy-plane on the Pt(111) surface, where the H_2O* and OH* species are in vivid exchange of protons. Close to PZC, we find a vacuum region forming right above the adsorbate layer. Going to reducing conditions leads to some water desorption into this vacuum region, forming a first water layer.

Now we can also rationalize why the peroxo O_2* on Au(111) has substantially more H-bonds to the O_2* than the peroxo O_2* on the Pt(111) surfaces as seen in Figure 5.3. First of all, we characterize the position of the H-bond donating H_2O. In Figure 5.10, we can observe that the H-bonds donating H_2O sit in the first water layer within the 2.65 Å$< z <$4.00 Å range for all investigated metal surfaces.

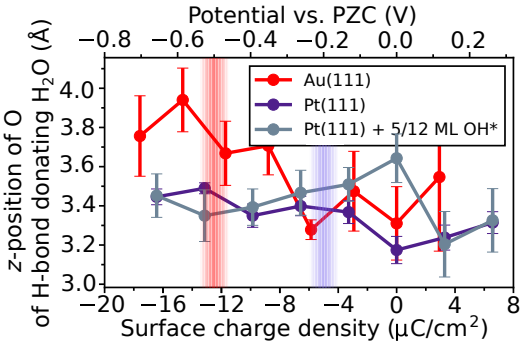

Figure 5.10: z-position of O of the H-bond donating H_2O above surface vs. surface charge density.

In the next step, we consider the water orientation of the first water layer: For the clean metal surfaces, we observe a flip of the interfacial water from a relatively unstructured O-down configuration at PZC to a more rigid one-H-down orientation under reducing conditions, as visible in the panels d) of Figures 5.7 and 5.8. The peak changes from a single broad peak to a double peak accompanied by a change of angle ϕ (angle between the water bisector and surface normal) towards 135 deg, going to reducing conditions (see panels f). For the OH*-covered Pt(111) system (Figure 5.9), we also observe a flip but towards a two-H-down water configuration in the first water layer characterized by a single H-density peak in panel d) and an angle ϕ=175 deg as seen in panel f). This might play a role in the substantial increase of H-bonds when going to reducing conditions on Au(111). Secondly, we will consider the position of the O_2*. On Au(111), the O_2* sits much further away from the surface and moves even further away when going to reducing conditions (Figure 5.4a)) as captured by the grey area in Figure 5.7. This, in combination with the re-oriented water, leads to the drastic increase of H-bonds to the O_2*. In contrast, on Pt(111), the O_2* is kept very close to the metal surface independent of the potential, restricting the number of possible H-bonds independent of the potential-induced change of water structure. This effect can also be captured by looking at the minimum O_2*-H(H_2O) distances as shown in Figure 5.11: On Au(111), when going to reducing conditions, the O_2*-H(H_2O) distance drops by ca. 0.4-0.5 Å while on Pt(111) we see a potential-independent O_2*-H(H_2O) distance at ca. 2.0 Å restricting the number of H-bonds possible to the O_2*.

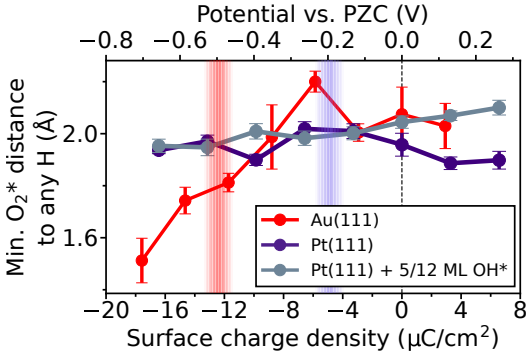

Figure 5.11: The average O_2*-H(H_2O) distance from AIMD simulations vs. surface charge density for Au(111) (red), Pt(111) (purple) and Pt(111) + 5/12 ML OH*. The dashed line depicts the PZC, while the red and purple areas indicate the experimental onset for Au(111) and Pt(111), respectively.

5.5 O_2* Dissociation at the Strong Binding Pt(111)

Up to this point, there was barely any potential dependence of the O_2* adsorption state visible on the strong binding Pt(111). Even when considering surface coverage species, the O_2 adsorption state appeared to be largely unaffected by changes in the interfacial water structure. Upon closer examination of our trajectories, we observe O_2* dissociation, which implies the promotion of the dissociative pathway and defines the selectivity towards H_2O. And once a more realistic OH* coverage is involved, an indirect effect of the potential on the next step of the ORR, the O_2* dissociation, becomes apparent. Only under highly reducing conditions, where the surface charge density is more than -13.1 µC/cm^2 can we observe trajectories exhibiting O_2* dissociation.

This is demonstrated in Figure 5.12, where we show the fraction of trajectories involving O_2* dissociation vs. the total number of trajectories for each surface charge density. We define the O_2* as dissociated once the intramolecular bond distance of O_2 is larger than 2.0 Å. For the clean Pt(111) surface, we detect O_2 dissociation in approximately $15 - 20$ % of the trajectories. However, when surface coverage species are added (+ 5/12 ML OH*), this changes drastically: We observe no dissociation near the PZC, with dissociation only occurring at more negative potentials ($\sigma <$ -13 µC/cm^2). It is important to note that these statistics are based on 14-16 trajectories, each with a length of $\approx$ 7.5 ps (excluding five ps equilibration time). For fully conclusive statistics, further investigation beyond the scope of this work is required. Nevertheless, our results indicate a clear trend: i) O_2* dissociation is favored over OOH* formation, and ii) this dissociation becomes somewhat more difficult near the PZC upon including more realistic surface coverages.

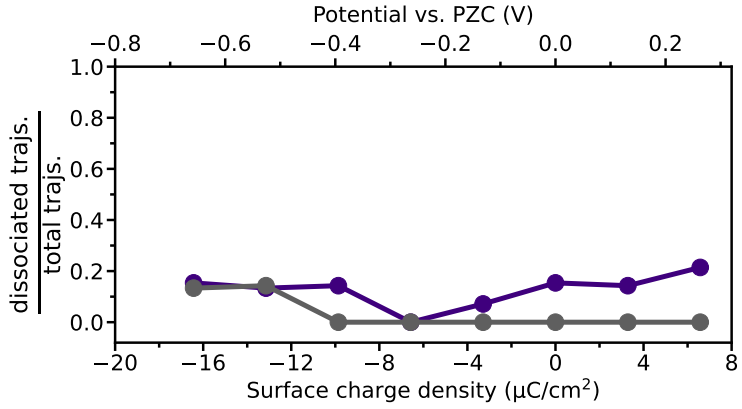

Figure 5.12: The probability of dissociation of the O_2* on the clean Pt(111) slab (purple) and on the OH*-covered Pt(111) slab (grey). The probability depicts how many trajectories show dissociated O_2* vs. the total number of trajectories per surface charge density.

This indirect effect of the potential on the O_2* dissociation can be explained with the potential dependent H_2O* adsorption: When going to reducing conditions relevant to experimental ORR operation, H_2O* is removed from the surface. This prediction aligns well with experimental observations that show a potential dependent preference for non-hydrated over hydrated OH* species on the surface during the ORR, as reported in Ref. [144].

Let's take a closer look at the surface coverage vs. the surface charge density: Figure 5.13a) shows the mean coverage per surface charge density for both Pt-based models. Firstly, the OH* coverage (empty markers) stays constant throughout the potential range: 0 ML and 5/12 = 0.42 ML, respectively. But once we look at the H_2O* population, we can see a potential dependent drop of the total OH*+H_2O* coverage (full markers). This picture does not change qualitatively when looking at the data without O_2* [2]. We suggest that fewer adsorbed H_2O* at reducing conditions lead to more available sites at the surface, which enables our AIMD simulations to capture O_2* dissociation.

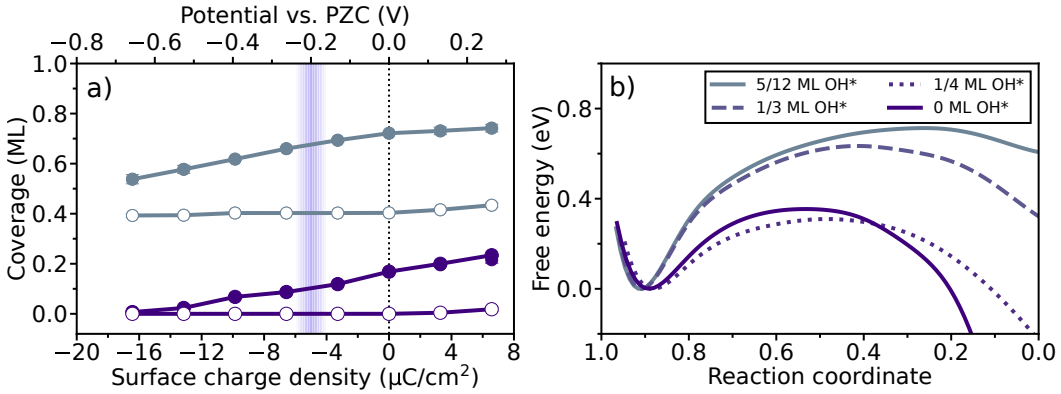

Figure 5.13: a) Total coverage (OH* and H_2O* on Pt(111) + O_2* (purple) and Pt(111) + 5/12 ML OH* + O_2* (grey) vs. surface charge density. The line with full markers shows the full H_2O* + OH* coverage, while the empty markers depict the OH* coverage. b) Free energy curves for O_2* dissociation for different amount of added OH* on Pt(111).

To gain further insight into the impact of the surface coverage on the O_2* dissociation, we have computed the free energy barrier calculations using AIMD-based umbrella sampling. These calculations were conducted by Elias Diesen; for in-depth technical information, see Ref. [2]. For simplicity, these simulations were performed at the PZC. Figure 5.12b) depicts the obtained free energy barrier for four distinct coverages of OH*: 0 ML, 1/4 ML, 1/3 ML, and 5/12 ML. The reaction coordinate describes the elongation of the O-O* bond while preventing protonation to OH*. The initial minimum observed on the left-hand side at approximately 0.9 in the reaction

coordinate represents the O_2* species, and going to the right-hand side, the distance between O-O* is widened, showing the change in free energy leading to the dissociated 2O* species. Overall, this reaction is exothermic. As previously hypothesized based on the AIMD results, the reaction exhibits a high barrier in the 5/12 ML OH* case. At the same time, it is significantly more facile in the low surface coverage (0-1/4 ML OH*) case. Notably, the reduction in the reaction barrier occurs relatively rapidly as the coverage decreases. In the low coverage regime, we observe a barrier of approximately 0.2-0.3 eV, which agrees with experimental studies in UHV [166, 167]. But once the coverage exceeds 1/3 ML OH*, we find a free energy barrier of 0.5-0.6 eV. Here, potential-driven desorption of H_2O* must free sufficient surface sites to allow O_2* dissociation within AIMD timescales. These findings are consistent with the statistics from the unbiased MD (Figure 5.12a)), where we observe a rather sudden onset of spontaneous dissociation once enough adsorbed H_2O* desorbs due to negative surface charge. The overall coverage of H_2O*/OH* seems to act as a rather sensitive switch, which determines whether O_2* can dissociate. Nevertheless, it is rather difficult to define the exact coverage cut-off due to the co-existence of adsorbed OH* and H_2O* species as we found an increase of adsorbed H_2O* with increasing OH*.

Now we can take a more in-depth look at the process of dissociation from AIMD simulations: We do not observe protonation of the adsorbed O_2*, but protonation occurs after O_2* dissociation. In Figure 5.14, we have selected all trajectories in which dissociation occurs after the equilibration time and compared the dissociation process with the subsequent hydrogenation. The dissociation of O_2* is set to occur at timestep 50 fs, and we have displayed the 50 previous images and the next 450 images to observe the dissociation process in this chosen 500 fs time window. Figure 5.14a) and Figure 5.14c) illustrate the O-O* distance for the clean Pt(111) and OH*-covered Pt(111) slab, respectively. These figures show how the O_2* dissociation is irreversible, as the O_2* does not re-associate afterward. The minimum distance between the original molecular O_2 atoms and any hydrogen can be used to track protonation events. Figure 5.14b) and Figure 5.14d) show the minimum OO-HOH distance with respect to the O_2* dissociation indicated by the vertical line. We have also considered OH* as a potential proton donor, but we only observe adsorbed H_2O* as a proton donor to protonate the oxygen species. Once the OO-HOH distance is below 1.2 Å, the O* species is considered protonated. Again, the protonation is an irreversible process in our simulations. Additionally, when we compare the timing of the O_2* dissociation (indicated by the vertical line) with the timing of protonation, it becomes clear that O_2* dissociation occurs first. Only one trajectory (purple) in Figure 5.14b) shows simultaneous dissociation and hydrogenation of O_2*. All other hydrogenation processes commence around 50 fs after dissociation. Nevertheless, since we work on

the fs-timescale, these dynamics are on the electronic timescale. So, it isn't fully clear to what extent the O_2* dissociation is decoupled from the protonation.

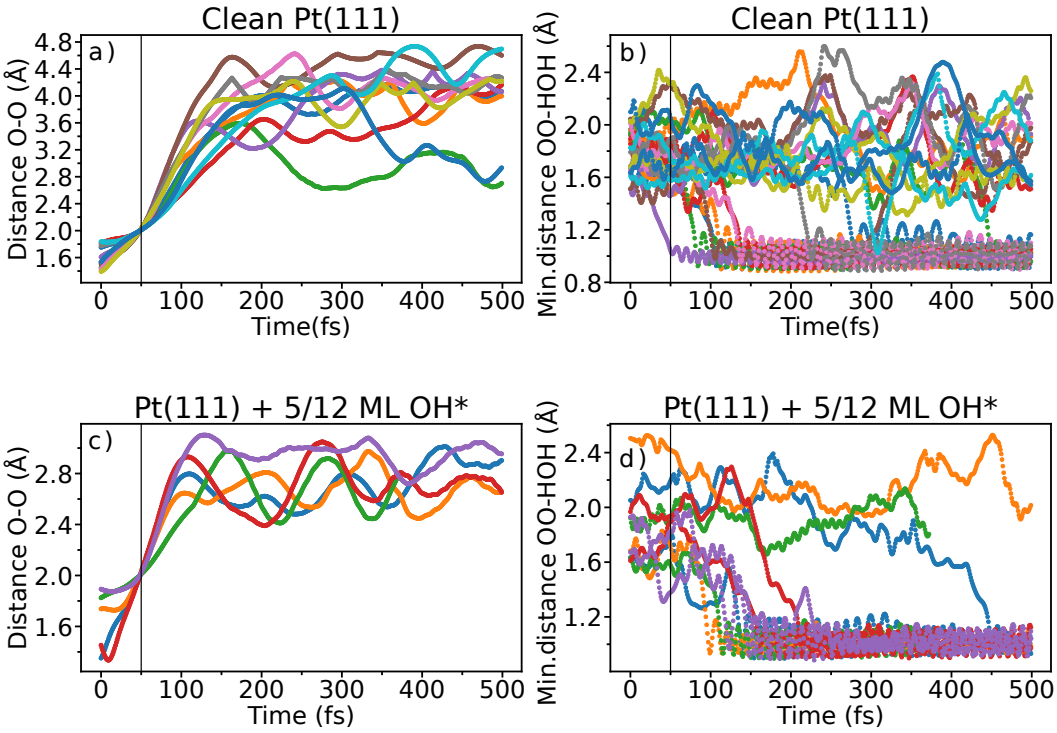

Figure 5.14: a) O-O* distance and b) minimum distance OO-HOH vs. timestep for the clean Pt(111) slab. c) and d) for the Pt(111) with 5/12 ML OH* coverage. Each line color represents one trajectory. Only trajectories where O_2* dissociation occurs after the equilibration time are chosen and the O_2* dissociation is set to occur at timestep = 50 fs for easy representation and comparison. The vertical line depicts the O_2* dissociation.

Lastly, we can plot the oxygen species' adsorption energies to understand the thermodynamics behind the O_2* dissociation and consecutive protonation steps. We resolve our trajectories to give us the O_2* adsorption energy for the different oxygen species present: O_2*, O*+O*, O*+OH*, and lastly, fully protonated OH*+OH* as seen in Figure 5.15. The O_2* dissociation and each consecutive protonation step are exothermic.

In summary, we observe the O_2* dissociation as the next step of the ORR and no occurrence of OOH*. This result implies promotion of the dissociative pathway and could also explain the selectivity on Pt(111): Since the O_2* dissociates, the pathway towards H_2O_2 is also permanently closed and H_2O always forms as a product, which is in agreement with experiments [139]. Additionally, we find an indirect effect of the

potential on the next step of the ORR: Close to PZC, the O_2* dissociation is blocked when more realistic surface coverages are included. Going to reducing conditions leads to H_2O* desorption, which in turn enables O_2* dissociation, implying that O_2* dissociation might be promoted at reducing conditions.

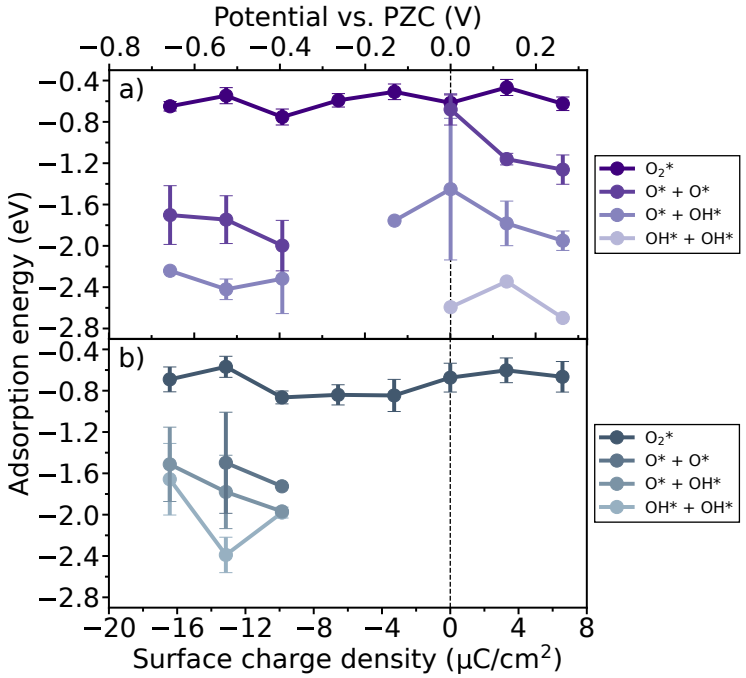

Figure 5.15: O_2* adsorption energy vs. surface charge density for a) the clean Pt(111) and b) the OH*-covered Pt(111) slab. The trajectory is resolved by oxygen species: Going from dark to light, we see the adsorption energies of O_2*, O*+O*, O*+OH*, and lastly, fully protonated OH*+OH*.

5.6 Summary

In this chapter, we compare the O_2* adsorption on the strong binding Pt(111) vs. the weak binding Au(111). With the help of AIMD simulations, we examine the initial step of the ORR under realistic conditions, including explicit water, charge effects, and co-adsorption.

We demonstrate that the O_2* adsorption behaves notably differently under potential on Pt(111) vs. Au(111): The strong potential dependence of the O_2* adsorption free energy is lost on the strong binding Pt(111). We explain this with the different reactivity of the two metal surfaces. As explained in Chapter 4, on Au(111), we observe a strong potential dependence, driving the transition from a preferred physisorbed state towards a superoxo and eventually peroxo O_2* adsorbed on the surface. We find a strong dipole-field effect stabilizing the O_2*, dominant close to

PZC. At more reducing potentials, close to the experimental ORR onset, we observe that the O_2* adsorption becomes favorable. A secondary stabilization from the increase of H-bonding during the transition from superoxo- to peroxo- O_2* leads to an even stronger response of the O_2* to the potential. We propose the O_2* adsorption as the rate-determining step since the O_2* adsorption becomes favorable close to experimental onset potentials as well as it can also explain the SHE-driven reaction onset [155] (see Chapter 4).

In contrast, on Pt(111), the situation is noticeably different. The adsorption of O_2 is thermodynamically favorable across the studied potential range. The reactive Pt(111) surface anchors the O_2* close to the surface, limiting electrostatic dipole-field effects and H-bonding from the solvent, leading to the negligible potential dependence of the O_2*. The O_2* state is characterized by a peroxo species with a relatively constant number of H-bonds sitting in the bridge position, irrespective of the potential.

It is known that OH* coverage plays a major role at the strong binding Pt(111) surface [144, 153]. We conduct AIMD simulations with a more realistic coverage of 5/12 ML OH* [154]. When going from the clean slab to the OH*-covered Pt(111) we observe a significant change in interfacial water structure: The first water layer is depleted and water adsorption is induced. We observe a stiff surface cover forming in the *xy*-plane of H_2O*+OH* species that dynamically interexchange protons throughout the simulation. For all investigated surfaces, when going to reducing conditions, we observe water desorption and the water in the first water layer flips from O-down water to H-down configuration. Surprisingly, the O_2* adsorption itself is barely affected by this change of interfacial water structure and remains independent from potential.

Moreover, our simulations allow us to look at the next step of the ORR: We observe O_2* dissociation and consecutive protonation of the newly formed O* species. We do not observe any formation of OOH* implying a promoted dissociative pathway of the ORR on Pt(111). This can also explain the experimental selectivity towards H_2O on Pt(111): After irreversible O_2* dissociation, the peroxide formation becomes fully inhibited. Interestingly, we find an indirect effect of the potential on the O_2* dissociation: Realistic coverage of OH* and H_2O* inhibits O_2* dissociation close to PZC, suggesting that the dissociation rate of O_2* is potential dependent. Going to reducing conditions H_2O* desorbs, promoting O_2* dissociation, which is in agreement with experimental findings [144]. Again, we find potential dependence on a step that seems decoupled from a proton transfer. The O_2 dissociation is unlikely to be the rate-limiting step on Pt(111), but this finding proves again that the electric field effect cannot be neglected.

To conclude, our work shows how potential effects can vary depending on the reactivity of the metal surface: On the weak binding Au(111), we find strong potential dependence of the O_2 adsorption, while on the strong binding Pt(111), we find very weak potential dependence of the O_2 adsorption, independent of surface coverage. However, we shed light on the indirect influence of potential through surface coverage species that can influence the next step we observe of the ORR: The O_2* dissociation. Although we do not determine this step as rate-determining, it can very well be the selectivity-determining step closing the possibility to form peroxide.

Chapter 6

Conclusion

One of the most significant challenges facing modern society today is the need to mitigate climate change by developing sustainable energy solutions. Fuel cells represent a promising technology for clean energy generation. However, the efficiency is limited by the Oxygen Reduction Reaction (ORR) that takes place at the cathode. This thesis aims at understanding the first step of the ORR: the O_2 adsorption and its role in the ORR on Au(111) and Pt(111) surfaces while providing fundamental and methodological insights that are crucial for understanding the processes at the highly complex electrochemical metal/water interfaces as found in fuel cell technologies.

Nowadays, first-principles simulations of electrochemical processes have made a significant contribution to our current understanding of heterogeneous electrocatalysis. Commonly, electrochemical reactions are depicted by proton-coupled electron transfers (PCET). Therefore, non-PCET steps, like, e.g., the O_2 adsorption, have often been neglected as "chemical steps" independent from potential. Secondly, previous literature often conducts calculations in a charge-neutral environment. Consequently, capacitive charging at the interface is often neglected and overlooked when investigating the mechanism of the ORR. At first, we therefore investigate the effect of the potential on the O_2 adsorption on the weak binding Au(111) from a computational modeling perspective. We evaluate three distinct modeling techniques: The saw-tooth potential in vacuum, implicit solvation, and AIMD simulations. Our results demonstrate the importance of including local electric field effects in models of the electrochemical interface. We find that neglecting explicit water and surface coverage gives an incomplete picture that can lead to fundamental mechanistic misconceptions. We conclude that the required level of detail can be achieved by AIMD simulations.

On the weak-binding Au(111) surface, we demonstrate that O_2 adsorption is highly potential dependent. The O_2 adsorption becomes favorable when going to reducing conditions, close to realistic ORR onset potential. The findings suggest that O_2 adsorption is an electrochemical step rather than a purely chemical one, potentially also serving as the rate-determining step in the ORR. O_2* adsorption as the rate-determining step can also explain the experimental SHE-driven activity [125,

155]. The stabilization of the O_2 adsorption is driven by two major effects: i) The dipole-field interactions and ii) H-bonding from the explicit water. The adsorbed O_2* on Au(111) shows a rather large dipole moment leading to substantial stabilization throughout the studied potential range. When going to more reducing conditions, close to ORR onset we observe a switch from the superoxo to the peroxo O_2* species, which leads to an increase in H-bonds to the adsorbed O_2*. Our findings thus underscore the importance of accounting for field and explicit water effects in computational models of the ORR. Our investigations on the weak binding Au(111) exemplify the critical role of potential in modulating O_2 adsorption, a non-PCET step. The study we conducted on the Au(111) suggests that weak-binding catalysts may benefit from strategies that stabilize the O_2 intermediate, potentially through the tweaking with the catalyst material or the addition of co-catalysts.

In contrast, we find weak potential dependence of the O_2 adsorption on the strong-binding Pt(111) surface, O_2 adsorption remains thermodynamically favorable across the studied potential range. This can be explained through the difference in reactivity. On the strong binding Pt(111), the adsorbed O_2* sits much closer to the metal catalyst, leading to a much smaller dipole moment and response to the field. The adsorbed O_2* is in the peroxo configuration and displays a rather constant stabilization from H-bonds throughout the studied potential range independent of changes in water structure and surface coverages. We observe O_2* dissociation and no OOH* formation, indicating a prominent dissociative pathway for the ORR on Pt(111). Furthermore, O_2* dissociation determines the selectivity towards H_2O as the sole product on Pt(111), which is in agreement with experimental results [139]. We find that the interfacial water structure on Pt(111) undergoes significant changes with the inclusion of more realistic surface coverages [144, 153, 154] and displays sensitive changes to the applied potential. This leads to an indirect effect of the potential on the ORR mechanism, particularly on the O_2* dissociation step. At reducing potentials, H_2O* desorbs promoting O_2* dissociation. It highlights how the potential can indirectly affect a non-PCET step, here the O_2* dissociation, through changes in surface coverage and water structure. This suggests that it is important to include potential effects on the interfacial water structure to get a complete picture of capacitive charging and its possible consequences for the ORR reaction mechanism. This way, one might find interesting routes, via control of the local fields [150, 151] or via controlling interfacial water structure to enhance catalytic performance.

Despite these advances, this study is subject to several limitations. The computational models, while robust, are constrained by the approximations inherent in AIMD simulations. AIMD simulations are very costly; the timescales and unit cell size remain very limited, so the full complexity of real-world electrochemical inter-

faces cannot be captured. Additionally, it is important to consider that our approach is a constant-charge approach. We only approximate the potential from our applied charges.

Future research should aim to extend the current work by exploring longer simulation timescales and larger system sizes to capture more complex dynamics. Development of more advanced and cheap computational methods, e.g., machine-learning potentials, are essential to go beyond picoseconds timescale and bigger, more realistic unit cells while still including quantum effects. Additionally, investigating the next steps of the ORR and including kinetics can provide broader insights into the ORR and complement the trends already observed in this work. Furthermore, including additional catalyst surfaces, differing surface coverages, and cationic species in solution can give an even more realistic view of the ORR.

In conclusion, this thesis contributes significant new insights into the ORR mechanisms on Au(111) and Pt(111), emphasizing the importance of going beyond proton-coupled-electron transfers in a charge-neutral picture. We shed light on how potential effects, explicit water, and coverage effects influence the O_2* adsorption and consecutive step of the ORR. We find that the potential dependent O_2 adsorption on Au(111) can be rate-determining. At the same time, on Pt(111), we observe O_2* dissociation that can determine the selectivity towards H_2O. At reducing conditions, we observe the promotion of the O_2* dissociation through the potential dependent desorption of surface species. These findings not only uncover some of the mysteries surrounding ORR but can inspire similar studies for a broader range of electrochemical reactions, e.g. the hydrogen evolution reaction and the carbon dioxide reduction reaction. Answering the need for a better understanding of the mechanisms at the complex electrochemical interface can help the development of better catalysts, hopefully mitigating the limitations currently present in fuel cell technologies.

Bibliography

(1) Dudzinski, A. M.; Diesen, E.; Heenen, H. H.; Bukas, V. J.; Reuter, K. First Step of the Oxygen Reduction Reaction on Au(111): A Computational Study of O_2 Adsorption at the Electrified Metal/Water Interface. *ACS Catal.* **2023**, *13*, 12074–12081.

(2) Dudzinski, A. M.; Diesen, E.; Reuter, K.; Bukas, V. J. Oxygen Adsorption at the Electrochemical Metal/Water Interface: Au(111) vs Pt(111). *ChemRxiv* **2024**.

(3) Diesen, E.; Dudzinski, A. M.; Reuter, K.; Bukas, V. J. On the Origin of Electrocatalytic Selectivity during the Oxygen Reduction Reaction on Au(111). *ChemRxiv* **2024**.

(4) Kresse, G.; Hafner, J. Ab initio molecular dynamics for liquid metals. *Phys. Rev. B* **1993**, *47*, 558–561.

(5) Kresse, G.; Furthmüller, J. Efficiency of ab-initio total energy calculations for metals and semiconductors using a plane-wave basis set. *Comput. Mater. Sci.* **1996**, *6*, 15–50.

(6) Kresse, G.; Furthmüller, J. Efficient iterative schemes for ab initio total-energy calculations using a plane-wave basis set. *Phys. Rev. B* **1996**, *54*, 11169–11186.

(7) Nørskov, J. K.; Studt, F.; Abild-Pedersen, F.; Bligaard, T., *Fundamental Concepts in Heterogeneous Catalysis*, 1st; John Wiley & Sons, Inc.: 2014.

(8) Kulkarni, A.; Siahrostami, S.; Patel, A.; Nørskov, J. K. Understanding Catalytic Activity Trends in the Oxygen Reduction Reaction. *Chem. Rev.* **2018**, *118*, 2302–2312.

(9) Seh, Z. W.; Kibsgaard, J.; Dickens, C. F.; Chorkendorff, I.; Nørskov, J. K.; Jaramillo, T. F. Combining Theory and Experiment in Electrocatalysis: Insights into Materials Design. *Science* **2017**, *355*.

(10) Yoshida, T.; Kojima, K. Toyota MIRAI Fuel Cell Vehicle and Progress Toward a Future Hydrogen Society. *Interface* **2015**, *24*, 45–49.

(11) Tripkovic, V.; Vegge, T. Potential- and Rate-Determining Step for Oxygen Reduction on Pt(111). *J. Phys. Chem. C* **2017**, *121*, 26785–26793.

(12) Jaganmohan, M. Global platinum mine production 2010-2023, `https://www.statista.com/statistics/1170691/mine-production-of-platinum-worldwide/`, accessed 19 April, 2024, 2024.

(13) Stephens, I. E. L.; Bondarenko, A. S.; Grønbjerg, U.; Rossmeisl, J.; Chorkendorff, I. Understanding the electrocatalysis of oxygen reduction on platinum and its alloys. *Energy Environ. Sci.* **2012**, *5*.

(14) Debe, M. K. Electrocatalyst Approaches and Challenges for Automotive Fuel Cells. *Nature* **2012**, *486*, 43–51.

(15) Gasteiger, H. A.; Marković, N. M. Just a Dream or Future Reality? *Science* **2009**, *324*, 48–49.

(16) Gasteiger, H. A.; Kocha, S. S.; Sompalli, B.; Wagner, F. T. Activity Benchmarks and Requirements for Pt, Pt-Alloy, and Non-Pt Oxygen Reduction Catalysts for PEMFCs. *Appl. Catal., B* **2005**, *56*, 9–35.

(17) Kodama, K.; Nagai, T.; Kuwaki, A.; Jinnouchi, R.; Morimoto, Y. Challenges in applying highly active Pt-based nanostructured catalysts for oxygen reduction reactions to fuel cell vehicles. *Nat. Nanotechnol.* **2021**, *16*, 140–147.

(18) Bondarenko, A. S.; Stephens, I. E. L.; Hansen, H. A.; Pérez-Alonso, F. J.; Tripkovic, V.; Johansson, T. P.; Rossmeisl, J.; Nørskov, J. K.; Chorkendorff, I. The Pt(111)/Electrolyte Interface under Oxygen Reduction Reaction Conditions: An Electrochemical Impedance Spectroscopy Study. *Langmuir* **2011**, *27*, 2058–2066.

(19) Gewirth, A. A.; Thorum, M. S. Electrochemical Applications of Porous Inorganic Materials. *Inorg. Chem.* **2010**, *49*, 3557–3566.

(20) Allen, M. P.; Tildesley, D. J., *Computer Simulation of Liquids*; Oxford University Press: 2017.

(21) Jensen, F., *Introduction to Computational Chemistry*, 3rd; Wiley: Chichester, 2017.

(22) Frenkel, D.; Smit, B. In *Understanding Molecular Simulation*, Frenkel, D., Smit, B., Eds., Second Edition; Academic Press: San Diego, 2002, pp 63–107.

(23) Sabatier, P. Hydrogenations et Déshydrogénations par Catalyse. *Ber. Dtsch. Chem. Ges.* **1911**, *44*, 1984.

(24) Nørskov, J. K.; Rossmeisl, J.; Logadottir, A.; Lindqvist, L.; Kitchin, J. R.; Bligaard, T.; Jónsson, H. Origin of the Overpotential for Oxygen Reduction at a Fuel-Cell Cathode. *J. Phys. Chem. B* **2004**, *108*, 17886–17892.

(25) Nørskov, J. K.; Bligaard, T.; Hvolbæk, B.; Abild-Pedersen, F.; Chorkendorff, I.; Christensen, C. H. The nature of the active site in heterogeneous metal catalysis. *Chem. Soc. Rev.* **2008**, *37*, 2163–2171.

(26) Ringe, S.; Morales-Guio, C. G.; Chen, L. D.; Fields, M.; Jaramillo, T. F.; Hahn, C.; Chan, K. Double layer charging driven carbon dioxide adsorption limits the rate of electrochemical carbon dioxide reduction on Gold. *Nat. Commun.* **2020**, *11*, 33.

(27) Vijay, S.; Gauthier, J. A.; Heenen, H. H.; Bukas, V. J.; Kristoffersen, H. H.; Chan, K. Dipole-Field Interactions Determine the CO2 Reduction Activity of 2D Fe–N–C Single-Atom Catalysts. *ACS Catal.* **2020**, *10*, 7826–7835.

(28) Montoya, J. H.; Shi, C.; Chan, K.; Nørskov, J. K. Theoretical Insights into a CO Dimerization Mechanism in CO2 Electroreduction. *J. Phys. Chem. Lett.* **2015**, *6*, 2032–2037.

(29) Liu, X.; Schlexer, P.; Xiao, J.; Ji, Y.; Wang, L.; Sandberg, R. B.; Tang, M.; Brown, K. S.; Peng, H.; Ringe, S.; Hahn, C.; Jaramillo, T. F.; Nørskov, J. K.; Chan, K. pH effects on the electrochemical reduction of CO(2) towards C2 products on stepped copper. *Nat. Comm.* **2019**, *10*, 32.

(30) Kristoffersen, H. H.; Chan, K. Towards constant potential modeling of CO-CO coupling at liquid water-Cu(100) interfaces. *J. Catal.* **2021**, *396*, 251–260.

(31) Seh, Z. W.; Kibsgaard, J.; Dickens, C. F.; Chorkendorff, I.; Nørskov, J. K.; Jaramillo, T. F. Combining theory and experiment in electrocatalysis: Insights into materials design. *Science* **2017**, *355*, eaad4998.

(32) Hori, Y., *Modern Aspects of Electrochemistry*; Springer: New York, 2008, pp 39–138.

(33) Koper, M. T. M. Theory of multiple proton–electron transfer reactions and its implications for electrocatalysis. *Chem. Sci.* **2013**, *4*, 2710–2723.

(34) Bukas, V. J.; Kim, H. W.; Sengpiel, R.; Knudsen, K.; Voss, J.; McCloskey, B. D.; Luntz, A. C. Combining Experiment and Theory To Unravel the Mechanism of Two-Electron Oxygen Reduction at a Selective and Active Co-catalyst. *ACS Catal.* **2018**, *8*, 11940–11951.

(35) Nitopi, S.; Bertheussen, E.; Scott, S. B.; Liu, X.; Engstfeld, A. K.; Horch, S.; Seger, B.; Stephens, I. E. L.; Chan, K.; Hahn, C.; Nørskov, J. K.; Jaramillo, T. F.; Chorkendorff, I. Progress and Perspectives of Electrochemical CO_2 Reduction on Copper in Aqueous Electrolyte. *Chem. Rev.* **2019**, *119*, 7610–7672.

(36) Cramer, C. J., *Essentials of Computational Chemsitry Theories and Models*, 2nd ed.; John Wiley & Sons, Ltd: 2004.

(37) Engel, E.; Dreizler, R., *Density Functional Theory: An Advanced Course*; Theoretical and Mathematical Physics; Springer Berlin Heidelberg: 2011.

(38) Heid, R. Electron-Phonon Coupling. *Autumn school on correlated electrons* **2017**.

(39) Montemore, M. M.; van Spronsen, M. A.; Madix, R. J.; Friend, C. M. O_2 Activation by Metal Surfaces: Implications for Bonding and Reactivity on Heterogeneous Catalysts. *Chem. Rev.* **2018**, *118*, 2816–2862.

(40) Hohenberg, P.; Kohn, W. Inhomogeneous Electron Gas. *Phys. Rev.* **1964**, *136*, B864–B871.

(41) Sahni, V. In *Quantal Density Functional Theory*; Springer Berlin Heidelberg: Berlin, Heidelberg, 2004, pp 99–123.

(42) Hafner, J. Ab-initio simulations of materials using VASP: Density-functional theory and beyond. *J. Comput. Chem.* **2008**, *29*, Special Issue: Computational Solid State Chemistry, 2044–2078.

(43) Salami, N.; Shokri, A. In *Photocatalysis: Fundamental Processes and Applications*, Ghaedi, M., Ed.; Interface Science and Technology, Vol. 32; Elsevier: 2021, pp 325–373.

(44) Pueyo, A. G.; Marques, M. A. L.; Rubio, A.; Castro, A. Propagators for the Time-Dependent Kohn–Sham Equations: Multistep, Runge–Kutta, Exponential Runge–Kutta, and Commutator Free Magnus Methods. *Journal of Chemical Theory and Computation* **2018**, *14*, 3040–3052.

(45) Dudzinski, A. Theoretical Investigation of Novel Binary Nitrides M_2N_3 (M=Ta, Nb, V) as New High-Pressure Superconductors, Master's thesis, Université Grenoble Alpes and Université de Liège, 2020.

(46) Blöchl, P. E. Projector augmented-wave method. *Phys. Rev. B* **1994**, *50*, 17953–17979.

(47) Vanderbilt, D. Soft self-consistent pseudopotentials in a generalized eigenvalue formalism. *Phys. Rev. B* **1990**, *41*, 7892–7895.

(48) Kresse, G.; Hafner, J. Norm-conserving and ultrasoft pseudopotentials for first-row and transition elements. *J. Condens. Matter Phys.* **1994**, *6*, 8245.

(49) Andersen, O. K. Linear methods in band theory. *Phys. Rev. B* **1975**, *12*, 3060–3083.

(50) Kresse, G.; Joubert, D. From ultrasoft pseudopotentials to the projector augmented-wave method. *Phys. Rev. B* **1999**, *59*, 1758–1775.

(51) VASP manual, Projector-augmented-wave formalism. Accessed: 2024-10-16, `https://www.vasp.at/wiki/index.php/Projector-augmented-wave_formalism`.

(52) Baerends, E.; Ellis, D.; Ros, P. Self-consistent molecular Hartree—Fock—Slater calculations I. The computational procedure. *Chem. Phys.* **1973**, *2*, 41–51.

(53) Pettersson, L.; Wahlgren, U. An investigation of basis sets and basis set superposition error in transition metals using frozen core and frozen orbital techniques. *Chem. Phys.* **1982**, *69*, 185–192.

(54) Matsuoka, O. A frozen-core approximation using reduced core-basis functions. *J. Chem. Phys.* **1992**, *96*, 6773–6777.

(55) Voss, J. XC Functionals in Density Functional Theory. Accessed: 20-Oct-2024, `https://stanford.edu/~vossj/slac/project/xc-functionals/`.

(56) Perdew, J. P.; Schmidt, K. Jacob's ladder of density funcitonal approximations for the exchange-correlation energy. *AIP Conf. Proc.* **2001**, *577*, 1–20.

(57) Perdew, J. P.; Wang, Y. Accurate and Simple Analytic Representation of the Electron-Gas Correlation Energy. *Phys. Rev. B* **1992**, *45*, 13244.

(58) Perdew, J. P.; Burke, K.; Ernzerhof, M. Generalized Gradient Approximation Made Simple. *Phys. Rev. Lett.* **1996**, *77*, 3865–3868.

(59) Hammer, B.; Hansen, L. B.; Nørskov, J. K. Improved adsorption energetics within density-functional theory using revised Perdew-Burke-Ernzerhof functionals. *Phys. Rev. B* **1999**, *59*, 7413–7421.

(60) Wellendorff, J.; Silbaugh, T. L.; Garcia-Pintos, D.; Nørskov, J. K.; Bligaard, T.; Studt, F.; Campbell, C. T. A Benchmark Database for Adsorption Bond Energies to Transition Metal Surfaces and Comparison to Selected DFT Functionals. *Surf. Sci.* **2015**, *640*, 36–44.

(61) Wellendorff, J.; Lundgaard, K. T.; Møgelhøj, A.; Petzold, V.; Landis, D. D.; Nørskov, J. K.; Bligaard, T.; Jacobsen, K. W. Density Functionals for Surface Science: Exchange-Correlation Model Development with Bayesian Error Estimation. *Phys. Rev. B: Condens. Matter Mater. Phys.* **2012**, *85*, 235149.

(62) Tao, J.; Perdew, J. P.; Staroverov, V. N.; Scuseria, G. E. Climbing the density functional ladder: Nonempirical meta-generalized gradient approximation designed for molecules and solids. *Phys. Rev. Lett.* **2003**, *91*, 146401.

(63) Perdew, J. P. Generalized gradient approximations for exchange and correlation: A look backward and forward. *Phys. B: Condens. Matter* **1991**, *172*, 1–6.

(64) Grimme, S.; Antony, J.; Ehrlich, S.; Krieg, H. A consistent and accurate ab initio parametrization of density functional dispersion correction (DFT-D) for the 94 elements H-Pu. *J. Chem. Phys.* **2010**, *132*, 154104.

(65) Grimme, S. Density functional theory with London dispersion corrections. *Wiley Interdiscip. Rev. Comput. Mol. Sci.* **2011**, *1*, 211–228.

(66) VASP manual, KPOINTS. Accessed: 2024-10-16, `https://www.vasp.at/wiki/index.php/KPOINTS`.

(67) Monkhorst, H. J.; Pack, J. D. Special points for Brillouin-zone integrations. *Phys. Rev. B* **1976**, *13*, 5188–5192.

(68) QuantumATK Manual, Occupation Methods. Accessed: 2024-10-16, `https://docs.quantumatk.com/manual/technicalnotes/occupation_methods/occupation_methods.html#background`.

(69) Martin, R. M., *Electronic Structure: Basic Theory and Practical Methods*; Cambridge University Press: 2004.

(70) Onishi, T., *Quantum Computational Chemistry: Modelling and Calculation for Functional Materials*, 1st ed.; Springer Nature Singapore: 2018.

(71) Marx, D.; Hutter, J. In *Modern Methods and Algorithms of Quantum Chemistry*, Grotendorst, J., Ed.; NIC Series, Vol. 1; John von Neumann Institute for Computing: Jülich, 2000, pp 301–449.

(72) Iftimie, R.; Minary, P.; Tuckerman, M. E. Ab Initio Molecular Dynamics: Concepts, Recent Developments, and Future Trends. *Proc. Natl. Acad. Sci. U.S.A.* **2005**, *102*, 6654–6659.

(73) Kutzelnigg, W. The adiabatic approximation I. The physical background of the Born-Handy ansatz. *Mol. Phys.* **1997**, *90*, 909–916.

(74) Paquet, E.; Viktor, H. L. Computational Methods for Ab Initio Molecular Dynamics. *Advances in Chemistry* **2018**, *2018*, Article ID 9839641.

(75) Verlet, L. Computer "Experiments" on Classical Fluids. I. Thermodynamical Properties of Lennard-Jones Molecules. *Phys. Rev.* **1967**, *159*, 98–103.

(76) Nosé, S. A molecular dynamics method for simulations in the canonical ensemble. *Mol. Phys.* **1984**, *52*, 255–268.

(77) Nosé, S. A unified formulation of the constant temperature molecular dynamics methods. *J. Chem. Phys.* **1984**, *81*, 511–519.

(78) Hoover, W. G. Canonical dynamics: Equilibrium phase-space distributions. *Phys. Rev. A* **1985**, *31*, 1695.

(79) Hoover, W. G. Constant-pressure equations of motion. *Phys. Rev. A* **1986**, *34*, 2499.

(80) Hoover, W. G. Nosé–Hoover nonequilibrium dynamics and statistical mechanics. *Mol. Simul.* **2007**, *33*, 13–19.

(81) Hünenberger, P. H. In *Advanced Computer Simulation: Approaches for Soft Matter Sciences I*, Dr. Holm, C., Prof. Dr. Kremer, K., Eds.; Springer Berlin Heidelberg: Berlin, Heidelberg, 2005, pp 105–149.

(82) Heenen, H. H.; Gauthier, J. A.; Kristoffersen, H. H.; Ludwig, T.; Chan, K. Solvation at metal/water interfaces: An ab initio molecular dynamics benchmark of common computational approaches. *J. Chem. Phys.* **2020**, *152*, 144703-1 - 144703–11.

(83) Sakong, S.; Groß, A. The electric double layer at metal-water interfaces revisited based on a charge polarization scheme. *J. Chem. Phys.* **2018**, *149*, 084705.

(84) Morawietz, T.; Singraber, A.; Dellago, C.; Behler, J. How van der Waals interactions determine the unique properties of water. *Proc. Natl. Acad. Sci.* **2016**, *113*, 8368–8373.

(85) Bengtsson, L. Dipole correction for surface supercell calculations. *Phys. Rev. B* **1999**, *59*, 12301–12304.

(86) VASP Manual, Structure Optimization Accessed: 20-Oct-2024, `https://www.vasp.at/wiki/index.php/Structure_optimization`.

(87) Press, W. H.; Flannery, B. P.; Teukolsky, S. A.; Vetterling, W. T., *Numerical Recipes*; Cambridge University Press, New York: 1986.

(88) Neugebauer, J.; Scheffler, M. Adsorbate-substrate and adsorbate-adsorbate interactions of Na and K adlayers on Al(111). *Phys. Rev. B* **1992**, *46*, 16067–16080.

(89) Otani, M.; Sugino, O. First-principles calculations of charged surfaces and interfaces: A plane-wave nonrepeated slab approach. *Phys. Rev. B* **2006**, *73*, 115407.

(90) Cramer, C. J.; Truhlar, D. G. Implicit solvation models: equilibria, structure, spectra, and dynamics. *Chemi. Rev.* **1999**, *99*, 2161–2200.

(91) Kelly, S. R.; Kirk, C.; Chan, K.; Nørskov, J. K. Electric Field Effects in Oxygen Reduction Kinetics: Rationalizing pH Dependence at the Pt(111), Au(111), and Au(100) Electrodes. *J. Phys. Chem. C* **2020**, *124*, 14581–14591.

(92) Fumagalli, L.; Esfandiar, A.; Fabregas, R.; Hu, S.; Ares, P.; Janardanan, A.; Yang, Q.; Radha, B.; Taniguchi, T.; Watanabe, K.; Gomila, G.; Novoselov, K.; Geim, A. Anomalously low dielectric constant of confined water. *Science* **2018**, *360*, 1339–1342.

(93) Deißenbeck, F.; Freysoldt, C.; Todorova, M.; Neugebauer, J.; Wippermann, S. Dielectric Properties of Nanoconfined Water: A Canonical Thermopotentiostat Approach. *Phys. Rev. Lett.* **2021**, *126*, 136803.

(94) Trasatti, S.; Lust, E., *Modern Aspects of Electrochemistry*; Springer: 1999; Chapter Chapter 1, pp 1–215.

(95) Kofman, R.; Garrigos, R.; Cheyssac, P. Optical response of a charged metal-aqueous electrolyte interphase. *Thin Solid Films* **1981**, *82*, 73–80.

(96) Kolb, D.; Schneider, J. Surface reconstruction in electrochemistry: Au(100-(5 × 20), Au(111)-(1 × 23) and Au(110)-(1 × 2). *Electrochim. Acta* **1986**, *31*, 929–936.

(97) Ojha, K.; Arulmozhi, N.; Aranzales, D.; Koper, M. T. M. Double Layer at the Pt(111)–Aqueous Electrolyte Interface: Potential of Zero Charge and Anomalous Gouy–Chapman Screening. *Angew. Chem., Int. Ed.* **2020**, *59*, 711–715.

(98) Bohnen, K. P.; Kolb, D. Charge-versus adsorbate-induced lifting of the Au (100)-(hex) reconstruction in an electrochemical environment. *Surf. Sci.* **1998**, *407*, L629–L632.

(99) Domínguez-Flores, F.; Melander, M. M. Approximating constant potential DFT with canonical DFT and electrostatic corrections. *J. Chem. Phys.* **2023**, *158*.

(100) Mathew, K.; Kolluru, V. S. C.; Hennig, R. G. VASPsol: Implicit solvation and electrolyte model for density-functional theory, `https://github.com/henniggroup/VASPsol`, 2018.

(101) Mathew, K.; Sundararaman, R.; Letchworth-Weaver, K.; Arias, T. A.; Hennig, R. G. Implicit solvation model for density-functional study of nanocrystal surfaces and reaction pathways. *J. Chem. Phys.* **2014**, *140*, 084106.

(102) Mathew, K.; Kolluru, V. S. C.; Mula, S.; Steinmann, S. N.; Hennig, R. G. Implicit self-consistent electrolyte model in plane-wave density-functional theory. *J. Chem. Phys.* **2019**, *151*, 234101.

(103) Kresse, G.; Joubert, D. From ultrasoft pseudopotentials to the projector augmented-wave method. *Phys. Rev. B* **1999**, *59*, 1758–1775.

(104) Yu, M.; Trinkle, D. R. Accurate and efficient algorithm for Bader charge integration. *J. Chem. Phys.* **2011**, *134*, 064111.

(105) Sanville, E.; Kenny, S. D.; Smith, R.; Henkelman, G. An improved grid-based algorithm for Bader charge allocation. *J. Comp. Chem.* **2007**, *28*, 899–908.

(106) Tang, W.; Sanville, E.; Henkelman, G. A grid-based Bader analysis algorithm without lattice bias. *J. Phys.: Condens. Matter* **2009**, *21*, 084204.

(107) Henkelman, G.; Arnaldsson, A.; Jónsson, H. A fast and robust algorithm for Bader decomposition of charge density. *Comput. Mater. Sci.* **2006**, *36*, 354–360.

(108) Allen, M. P.; Tildesley, D. J., *Computer Simulation of Liquids*; Press, O. C., Ed., 1987.

(109) Moskaleva, L. V.; Weiss, T.; Klüner, T.; Bäumer, M. Chemisorbed Oxygen on the Au(321) Surface Alloyed with Silver: A First-Principles Investigation. *J. Phys. Chem. C* **2015**, *119*, 9215–9226.

(110) Carbogno, C.; Gross, A.; Meyer, J.; Reuter, K. In *Dynamics of Gas-Surface Interactions: Atomic-level Understanding of Scattering Processes at Surfaces*, Díez Muiño, R., Busnengo, H. F., Eds.; Springer Berlin Heidelberg: Berlin, Heidelberg, 2013, pp 389–419.

(111) Larsen, A. H. et al. The atomic simulation environment—a Python library for working with atoms. *J. Phys. Condens. Matter* **2017**, *29*, 273002.

(112) Bahn, S. R.; Jacobsen, K. W. An object-oriented scripting interface to a legacy electronic structure code. *Comput. Sci. Eng.* **2002**, *4*, 56–66.

(113) Haynes, W. M., *CRC handbook of chemistry and physics*; CRC press: 2016.

(114) *Lange's Handbook of Chemistry*, 15th ed.; Dean, J. A., Ed.; McGraw-Hill, New York: 1999.

(115) ASE developers, Vibrational Modes. Accessed: 2024-10-17, `https://wiki.fysik.dtu.dk/ase/ase/vibrations/modes.html`.

(116) LibreTexts Molecular Orbital Theory Predicts that Molecular Oxygen is Paramagnetic. Accessed: 2024-05-22, `https://chem.libretexts.org/Courses/Pacific_Union_College/Quantum_Chemistry/09%3A_Chemical_`

Bonding_in_Diatomic_Molecules/9.10%3A_Molecular_Orbital_Theory_Predicts_that_Molecular_Oxygen_is_Paramagnetic.

(117) Ervin, K. M.; Anusiewicz, I.; Skurski, P.; Simons, J.; Lineberger, W. C. The Only Stable State of O_2^- Is the X $^2\Pi_g$ Ground State and It (Still!) Has an Adiabatic Electron Detachment Energy of 0.45 eV. *J. Phys. Chem. A* **2003**, *107*, 8521–8529.

(118) Redington, R. L.; Olson, W. B.; Cross, P. C. Studies of Hydrogen Peroxide: The Infrared Spectrum and the Internal Rotation Problem. *J. Chem. Phys.* **1962**, *36*, 1311.

(119) Herzberg, G.; Mrozowski, S. Molecular Spectra and Molecular Structure. I. Spectra of Diatomic Molecules. *Am. J. Phys.* **1951**, *19*, 390–391.

(120) He, X.; Zhu, Y.; Epstein, A.; Mo, Y. Statistical variances of diffusional properties from ab initio molecular dynamics simulations. *Npj Comput. Mater.* **2018**, *4*, 1–9.

(121) Gauthier, J. A.; Ringe, S.; Dickens, C. F.; Garza, A. J.; Bell, A. T.; Head-Gordon, M.; Nørskov, J. K.; Chan, K. Challenges in Modeling Electrochemical Reaction Energetics with Polarizable Continuum Models. *ACS Catal.* **2019**, *9*, 920–931.

(122) Sakong, S.; Forster-Tonigold, K.; Groß, A. The structure of water at a Pt(111) electrode and the potential of zero charge studied from first principles. *J. Chem. Phys.* **2016**, *144*, 194701.

(123) Groß, A.; Sakong, S. Ab Initio Simulations of Water/Metal Interfaces. *Chem. Rev.* **2022**, *122*, 10746–10776.

(124) Marković, N.; Adžić, R.; Vešović, V. Structural effects in electrocatalysis: Oxygen reduction on the gold single crystal electrodes with (110) and (111) orientations. *J. Electroanal. Chem.* **1984**, *165*, 121–133.

(125) Adžić, R.; Štrbac, S.; Anastasijević, N. Electrocatalysis of oxygen on single crystal gold electrodes. *Mater. Chem. Phys.* **1989**, *22*, 349–375.

(126) Štrbac, S.; Anastasijević, N.; Adžić, R. Oxygen reduction on Au(111) and vicinal Au(332) faces: A rotating disc and disc-ring study. *Electrochim. Acta* **1994**, *39*, 983–990.

(127) Štrbac, S.; Adžić, R. The influence of pH on reaction pathways for O_2 reduction on the Au(100) face. *Electrochim. Acta* **1996**, *41*, 2903–2908.

(128) Blizanac, B. B.; Lucas, C. A.; Gallagher, M. E.; Arenz, M.; Ross, P. N.; Marković, N. M. Anion Adsorption, CO Oxidation, and Oxygen Reduction Reaction on a Au(100) Surface: The pH Effect. *J. Phys. Chem. B* **2004**, *108*, 625–634.

(129) Rodriguez, P.; Koper, M. T. M. Electrocatalysis on gold. *Phys. Chem. Chem. Phys.* **2014**, *16*, 13583–13594.

(130) Hansen, H. A.; Viswanathan, V.; Nørskov, J. K. Unifying Kinetic and Thermodynamic Analysis of 2 e– and 4 e– Reduction of Oxygen on Metal Surfaces. *J. Phys. Chem. C* **2014**, *118*, 6706–6718.

(131) Schmidt, T.; Stamenkovic, V.; Arenz, M.; Marković, N.; Ross, P. Oxygen electrocatalysis in alkaline electrolyte: Pt(hkl), Au(hkl) and the effect of Pd-modification. *Electrochim. Acta* **2002**, *47*, 3765–3776.

(132) Ignaczak, A.; Nazmutdinov, R.; Goduljan, A.; Pinto, L.; Juarez, F.; Quaino, P.; Belletti, G.; Santos, E.; Schmickler, W. Oxygen Reduction in Alkaline Media—a Discussion. *Electrocatalysis* **2017**, *8*, 554–564.

(133) Lu, F.; Zhang, Y.; Liu, S.; Lu, D.; Su, D.; Liu, M.; Zhang, Y.; Liu, P.; Wang, J. X.; Adžić, R. R.; Gang, O. Surface Proton Transfer Promotes Four-Electron Oxygen Reduction on Gold Nanocrystal Surfaces in Alkaline Solution. *J. Am. Chem. Soc.* **2017**, *139*, PMID: 28493691, 7310–7317.

(134) Vassilev, P.; Koper, M. T. M. Electrochemical Reduction of Oxygen on Gold Surfaces: A Density Functional Theory Study of Intermediates and Reaction Paths. *J. Phys. Chem. C* **2007**, *111*, 2607–2613.

(135) Duan, Z.; Henkelman, G. Theoretical Resolution of the Exceptional Oxygen Reduction Activity of Au(100) in Alkaline Media. *ACS Catal.* **2019**, *9*, 5567–5573.

(136) Hörmann, N. G.; Andreussi, O.; Marzari, N. Grand canonical simulations of electrochemical interfaces in implicit solvation models. *J. Chem. Phys.* **2019**, *150*, 041730.

(137) Ringe, S.; Hörmann, N. G.; Oberhofer, H.; Reuter, K. Implicit Solvation Methods for Catalysis at Electrified Interfaces. *Chem. Rev.* **2022**, *122*, 10777–10820.

(138) Panchenko, A.; Koper, M. T. M.; Shubina, T. E.; Mitchell, S. J.; Roduner, E. Ab Initio Calculations of Intermediates of Oxygen Reduction on Low-Index Platinum Surfaces. *J. Electrochem. Soc.* **2004**, *151*, A2016.

(139) Markovic, N.; Gasteiger, H.; Ross, P. N. Kinetics of Oxygen Reduction on Pt (Hkl) Electrodes: Implications for the Crystallite Size Effect with Supported Pt Electrocatalysts. *J. Electrochem. Soc.* **1997**, *144*, 1591–1597.

(140) Hansen, H. A.; Rossmeisl, J.; Nørskov, J. K. Surface Pourbaix Diagrams and Oxygen Reduction Activity of Pt, Ag and Ni(111) Surfaces Studied by DFT. *Phys. Chem. Chem. Phys.* **2008**, *10*, 25.

(141) Markovic, N. Surface Science Studies of Model Fuel Cell Electrocatalysts. *Surf. Sci. Rep.* **2002**, *45*, 117–229.

(142) Lv, H.; Li, D.; Strmcnik, D.; Paulikas, A. P.; Markovic, N. M.; Stamenkovic, V. R. Recent Advances in the Design of Tailored Nanomaterials for Efficient Oxygen Reduction Reaction. *Nano Energy* **2016**, *29*, 149–165.

(143) Marković, N. M.; Adžić, R. R.; Cahan, B. D.; Yeager, E. B. Structural Effects in Electrocatalysis: Oxygen Reduction on Platinum Low Index Single-Crystal Surfaces in Perchloric Acid Solutions. *J. Electroanal. Chem.* **1994**, *377*, 249–259.

(144) Casalongue, H. S.; Kaya, S.; Viswanathan, V.; Miller, D. J.; Friebel, D.; Hansen, H. A.; Norskov, J. K.; Nilsson, A.; Ogasawara, H. Direct Observation of the Oxygenated Species during Oxygen Reduction Reaction on a Pt Fuel Cell Cathode. *Nat. Commun.* **2013**, *4*, 2817.

(145) Keith, J. A.; Jerkiewicz, G.; Jacob, T. Theoretical Investigations of the Oxygen Reduction Reaction on Pt(111). *Chem. Phys. Chem.* **2010**.

(146) Tripković, V.; Skúlason, E.; Siahrostami, S.; Nørskov, J. K.; Rossmeisl, J. The oxygen reduction reaction mechanism on Pt(111) from density functional theory calculations. *Electrochim. Acta* **2010**, *55*, 7975–7981.

(147) Chan, K.; Nørskov, J. K. Electrochemical Barriers Made Simple. *J. Phys. Chem.* **2015**, *6*, 2663–2668.

(148) Bergmann, N.; Hörmann, N. G.; Reuter, K. Ab Initio-Based Modeling of Thermodynamic Cyclic Voltammograms: A Benchmark Study on Ag(100) in Bromide Solutions. *J. Chem. Theory Comput.* **2023**, *19*, 8815–8825.

(149) Buraschi, M.; Horsfield, A. P.; Cucinotta, C. S. Revealing Interface Polarization Effects on the Electrical Double Layer with Efficient Open Boundary Simulations under Potential Control. *J. Phys. Chem. Lett.* **2024**, *15*, 4872–4879.

(150) Vijay, S.; Hogg, T. V.; Ehlers, J.; Kristoffersen, H. H.; Katayama, Y.; Shao Horn, Y.; Chorkendorff, I.; Chan, K.; Seger, B. Interaction of CO with Gold in an Electrochemical Environment. *J. Phys. Chem. C* **2021**, *125*, 17684–17689.

(151) Clark, E. L.; Nielsen, R.; Sørensen, J. E.; Needham, J. L.; Seger, B.; Chorkendorff, I. Tuning Surface Reactivity and Electric Field Strength via Intermetallic Alloying. *ACS Energy Lett.* **2023**, *8*, 4414–4420.

(152) Li, M. F.; Liao, L. W.; Yuan, D. F.; Mei, D.; Chen, Y.-X. pH effect on oxygen reduction reaction at Pt(111) electrode. *Electrochim. Acta* **2013**, *110*, 780–789.

(153) Van der Niet, M. J.; Garcia-Araez, N.; Hernández, J.; Feliu, J. M.; Koper, M. T. Water dissociation on well-defined platinum surfaces: The electrochemical perspective. *Catal. Today* **2013**, *202*, 105–113.

(154) Kristoffersen, H. H.; Vegge, T.; Hansen, H. A. OH formation and H_2 adsorption at the liquid water–Pt(111) interface. *Chem. Sci.* **2018**, *9*, 6912–6921.

(155) Marković, N. M.; Adić, R. R.; Vešović, V. B. Structural effects in electrocatalysis: Oxygen reduction on the gold single crystal electrodes with (110)

and (111) orientations. *J. Electroanal. Chem. Interf. Electrochem.* **1984**, *165*, 121–133.

(156) Lang, N. D.; Kohn, W. Theory of Metal Surfaces: Induced Surface Charge and Image Potential. *Phys. Rev. B* **1973**, *7*, 2270–2281.

(157) Šljivančanin, Z.; Hammer, B. Oxygen dissociation at close-packed Pt terraces, Pt steps, and Ag-covered Pt steps studied with density functional theory. *Surf. Sci.* **2002**, *515*, 235–244.

(158) Wang, X.-G.; Fisher, G. B. Phase Diagram of Molecular Oxygen Adsorption on the (111) Platinum Surface. *Phys. Rev. Lett.* **2007**, *99*, 066101.

(159) Xue, T.; Wu, C.; Ding, X.; Sun, J. Dissociative adsorption of O_2 on strained Pt(111). *Phys. Chem. Chem. Phys.* **2018**, *20*, 17927–17933.

(160) Eichler, A.; Hafner, J. Molecular Precursors in the Dissociative Adsorption of O_2 on Pt(111). *Phys. Rev. Lett.* **1997**, *79*, 4481–4484.

(161) Qi, L.; Yu, J.; Li, J. Coverage dependence and hydroperoxyl-mediated pathway of catalytic water formation on Pt (111) surface. *J. Chem. Phys.* **2006**, *125*, 054701.

(162) McEwen, J.-S.; Bray, J. M.; Wuc, C.; Schneider, W. F. How low can you go? Minimum energy pathways for O_2 dissociation on Pt(111). *Phys. Chem. Chem. Phys.* **2012**, *14*, 14067–14076.

(163) Li, C.-Y.; Le, J.-B.; Wang, Y.-H.; Chen, S.; Yang, Z.-L.; Li, J.-F.; Cheng, J.; Tian, Z.-Q. In situ probing electrified interfacial water structures at atomically flat surfaces. *Nat. Mater.* **2019**, *18*, 697–701.

(164) Le, J.-B.; Fan, Q.-Y.; Li, J.-Q.; Cheng, J. Molecular origin of negative component of Helmholtz capacitance at electrified Pt(111)/water interface. *Sci. Adv.* **2020**, *6*, eabb1219.

(165) Limmer, D. T.; Willard, A. P.; Madden, P.; Chandler, D. Hydration of metal surfaces can be dynamically heterogeneous and hydrophobic. *Proc. Natl. Acad. Sci. U.S.A.* **2013**, *110*, 4200–4205.

(166) Gland, J. L.; Sexton, B. A.; Fisher, G. B. Oxygen interactions with the Pt(111) surface. *Surf. Sci.* **1980**, *95*, 587–602.

(167) Nolan, P. D.; Lutz, B. R.; Tanaka, P. L.; Davis, J. E.; Mullins, C. B. Molecularly chemisorbed intermediates to oxygen adsorption on Pt(111): A molecular beam and electron energy-loss spectroscopy study. *J. Chem. Phys.* **1999**, *111*, 3696–3704.